# Combustion knock in divided chamber type diesel engines( Dissertation_全文 )

AUTHOR(S):

Ikegami, Makoto

# Combustion Knock in Divided Chamber Type Diesel Engines

By

Makoto IKEGAMI

1967

# Combustion Knock in Divided Chamber Type Diesel Engines

By

Makoto IKEGAMI

1967

CONTENTS

# INTRODUCTION

The present progress of the high speed and compact diesel engines owes much to rational design attained by successful matching of fuel injection system and skillful utilization of high intensity air-turbulence and -swirl induced in the combustion chamber, namely, by the improvements made on the combustion process. Owing to its prominent performance, ever-increasing demand for this type engine has arisen as a promising economic prime mover, say, in the use of passenger transport that had been considered as the application field of spark ignition engine. Simultaneously increasing attention is now paid to the eradication of faults that were relatively less important in the earlier stages of diesel engine's development. One of these is engine noise.

At the present time being, the conceived target for reducing the noise of the small diesel engine is to equalize it down to a degree within that of gasoline engine as its competitor. It may be considered from this point of view that among the predominant noises suction- and exhaust-noises as well as creaking from the engine body and accessories are not of prime importance as the noise problem peculiar to the diesel engine. In the meanwhile, a handicap in combustion noise is the maximum barrier, so that its solution seems to be on the tiptoe of expectation.

The combustion noise and its extreme manifestation as diesel knock are originated from a sharp pressure rise in cylinder due to explosive combustion of mixture formed during the so-called delay period. The absolute necessity for relieving the pressure development from the explosive pressure change is to reduce the fuel quantity present in the delay period. In this viewpoint, possible means of controlling the diesel knock will be classified into the following four basic categories:

(1) Shortening the ignition delay; the use of high ignition quality fuels, increasing the compression ratio, adopting an ignition promotor such as the glow stud, etc.

(2) Reducing the rate of fuel injection during the ignition delay; the use of specially designed injection nozzle such as throttle nozzle and "Pintaux" nozzle[1]*, and the adoption of pilot injection system[2].

(3) Changing the course of mixture formation to reduce fuel that takes a part in the rapid combustion; for example, the "M-combustion system"[3] using the combustion chamber wall as refuge of fuel.

(4) Separate introduction of fuel; for example, "Fumigation" by intro-

* Numbers in parentheses designate References at end of the volume.

ducing a supplementary fuel in the suction duct in a very fine mist[4], and "Vigom process" in which the fuel is injected separatedly through a single injector by using double cam in the fuel pump[5].
In those means, the first is considered to be most classical, the second and third to be modern, and the fourth seems to belong to a future problem. Some of them have attained considerable progress in recent years on the demand of the "multifuel operation"[6][7][8] of the engine; that is, to run satisfactorily with any kinds of fuel from gasoline to diesel fuel having a high cetane number. This problem has a close connection with the subject now concerned with, since one of the factors limiting the multifuel ability is the long ignition delay of the fuel and resulting diesel knock.

When a gasoline engine is knocking or emitting other kinds of combustion noise, deterioration of performance usually supervenes; for this reason, much efforts have been made for their elimination. On the contrary, reduction of diesel combustion noise is not indispensable for the improvement of the thermal effieiency, or in many cases, too quiet running sometimes sacrifices the fuel economy and the maximum output. As an example apt to encounter, a very early ignition of fuel will hinder its access to air remote from the injection nozzle thereby resulting in a poor combustion. Generally speaking, several methods of eliminating the combustion noise are qualified when they are not malignant on other performances of the engine; not merely on the fuel economy and maximum output but also on ability of cold-starting, durability of the engine, cost of construction and so forth.

This thesis is based on a series of experiments and considerations with a view to shedding more light on a smooth running of compact diesel engines, taking into consideration the matters mentioned above. They were made less on the special combustion systems such as the third or fourth category of those presented earlier, but mainly on conventional systems, of divided chamber type engines which were most widely applicated in the field of small size engines, from several new viewpoints. In the first chapter, origin of the combustion noise was pursued from the mechanical and acoustic points of view. Thereby all the problem of the combustion noise could be reduced to the matter of pressure-time relation in the combustion chamber. In the connection with the research of the present subject, in the second chapter, in-

vestigation was carried out to offer the requisite for an accurate measurement of pressure in the combustion chamber. In the third through fifth chapters, several works were made on influences of various circumstances on the combustion progress, especially on the rate of pressure rise in the combustion chamber of the divided chamber type engines; third chapter dealt with the effect of dimension of connecting passage on the pressure change in cylinder, the fourth with various influences on combustion and pressure rate in swirl chamber type engines, and the fifth with the idling knock phenomenon and its elimination of prechamber type engines. In the last chapter, the origin of rapid combustion was analyzed from a new viewpoint by introducing a model in which the ignition delay of every fuel element varied from time to time according to the development of pressure and temperature in the combustion chamber.

# CHAPTER 1

## Sources of Combustion Noise and Criterion of Its Intensity

### 1.1. Outline of the Problems

Numerous studies have been made to clarify how the sharp pressure rise in the combustion chamber can be transmitted to the ear of a listener acknowledging it as the combustion noise. There are two concepts about the mechanism of the noise generation: The one is that the transient vibration in the engine structure linked with the chamber walls causes the outer surface to emit the noise, as has been supported by Davies[2]. The other is that the gas oscillation initiated by a sudden combustion emits a noise of the identical frequency directly through the engine walls in the same manner as that occurring in a gasoline engine. In this chapter, the former concept was emphasized by several evidences obtained in the course of the experiment.

In the second part of this chapter an examination of the excitation of vibration by given force-time relations was made in order to obtain some knowledges of how the rate of pressure rise relates intensity of emitted noise. For this purpose, two methods may be available: The one is the harmonic analysis of cylinder pressure, namely, transforming the cylinder pressure versus time relation into power spectrum, with which the emitted noise may be correlated, as has been conducted by Priede[9]. The other is the analysis of free oscillation generated in the engine structure by the rise in the cylinder pressure. In the present investigation, the latter method was introduced by adopting a simplified model proposed by Davies[2], in which the vibrating member is idealized by a mass permitted to move in the direction of varying force under restraint of a spring.

The last problem of this chapter is how the intensity of the combustion noise will be described and what will be a criterion of discriminating whether the diesel knock occurs. For this purpose the maximum rate of pressure rise caused by combustion was proposed as the measure.

### 1.2 Frequency Analysis of Combustion Noise

#### 1) Experimental engine and measuring apparatus

A water-cooled four-cycle single cylinder diesel engine manufactured by Yanmar Diesel Co. (ST-95 type) was used in the experiment. It could be oper-

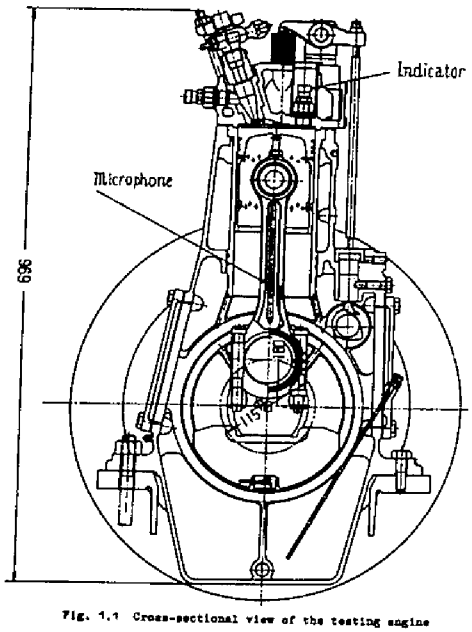


Fig. 1.1 Cross-sectional view of the testing engine

ated as either a pre-chamber type engine or as a swirl chamber type. The principal dimensions of the engine were as follows:

| | | |
|---|---|---|
| Cylinder bore and stroke | 95 mm and 115 mm respectively | |
| Nominal output | 7 PS at 1400 rpm | |
| Combustion chamber | Pre-chamber type | Swirl chamber type |
| Ratio of the auxiliary chamber to the total compression volume | 0.31 | 0.63 |
| Ratio of cross-sectional area of the connecting passage to piston area | 0.52 % | 2.0 % |
| compression ratio | 19 : 1 | 16 : 1 |

Fig. 1.1 shows the cross-sectional view of the engine. Fuel injection pump was Bosch type PE1A70B101, whose plunger diameter was 7 mm. The opening pressure of the injection nozzle was adjusted so as to be 105 $kg/cm^2$ in the course of the experiment. The fuel used was heavy oil "A" (specific weight 0.845, cetane number 45).

Noise measurement was made by using an audio-frequency analyzer (Reutlinger Frequenzspektrometer). As the transducer of the cylinder pressure, strain gage type indicators (made of Kyowa Dengyo Co., PHF-7B type), which had the nominal natural frequency above 35 kc/sec, were flushed to the chamber wall as shown in Fig. 1.1. The recording of the pressure diagrams was made on an electromagnetic oscillograph with B type vibrator having a constant sensibility up to 3.5 kc/sec, after anamplification by a transistor circuit. In addition to this, crank-angle marks and timing marks were recorded on each oscillogram.

2) Frequency analysis of body noise

With the installation mentioned above, noises from engine body were analyzed under the conditions with and without knocking, in contrast with the non-firing conditions; typical modes of knocking were examined with (i) the idling knock which was remarkable in low speed range of a pre-chamber type chamber (idling at 630 rpm), and (ii) conventional knock in high speed range of a swirl chamber type chamber (at 1500 rpm). In order to avoid the overestimation of impedimental noises such as those from flywheel and suction-

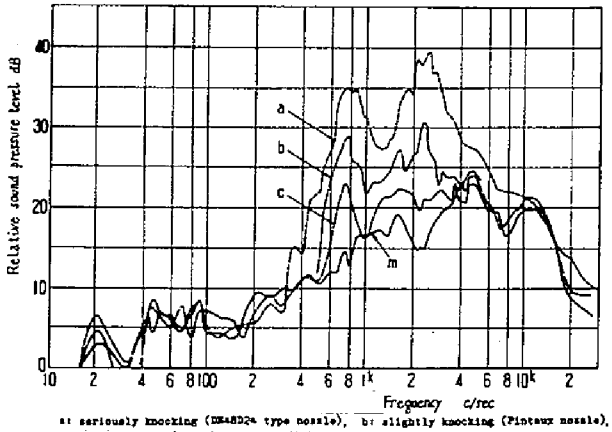


a: seriously knocking (DKA5D2a type nozzle), b: slightly knocking (Pintaux nozzle), c: knocking-free (ibid.), m: non-firing.
Speed 630 rpm and coolant temperature 40°C

Fig. 1.2 Noise spectra at a low speed idling in the pre-chamber installation

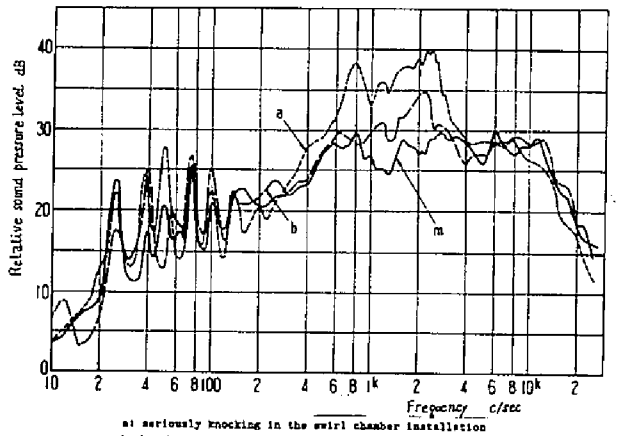


a: seriously knocking in the swirl chamber installation
b: knocking-free in the pre-chamber installation
m: non-firing
Speed at 1 500 rpm, Bmep 4.0 kg/cm² and coolant temperature 80°C

Fig. 1.3 Noise spectra at a high speed

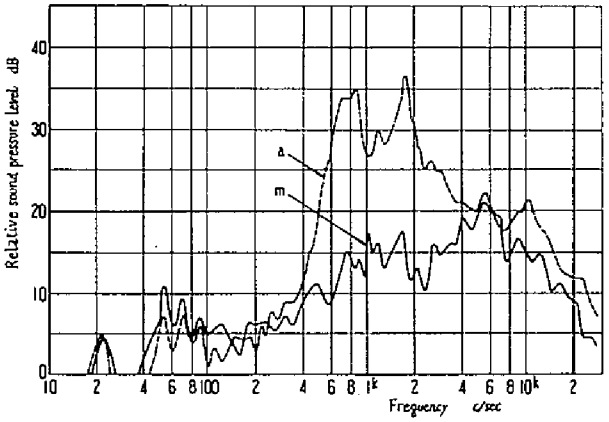


a: seriously knocking, m: non-firing
Conditions are the same as those in Fig. 1.2.

Fig. 1.4 Noise spectra with a cast iron piston

and exhaust-noises, the receiving microphone was placed at a distance of 110 mm from the engine cover opposite the flywheel, as illustrated in Fig. 1.1.

With the pre-chamber type, the testing engine emitted a furious knocking at speed lower than 800 rpm. This is the so-called idling knock, whose intensity and existence are influenced by the cylinder wall temperature, the rate of fuel injection, its injection timing and so on. Fig. 1.2 shows the results of frequency analysis of the body noise, under the conditions without load at a low speed, for various types of injection nozzles that would have different injection characteristics. It can be seen from the figure that a relatively high frequency range between 400 c/sec and 4000 c/sec has a connection with the combustion noise. The frequencies giving two peaks are not influenced by the intensity of knock nor whether an audible knocking occurs or not.

Fig. 1.3 contrasts the case of furiously knocking in the swirl chamber type with the case of rather smooth running in the pre-chamber type, both at the full speed of the engine. It can be seen that the frequencies giving peak levels in the swirl chamber type virtually coincide with those of idling knock and with noise at high speed with the pre-chamber type. Therefore we may conclude that the constituent frequencies of the combustion noise are irrespective of the type of the combustion chamber or running conditions such as speed and load or injection rate, and that there is no essential difference between the idling knock and the ordinary knock occurring at a high speed, although the running speed relates to the spectra of non-firing and of lower frequency region.

These facts suggest that the combustion noise is caused by the transient excitation by the cylinder pressure in some particular mechanical components of the engine structure. Another evidence supporting this matter is that a considerable change of the frequencies was experienced by alternating the aluminium piston to a heavier cast iron piston, as shown in Fig. 1.4; the higher frequency shifts from 2.5 kc/sec to 1.8 kc/sec and the lower frequency from 0.80 kc/sec to 0.85 kc/sec. This fact indicates that the combustion noise has a very close connection with the crank and piston mechanism.

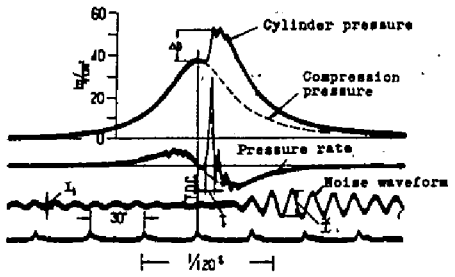


Fig. 1.5 Example of indicator diagram

## 1.3 The Relation between Pressure Development in Cylinder and Combustion Noise

### 1) Theoretical consideration

Nomenclature

$p_z$ cylinder pressure
$\Delta p$ pressure rise due to combustion
$t$ time variable
$t_o$ period of vibration
$t_e$ duration of effective pressure rise, i.e., the duration of cylinder-pressure changing from 10 % to 90 % of $\Delta p$
$x$ displacement of a vibrating member
$\tilde{x}$ amplitude of vibration excited
$x_s$ amplitude for step-functional pressure change
$\phi$ non dimensional amplitude of vibration ($= \tilde{x}/x_s$)
$\xi$ ratio of rising time of pressure to period of vibration ($=t_e/t_o$)

In Fig. 1.5 is shown an example of indicator diagram in which some of symbols are illustrated.

The relationship between the amplitude of mechanical vibration and the pressure development inside the cylinder will be estimated if we consider a simplified model of the vibration system such as follows:

(1) The model is a one-degree-of-freedom system of vibration.

(2) The mechanical impedance at the driving terminal, i.e., the surface of the piston, is so high that pressure development is not influenced by the transient vibration excited in the system.

(3) Only a single blow acts on the system, or, in other words, the excitation of vibration is not influenced by that occuring in previous cycle.

(4) The slopes of pressure change during compression and expansion strokes are low enough to be neglected, compared with the rate of pressure rise during combustion.

(5) There is no decay in the vibration once excited.

At first, we define $x^*(t)$ as the unit step response, i.e. the transient waveform of vibration when the cylinder pressure instantaneously jumps by a unit magnitude. According to the above presented assumptions, $x^*$ is described as follows:

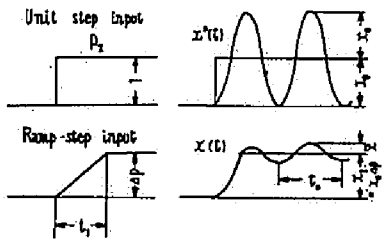


Fig. 1.6 Calculation of transient vibration from given $p_g(t)$

$$x^*(t) = x_0(1-\cos\omega_0 t) \qquad (t \geq 0) \tag{1.1}$$

where $x_0$ is a constant and $\omega_0$ the angular frequency. By using $x^*(t)$ thus defined, we can calculate the response $x(t)$ for a given pressure-time relation $p_z(t)$, by means of, for example, the Duhammel's formula.

Fig. 1.6 illustrates the relation between $x(t)$ and $p_z(t)$ for the unit step functional input where the amplitude of vibration is $x_0$. Now we consider that an input of a ramp-step function of total rising time $t_1$ and the pressure rise by $\Delta p$ produces a vibration of amplitude $\tilde{x}$ on the static displacement $x_s$. It can be easily noticed that $x_s$ is the product of $x_0$ and $\Delta p$, because of linearity of the system, and signifies the amplitude of step-functional pressure change because x coincides with $x_s$ at the extreme of $t_1=0$. We can evaluate the effect of the course of pressure on noise by using the ratio $\phi = \tilde{x}/x_s$, namely, the ratio of amplitude for a given development of pressure to the amplitude for the pure step-functional course of the same pressure rise. The results obtained is as follows:

$$\phi = \frac{\tilde{x}}{x_s} = \frac{|\sin(\omega_0 t_1/2)|}{\omega_0 t_1/2} \tag{1.2}$$

where $\omega_0$ is re-written by the period of vibration $t_0 = 2\pi/\omega_0$. The notation of $t_1$ may be replaced by $t_e$ which is the effective duration of pressure rise, defined as the duration of pressure changing from 10 % to 90 % of $\Delta p$. This substitution is required from the comparison between waveforms of cylinder pressure. For the ramp-step function, $t_e$ holds a relation as follows:

$$K_1 = t_1/t_e = 5/4 \tag{1.3}$$

Thirdly, the ratio of $t_e$ to $t_0$ is introducted, namely

$$\xi = t_e/t_0 \tag{1.4}$$

This is the non-dimensional variable that represents the sharpness of pressure change relative to the period of vibration $t_0$. With those notations, Eq. (1.2) is converted into

$$\phi = \frac{|\sin k_1\pi\xi|}{k_1\pi\xi} \qquad \text{(for the ramp-step function)} \tag{1.5}$$

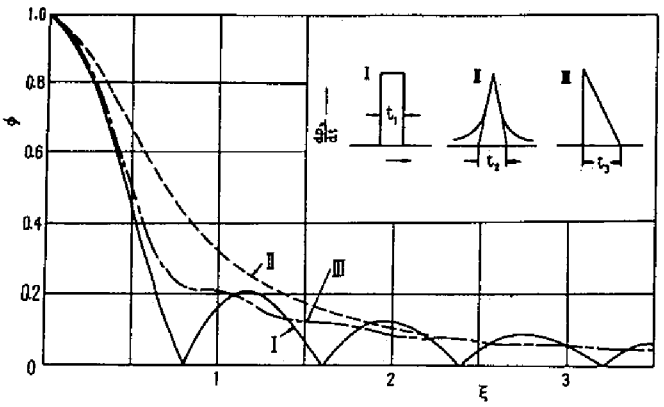


Fig. 1.7 $\phi$ versus $\xi$ for various functions of input

We can find out similar relationships for any analytical functions of input. Some results of typical functions expected in the actual engine are shown in Table 1.1. The corresponding curves are inclusively drawn in Fig. 1.7. These lead the following informations as regards the effect of pressure development on the amplitude of vibration:

(1) For a waveform of input, the amplitude of vibration generally decreases with $\xi$, although it is not always monotonous, as is observed with the ramp-step input (Curve I). Even for this case, the following formula holds:

$$\phi \leqq \frac{1}{\kappa_1 \pi \xi} \tag{1.6}$$

(2) As for the calculated cases, $\phi$ decreases rapidly with $\xi$ when $\xi$ is between 0.5 and the unity. Hence the intensity of the combustion noise will rapidly change if $\xi$ is in this range.

(3) Since the amplitude of vibration $\tilde{x}$ is proportional to the product of $\phi$ and $\Delta p$, $\tilde{x}$ depends only on $\Delta p$ for a very small value of $\xi$. For a larger $\xi$, $\phi$ is approximately proportional to $1/\xi$ for Curves I and III, and to $1/\xi^2$ for Curve II, as seen from the table. For a kind of pressure-time curve, the relation between the maximum rate of pressure rise $(dp/dt)_{max}$ and $\xi$ is clearly given by the following form.

$$\left(\frac{dp}{dt}\right)_{max} = const \times \frac{\Delta p}{\xi}$$

Therefore the amplitude $\tilde{x}$ will be

$$\tilde{x} \propto \phi \Delta p \propto \frac{\Delta p}{\xi} \propto \left(\frac{dp}{dt}\right)_{max} \quad \text{for Curves I and III} \tag{1.7}$$

$$\propto \frac{\Delta p}{\xi^2} \propto \frac{1}{\Delta p}\left(\frac{dp}{dt}\right)^2_{max} \quad \text{for Curve II} \tag{1.8}$$

It is clear from these relations that in either case the amplitude $\tilde{x}$ is largely dependent on $(dp/dt)_{max}$ but less or independent on the pressure rise $\Delta p$ for a larger value of $\xi$.

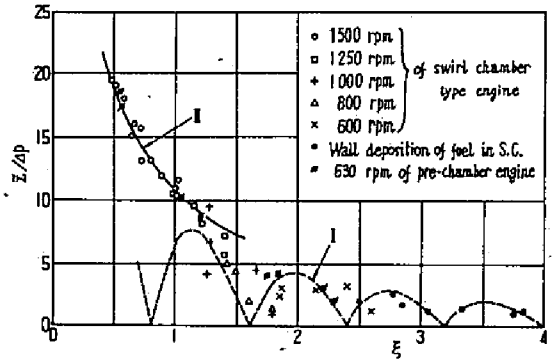


Fig. 1.8 Correlation between Σ/Δp and ξ

Table 1.1 Theoretical relationships between $\phi$ and $\xi$

| | Ramp-step fuction | Exponential function | Parabolic function |
|---|---|---|---|
| $p_z$ |  |  |  |
| $dp_z/dt$ |  |  |  |
| | $\begin{cases} 0 & t \le 0 \\ \Delta p/t_1 & 0 < t \le t_1 \\ 0 & t_1 < t \end{cases}$ | $\frac{\Delta p}{t_2} \exp\left[-\frac{2t}{t_1}\right]$ | $\begin{cases} 0 & t \le 0 \\ \frac{\Delta p}{t_3}\left(1-\frac{t}{t_3}\right) & 0 < t \le t_3 \\ 0 & t_3 < t \end{cases}$ |
| $k_j = t_j/t_e$ | $k_1 = 5/4$ | $k_2 = \log_{10} e$ | $k_3 = \sqrt{5/2}$ |
| $\phi$ | $\frac{\lvert \sin(k_1 \pi \xi) \rvert}{(k_1 \pi \xi)}$ | $\frac{1}{(k_2 \pi \xi)^2 + 1}$ | $\frac{1}{k_3 \pi \xi} \sqrt{1 - \frac{\sin 2k_3 \pi \xi}{k_3 \pi \xi} + \frac{\sin^2 k_1 \pi \xi}{k_1 \pi \xi}}$ |
| | Curve I Fig 1.7 | Curve II | Curve III |

2) Experimental results and evaluation on combustion characteristics

Unfortunately, it was difficult to confirm the above mentioned theory at the practical system of the engine, since the amplitude for the step-wise pressure rise $x_s$ was not known. However, on assuming the linearity of the system, it would be feasible to find out the correlation between $\xi$ and $\tilde{x}/\Delta p$. In order to examine this, a number of indicator diagrams were taken under various test conditions, and both $\Delta p$ and $\xi$ were measured. At the same time, using the frequency analyser tuned to the predominant frequency of the combustion noise, that is 800 c/s, the noise waveform was recorded on the oscillogram together with the pressure patterns. The peak-to-peak amplitude of the selected noise component were assumed to indicate $\tilde{x}$. Fig. 1.8 shows the plots of $\tilde{x}/\Delta p$ against $\xi$, together with the theoretical curves whose vertical scale was so selected as to obtain the best coincidence of the curves with the plots. It turns out from this diagram that the $\tilde{x}/\Delta p$ versus $\xi$ relation resembles in tendency those predicted from the theoretical calculation.

Further, by accounting the running conditions into consideration, the following facts were drawn out.

(1) When the pre-chamber type engine runs with idling knock occurring, $\xi$ is in a range between 0.5 and 1.0. When the knocking is absent with the same speed, $\xi$ is higher than 1.5.

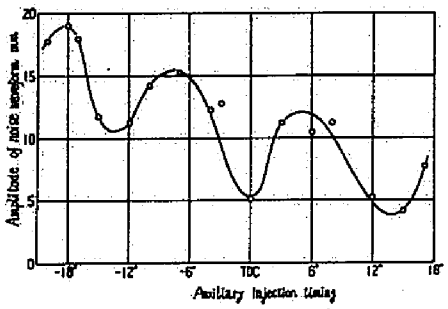


Main injection: 16.2 mg/stroke, 10° before TDC
Auxiliary injection: 15.4 mg/stroke

Fig. 1.9 Combustion noise at dual injection system

(2) With the swirl chamber type engine, $\xi$ distributes over a fairly wide range but is clearly subdivided by the engine speed. This will probably be due to an effect of the swirl intensity on the velocity of combustion. (3) Generally speaking, the engine runs smoothly if $\xi$ is larger than 1.5. Such conditions were materialized with following cases; at high speed with a load and low speed knock-free running with the pre-chamber type engine, at low speed with the swirl chamber type engine, and in the entire range when the fuel is injected onto the wall of the swirl chamber. (4) With a divided chamber type engine fuel injection were made individually from the two sets of injection nozzles in the main and auxiliary chambers (Dual injection system)[10]. Fig. 1.9 shows the noise characteristics measured at varying injection timing of auxiliary chamber at a fixed timing of main injection. The curve shows a periodic rolling. This phenomenon is believed to be caused by twofold pressure rises occurring in the main chamber. The interval between those pressure rises clearly determines whether the excitation of the noise is emphasized or reduced. This supports also the matter that the combustion noise originates from the mechanical vibration as mentioned earlier.

## 1.4 Criterion of Occurrence of Knocking and Its Intensity

There is, in fact, no measure nor criterion reasonably describing the properties of the combustion noise, such as the knock intensity or whether knock occurs, except an empirical expression of maximum rate of pressure rise in terms of crank angle $(dp/d\theta)_{max}$ in which $\theta$ denotes crank angle in degree. It is commonly said that for a small size diesel engine the knock occurs at a value higher than 4 $kg/cm^2/deg$ and that a furious one does at higher than 5 or 6 $kg/cm^2/deg$. Although the amplitude of the transient vibration is determined by the time rate of pressure rise $(dp/dt)$ as has been investigated in the previous section, the knock phenomenon in the actual engine seems to depend not on $(dp/dt)$ but rather on $(dp/d\theta)$. This is not explainable only by the investigation on the mechanical system of vibration. In fact, knock is weak in spite of a large $(dp/dt)$ at a higher speed, while even a small $(dp/dt)$ causes a knock at a lower speed.

This fact is likely to be understood by accounting the "masking effect"[11], which is a well-known phenomenon in the auditory perception

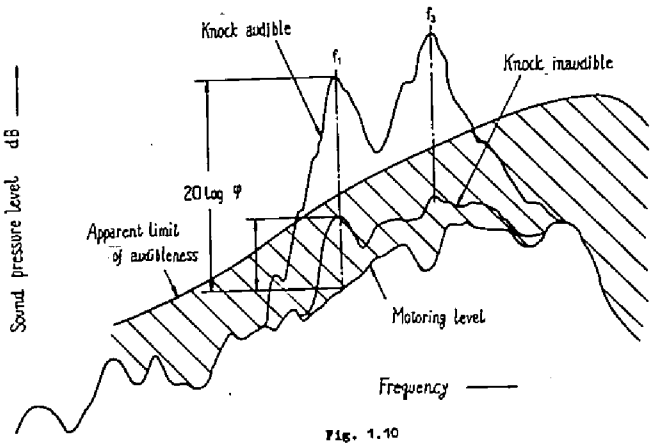


Fig. 1.10

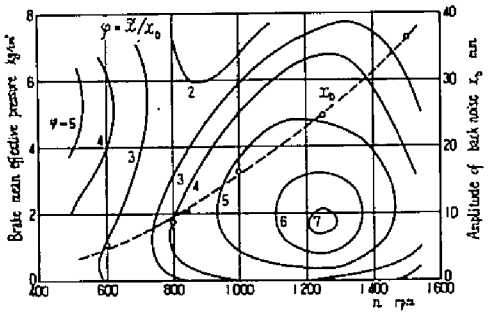


Injection timing at 10° before TDC, coolant at 80°C

Fig. 1.11 Map of φ-value in a swirl chamber type engine

of a man. Generally speaking, when he wants to hear a sound in a background noise, he cannot percieve the objective sound if it is not louder than the background by a certain degree, in other words, the background noise raises the apparent limit of audibleness. It has been known from the physiological acoustics that, in order to discern a harmonic tune out of the field of white noise, it is necessary for the objective sound level to be raised higher than the spectral noise level of the frequency of the tune by a known level which is dependent only on the frequency, for example, by 16 dB for 0.8 kc/s. Fig. 1.10 illustrates the application of the theory on the present problem. If any spectrum does not protrude the hatched region under a firing condition, then the combustion noise is scarcely heard, giving an impression of smooth running. Once some components exceed the apparent limit of audibleness, that is, the upper limit of the hatched region, a listener would experience the knock occurring with the engine. On account of this, the magnitude of 20 $\log \varphi$ indicated in Fig. 1.10, which is difference between the peak noise level of a component and the corresponding motoring level, is considered to be a criterion of whether the knock occurs or not. At the same time, this value will clearly be a measure of knock intensity. Fig. 1.11 illustrates the magnitude of $\varphi$ measured for a wide range of the engine speed n and the brake mean effective pressure with a swirl chamber type engine, showing a tendency somewhat close to what meets the ear.

If $\varphi$ is approximated to be the ratio of the amplitude of combustion noise $\bar{x}$ to that of the corresponding component of background noise $x_b$, then the following discussion may be possible: As is illustrated in Fig. 1.11, $x_b$ is largely dependent on the engine speed n rpm and may be expressed in the following form:

$$x_b = 16\,(n/1000)^2 \tag{1.9}$$

where $x_b$ is measured in mm from an oscillogram. If $\varphi$ is proportional to the square of the maximum rate of pressure rise $(dp/dt)_{max}$ and to the reciprocal of pressure rise $\Delta p$, as suggested by Eq. (1.8), then $\varphi$ will be

$$\varphi = \frac{\bar{x}}{x_b} \propto \frac{1}{n^2 \Delta p}\left(\frac{dp}{dt}\right)^2_{max} \tag{1.10}$$

By using the relationship $dp/dt = 6n\,(dp/d\theta)$, we obtain

$$\varphi \propto \frac{1}{\Delta p}\left(\frac{dp}{d\theta}\right)^2_{max}$$

Namely, $\varphi$ is proportional to $(dp/d\theta)^2_{max}$ for a constant magnitude of pressure rise. In an actually encountered case, the relation between the amplitude of combustion noise $\tilde{x}$ and $(dp/dt)_{max}$ would lie between Eq. (1.7) and Eq. (1.8), probably more close to the latter expression for a range of $\xi$ near its unity, so that $\varphi$ depends very closely on $(dp/d\theta)_{max}$, although many other factors may affect it. For this reason, we can conclude that the maximum rate of pressure rise in terms of crank angle is a good measure describing the knock intensity and at the same time a reasonable criterion of whether an engine is knocking or not.

All discussions in the foregoing section were made for the fundamental component of 0.8 kc/sec of the testing engine and none for higher frequency components that will probably play an important role in characterizing the timbre of the combustion noise. Since the combustion noise originates from the mechanical system of vibration, the origin of characteristic timbre of the combustion noise will be interpreted like this: As the rate of pressure rise $(dp/d\theta)$ increases, the acoustic limits of audibleness are exceeded firstly by the fundamental component, next by the second component of the noise and so on.

## 1.5 Conclusion

As the results of fundamental studies on the origin of combustion noise, the following conclusions were gained:

(1) The constituent frequencies of the combustion noise of a diesel engine are irrespective of the type of combustion chamber or conditions of operation. The immediate cause of the combustion noise is the transient vibration excited by the rapid change in cylinder pressure, in the mechanical system consisting of the piston, the connecting rod, the crank arm and the crankcase.

(2) By assuming that the vibration system was that of one degree of freedom, the relation between pressure development in cylinder and the noise amplitude was determined. The engine is very smooth if the ratio of duration of pressure rise to the period of vibration is larger than 1.5.

(3) The maximum rate of pressure rise measured in terms of crank angle can be adopted as a measure describing the intensity of the combustion noise and the cirterion of whether knock occurs or not. This physical and acoustic meaning is understood by accounting the masking effect into consideration.

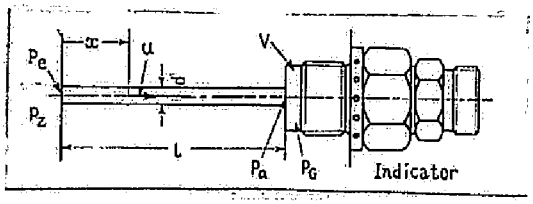


Fig. 2.1

## CHAPTER 2

## On Errors of Indicator due to Pressure Adapter: A Contribution to an Accurate Measurement of Pressure

### 2.1 Purpose of the study

With a view to obtaining distortion-free pressure diagrams, pressure sensitive elements are to be placed flush with the combustion chamber wall. In many cases, however, it is compelled to use an indicator adapter. An inappropriate one will injure the fidelity of pressure response, thus leading to errors in the pressure diagrams. Hence a careless choice of the adapter may occasionally cause unexpected errors in the test results.

The behavior of the gas system inside the leading passage has been successfully treated by acoustics or electro-acoustic analogy[12]. Most important problems met with the use of it are probably understanding the errors in the pressure diagrams and knowing to what extent the passage is available in the measurement. Some solutions for practical use are recently reported; such as for detecting the knock phenomenon in gasoline engines [13][14] and for measurement of changing pressure at low pressure[15].

In this investigation, the behavior of the leading passage is firstly analyzed from the frequency response as well as from the transient response. Further, the errors due to the pressure oscillation which is caused by rapid pressure change in cylinder are estimated by applying the theory of vibration. Further, the available range of a leading passage is studied from several indicator diagrams. An experimental and a theoretical investigation are also conducted in order to ascertain the merit of vibration absorbers and to know their optimum conditions.

### 2.2 Theoretical Considerations on the Behavior of the Adapter

#### 1) Fundamental equations

Fig. 2.1 represents a typical arrangement of an adapter and pick-up system. A canal with constant cross-sectional area f and length $\ell$ is open to the combustion chamber at one end, and a space of volume V. in which a diaphragm of the pressure pick-up is installed, is connected with the passage at its another end. Once the cylinder pressure $p_z$ has rapidly changed,

for instance, through combustion, some transient pressure vibration is caused in the clearance space, thus leading to errors in the pressure diagrams.

The equations describing the behavior of the gas system inside the canal are derived by calculating conservations of mass and of momentum on the assumptions that the gas behaves as an ideal gas following the adiabatic law and that such acoustic variables as pressure and gas velocity may be considered as deviations from mean values. Denoting pressure, velocity and density as p, u and $\rho$ respectively, at a given location x in the canal, we assume that the density change along the canal $\partial\rho/\partial x$ and the change of the square of velocity $\partial u^2/\partial x$ are naught in the equations of continuity and momentum. If reference density $\rho_0$ and sound velocity $a_0=\sqrt{(\partial p/\partial\rho)_s}$ are used, these equations become

$$\frac{\partial p}{\partial t}+\rho_0 a_0^2\frac{\partial u}{\partial x}=0 \tag{2.1}$$

$$\frac{\partial u}{\partial t}+\frac{1}{\rho_0}\frac{\partial p}{\partial x}+W=0 \tag{2.2}$$

where W represents the frictional force per unit of mass. Under a steady state, pressure drop per unit length of the canal $\rho_0 W$ may be described by the following formula for a steady flow in a circular pipe.

$$\rho_0 W=\frac{dp}{dx}=\frac{\lambda}{2d}\rho_0 u^2\frac{u}{|u|} \tag{2.3}$$

where d is the diameter of the canal and $\lambda$ the friction coefficient whose mean value is $2\times10^{-2}$ in a wider range of Reynolds number.

Boundary conditions for inlet and outlet of the canal are given by Bernoulli's equation. As for the open side, when the gas flows into the canal from the cylinder, the pressure at the inlet $p_e$ decreases below that in the cylinder $p_z$, while there is no difference when the gas flows into cylinder from the canal. So we may describe the boundary condition at this end as follows:

$$p_z-p_e=\begin{cases}\dfrac{\rho_0 u_e^2}{2\mu^2} & [u_e\geq 0]\\ 0 & [u_e<0]\end{cases} \tag{2.4}$$

where $u_e$ is the velocity of gas at the inlet and $\mu$ the flow coefficient. The magnitude of the latter fluctuates between 0.6 and 0.8 if there is no fillet nor throttling. As for the clearance-space side, in the same manner

the relation between the pressure at the point $p_a$ and the velocity $u_a$ is given,

$$p_G - p_a = \begin{cases} 0 & [u_a \geqq 0] \\ \dfrac{\rho_0 u_a^2}{2\mu^2} & [u_a < 0] \end{cases} \tag{2.5}$$

The relationship between the excess pressure in the clearance space $p_G$ and the velocity of gas $u_a$ is determined by assuming that the adiabatic gas law holds in the space. The following formula represents its first approximation:

$$\dot{p}_G = \rho_0 a_0^2 f/V \cdot u_a \tag{2.6}$$

In order to recognize the behavior of the adapter, we approximate the system to a lumped parameter one. In deriving the relation between $\dot{p}_G$ and $u_e$, analogous to Eq. (2.6), it is necessary to consider the total volume that works as the storage of potential energy, namely, "capacitance". Because such a volume is nearly the clearance space V plus the volume of pipe $fl$, we can assume the following equation instead of Eqs. (2.1) and (2.6):

$$\dot{p}_G = \frac{\kappa p_0}{l} \frac{u_e}{1+V/fl} \tag{2.7}$$

In Eq. (2.2) which concerns the "inductance", if the terms of $\partial u/\partial t$ and $\partial p/\partial x$ are substituted by $du_e/dt$ and $-(p_e - p_G)/l$ respectively, then we can obtain the following equations from Eqs. (2.2) and (2.3):

$$\dot{u}_e = -\frac{1}{\rho_0 l}(p_e - p_G) - \frac{\lambda}{2d} u_e^2 \frac{u}{|u|} \tag{2.8}$$

Differentiating Eq. (2.7) and eliminating $u_e$ and $p_e$ from Eqs. (2.8) and (2.4), we can derive a kind of differential equation of forced vibration:

$$\left.\begin{aligned} &\ddot{p}_G + 2\vartheta|\dot{p}_G|\dot{p}_G + \omega_0^2 p_G = \omega_0^2 p_z \\ &\text{where} \\ &\omega_0 = \frac{a_0}{l\sqrt{1+V/fl}} \\ &\vartheta = \frac{1+V/fl}{4\kappa p_0}\left(\frac{1}{\mu^2} + \lambda\left(\frac{l}{d}\right)\right) \end{aligned}\right\} \tag{2.9}$$

It is noted that the left side of the above equation represents the usual mass and spring system with nonlinear damping force.

2) Frequency response

In order to derive the relationship between cylinder pressure and indicated pressure, a further analysis is made from the viewpoint of frequency response. For this purpose, we introduce the transfer function $G(j\omega)$, the ratio of the excess pressure in the clearance space $p_G-p_0$ to that in the cylinder $p_z-p_0$, where $\omega$ denotes angular frequency and $j=\sqrt{-1}$. The excess pressure $p-p_0$ and the velocity of fluid inside the passage u are, according to Binder and Hall[16],

$$p-p_o=\left[A\exp\left\{-(F+j\omega/a_o)x\right\}+B\exp\left\{(F+j\omega/a_o)x\right\}\right]\exp(j\omega t)$$

$$u=\frac{1}{\rho_o a_o}\left[A\exp\left\{-(F+j\omega/a_o)x\right\}-B\exp\left\{(F+j\omega/a_o)x\right]\exp(j\omega t)\right.$$

where A and B are constants and F denotes attenuation factor to friction damping of vibration per unit distance along the wall travel. If all nonlinear terms are ignored, A and B can be determined by the following boundary conditions; Eq. (2.6) for the outlet of the passage $x=\ell$, and $p-p_0=e^{j\omega t}$ for the inlet $x=0$. Thus we obtain

$$\begin{pmatrix}A\\B\end{pmatrix}=\frac{1\pm j\omega V/fa_o}{(1\mp j\omega V/fa_o)\exp\left\{\mp 2(F\ell+j\omega\ell/a_o)\right\}+(1\pm j\omega V/fa_o)}$$

According to Binder and Hall, the attenuation factor F is described in the following form.

$$F=\frac{1}{da_o}\sqrt{\frac{\omega}{\pi}\varepsilon}$$

where d denotes diameter of the passage, $\varepsilon$ kinetic viscosity modified by eddy-viscosity for a large amplitude wave. Denoting $4\varepsilon/\pi d^2=\gamma$ and using the above relationships, we reach the final expression as follows:

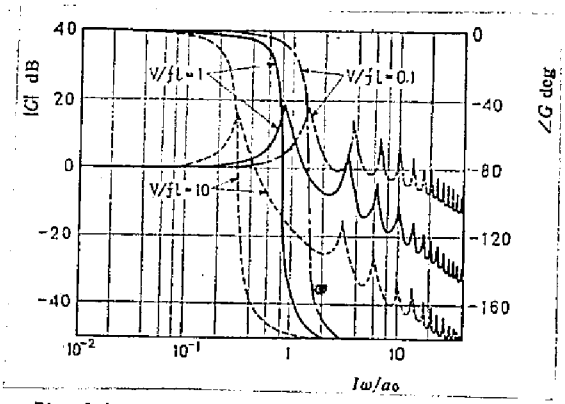


Fig. 2.2 Frequency response of adapter for various V/fl at $\zeta = 0.1$

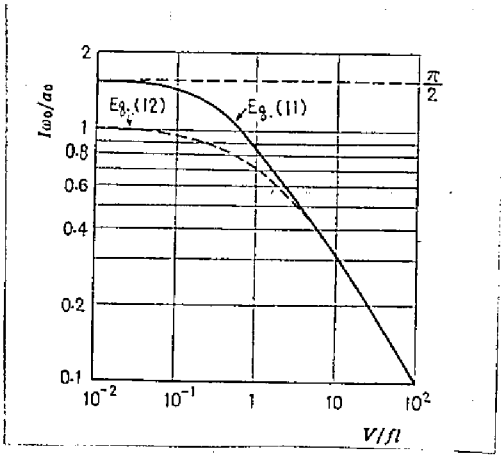


Fig. 2.3 Influence of V/fl on $l\omega_1/a_0$

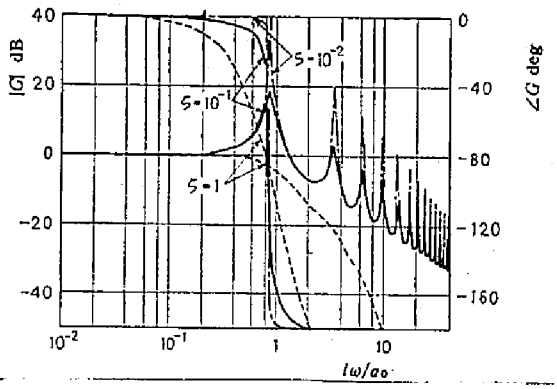


Fig. 2.4 Frequency response of adapter for various damping coefficients $\zeta$ at V/fl = 1

$$G(j\omega) = \frac{p_G - p_0}{p_z - p_0} = \frac{p_a - p_e}{p_e - p_0}$$

$$= \frac{1}{\cosh\left(\sqrt{\gamma l/a_0}\,\sqrt{\omega l/a_0} + j\omega l/a_0\right) + j\omega l/a_0 \cdot V/fl \cdot \sinh\left(\sqrt{\gamma l/a_0}\,\sqrt{\omega l/a_0} + j\omega l/a_0\right)} \quad (2.10)$$

There are two non-dimensional parameters in this formula: namely, $V/fl$ and $\sqrt{\gamma l/a_0} = \zeta$. Here they are designated as the volume ratio of the clearance space and the non-dimensional damping coefficient respectively. In order to know the effect of those parameters on the characteristics of an adapter, the frequency response was calculated from Eq. (2.10).

Fig. 2.2 shows the effect of volume ratio $V/fl$ on the frequency response, with $\zeta = \sqrt{\gamma l/a_0} = 1/10$. It can be seen that the passage acts as a sort of "comb type filter". Frequency where the argument $\angle G$ is delayed by $90^\circ$ exactly corresponds to $\omega_0$ of Eq. (2.9) in which parameters are lumped to one-degree-of-freedom, so that the same notation is adopted here. By setting the dominator of Eq. (2.10) to be naught, an equation to find out $\omega_0$ is derived as follows:

$$\frac{V}{fl}\,\frac{l\omega_0}{a_0}\tan\frac{l\omega_0}{a_0} - 1 = 0 \quad (2.11)$$

As can be seen from above, the frequency $\omega_0$ is a function of $V/fl$ and independent of the damping coefficient. In Fig. 2.3 is shown the relationship between $l\omega_0/a_0$ and $V/fl$ calculated from Eq. (2.11), together with that from Eq. (2.9), that is,

$$\frac{l\omega_0}{a_0} = \frac{1}{\sqrt{1 + V/fl}} \quad (2.12)$$

The error caused by lumping parameters is remarkable when $V/fl$ is lower than the unity; namely, when $V/fl$ approaches to naught, Eqs. (2.11) and (2.12) give $l\omega_0/a_0 = \pi/2$ and 1 respectively. However, when $V/fl$ is far larger than unity, only a small discrepancy is noticed between them.

Fig. 2.4 represents the effect of damping where the volume ratio is kept constant at the unity. In the case of $\zeta$ being $10^{-2}$ and $10^{-1}$, the response shows deficient damping and in the case of unity it shows an excessive damping. A treatment with such a linearized damping force, however, involves a possibility of leading to misjudgement, so that more careful treatment is required.

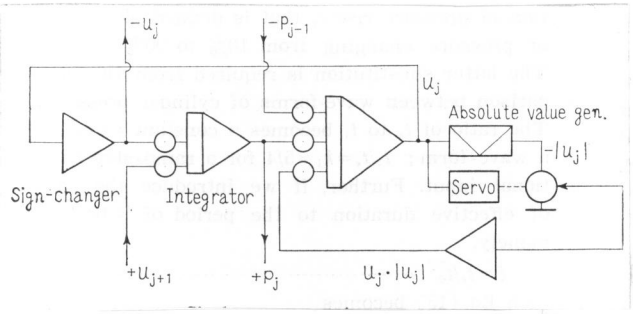


Circles are potentiometers.

Fig. 2.5 Analog circuit of a pipe section

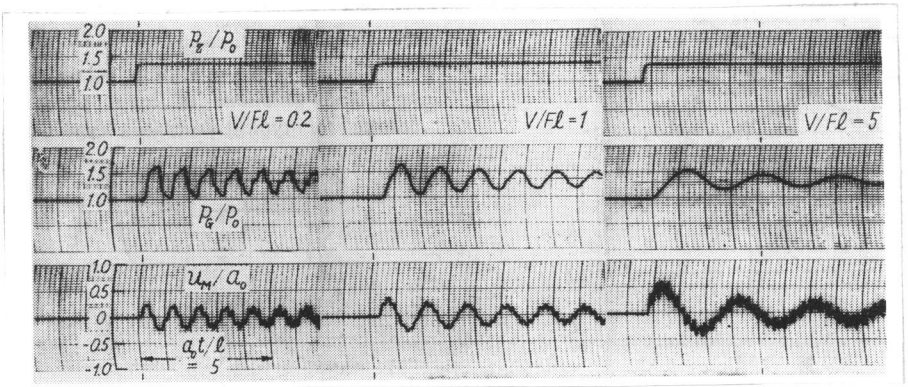


$p_z$: cylinder pressure, $p_G$: pressure in the clearance space, $u_M$: gas velocity at the middle way of the passage.

Fig. 2.6 Transient response of adapter, calculated by using the analog computer

3) Transient response

It is then of importance to evaluate nonlinear damping effects such as the frictional force of the canal and the boundary conditions of Eqs. (2.4) and (2.5). A study of the transient pressure change in $p_G$ for a step-functional input with a complete description of Eqs. (2.1) to (2.6) is quite feasible with an electric analog-computer. Solving the partial differential equations (2.1) and (2.2) is submitted to the space derivatives, thus first order ordinary differential equations with time as an independent variable is obtained. Consider $m$ as the number of divisions, and the equations thus transformed will become the following formulae as regards the $j$-th element of pipe section:

$$\left.\begin{aligned} \dot{p}_j &= \frac{m\rho_0 a_0^2}{l}(u_j - u_{j+1}) \\ \dot{u}_j &= \frac{m}{\rho_0 l}(p_{j-1} - p_j) - \frac{\lambda}{2d} u_j^2 \frac{u_j}{|u_j|} \\ &\qquad [j = 1, 2, \cdots\cdots m] \end{aligned}\right\} \qquad (2.13)$$

The analog-computer circuit of Eq. (2.13) is schematically shown in Fig. 2.5. Beside the main loop consisting of two integrators and a sign changer, there is a sub-loop for simulating the nonlinear frictional force, which includes an absolute value generator and a servo-multiplier. For realization of the boundary conditions of Eqs. (2.4) and (2.5), there inserted, in the terminal circuits, additional similar sub-loops which have in them gate-circuits for materializing the inequality due to the gas flow direction. Because of size of the computor available for the study (which was originally constructed as nuclear reactor simulator at Kyoto University), the number of divisions was five.

Some results for various volume ratios are shown in Fig. 2.6 in which a sudden pressure rise by $\Delta p$ in cylinder is assumed to take place. The numerical values for the computation were:

| | |
|---|---|
| The ratio of the pressure rise in cylinder to the initial pressure at rest | $\Delta p/p_0 = 0.35$ |
| Passage length to diameter ratio | $l/d = 20$ |
| Friction coefficient | $\lambda = 0.020$ |
| Flow coefficient at inlets of the canal | $\mu = 0.80$ |

In oscillograms pressures in cylinder and in clearance space are recorded in non-dimensional forms, namely, as $p_E/p_0$ and $p_G/p_0$ respectively. Besides

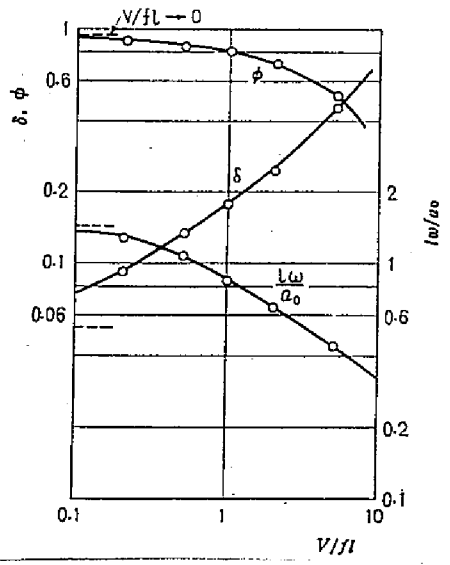


Fig. 2.7 Calculated values of $l\omega/a_0$ , overshoot ratio $\phi$, and logarithmic attenuation factor $\delta$

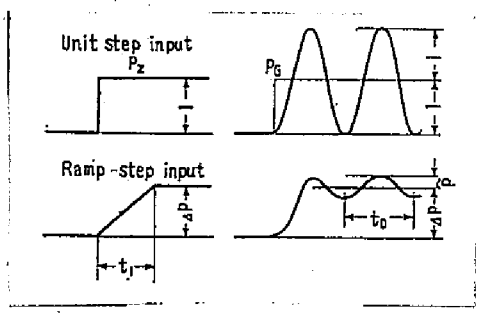


Fig. 2.8 Nomenclature

them, the non-dimensional gas velocities at the middle position of the canal, namely, $u_M/a_o$, are presented. The shape of the output $p_G$ is in close proximity to a square waveform for $V/fl$ =0.2 and to a sinusoidal wave-form for $V/fl$ =5. This is due to the fact that distribution of phase in the canal becomes uniform with an increasing $V/fl$, thus resulting in the disappearance of higher components in $p_G$. And its transient nature becomes very similar to a one-degree-of-freedom lumped parameter system if the influence of the higher components on the shape of pressure response is tolerated.

Fig. 2.7 shows the computed values of the non-dimensional angular frequency $lw/a_o$, the mean logarithmic damping factor $\delta$ and the non-dimensional over-shoot $\phi$, in relation with $V/fl$. The last variable $\phi$ denotes the ratio of the over-shoot pressure $\tilde{p}$ at first oscillation cycle to the pressure rise $\Delta p$. Considering that an ideal system without loss holds to be $\delta$ =0 and $\phi$ =1 for any $V/fl$, we may conclude that the effect of damping factors increases with $V/fl$ and that the damping effect can be safely ignored for smaller $V/fl$ than, for instance, 1.0.

4) Effect of development of cylinder pressure upon pressure vibration

In the case of a small ratio of clearance space, as has be seen above, the damping effect of pressure vibration can virtually be ignored and at the same time an approximation to a lumped parameter system is acceptable if $\omega_o$ is properly corrected and if the wave-form of response is not considered. Owing to the fact that the governing equation becomes linearized in such a case, the influence of development of cylinder pressure $p_t$ upon the amplitude of pressure oscillation in $p_G$ can be known.

If the damping coefficient in Eq. (2.9) is neglected, then the transient response $p_G^*$ for the unit step function is

$$p_G^*(t) = 1 - \cos \omega_o t \qquad [t \geq 0] \tag{2.14}$$

Consequently, the treatment will become completely identical to that of Section 1.3, if several notations are properly modified, and if $x_o$ is assumed to be unity. First of all, $p_G$ and $p_G^*$ correspond to x and x* respectively, and $\omega_o$ signifies the angular frequency of pressure oscillation. Fig. 2.8 illustrates new notations employed in this chapter; the amplitude of oscillation $\tilde{p}$ is related to $\tilde{x}$ and the magnitude of pressure rise $\Delta p$ with $x_s$.

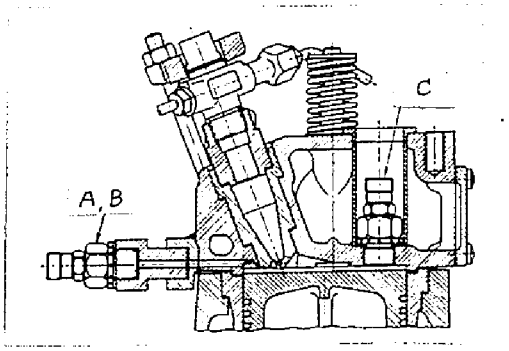


Fig. 2.9 Cross-sectional view of the combustion chamber arranged with pressure pick-ups with adapters (A and B) and directly flush to the wall (C)

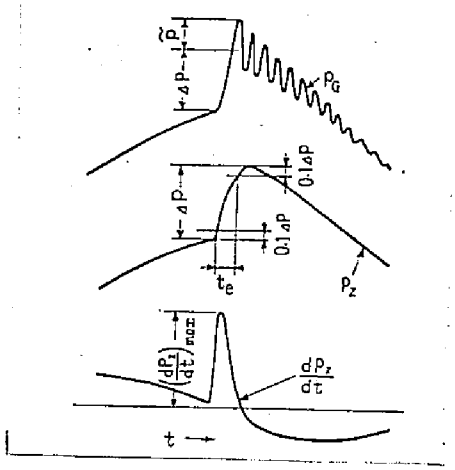


Fig. 2.10 Analysis of indicator diagram

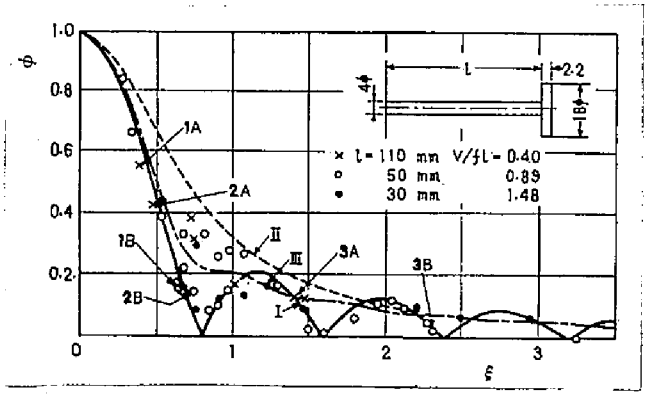


Fig. 2.11 Non-dimensional amplitude $\phi$ versus rising time ratio $\xi$

If $t_e$, $t_o$ and $\xi$ are defined similarly as effective rising time, period of vibration and ratio of them respectively, then the relationship between $\xi$ and $\phi = \bar{p}/\Delta p$ completely accords with the expressions presented in Table 1.1. Therefore the previous conclusions are all valid on the effect of course of pressure on the pressure vibration induced in the adapter.

## 2.3 Evaluation of Errors in the Indicator Diagrams

### 1) Experimental apparatus

In order to testify the aforementioned theories and to obtain the knowledge of the damping effect of pressure vibration, experiments were carried out with a four-cycle diesel engine of pre- chamber type (cylinder diameter and stroke 95mm and 115 mm resp.). As shown in Fig. 2.9, two pressure pick-ups with passages are set up to the main combustion chamber and another one for reference is set flush directly with the cylinder wall for obtaining a distortion-free diagram. They were all strain gage type (Kyowa-Dengyo, PHF-7B). The engine was operated under a light load or without any load so that a high temperature gas might not penetrate into these passages.

Either an electromagnetic oscillograph or a cathode-ray tube oscillograph was used for recording. In the former, special caution was taken to maintain necessary frequency characteristics of the electromagnetic vibrators (B-type of Yokogawa Electric Works) and their gains were adjusted so as to drop by 3 dB at as high as 7 kc/sec.

### 2) Effect of pressure development on the accuracy of diagrams

Passages of three different lengths were experimented for obtaining the relation between the cylinder pressure and the pressure vibration caused. The temperature of cooling water was properly controlled so as to realize a desirable duration of pressure rise. This duration was measured from the pressure diagrams in the manner as illustrated in Fig. 2.10, where $\phi$ was calculated from the overshoot caused by the transient pressure change. The plots of the relationship between $\phi$ and $\xi = t_e/t_o$ were summarized in Fig. 2.11. It can be seen that their plots correlate on the whole with the theoretical curves and that the over-shoot ratio $\phi$ decreases with the rising time $t_e$ and becomes within 10% when $\xi$ is higher than two. Fig. 2.12 shows

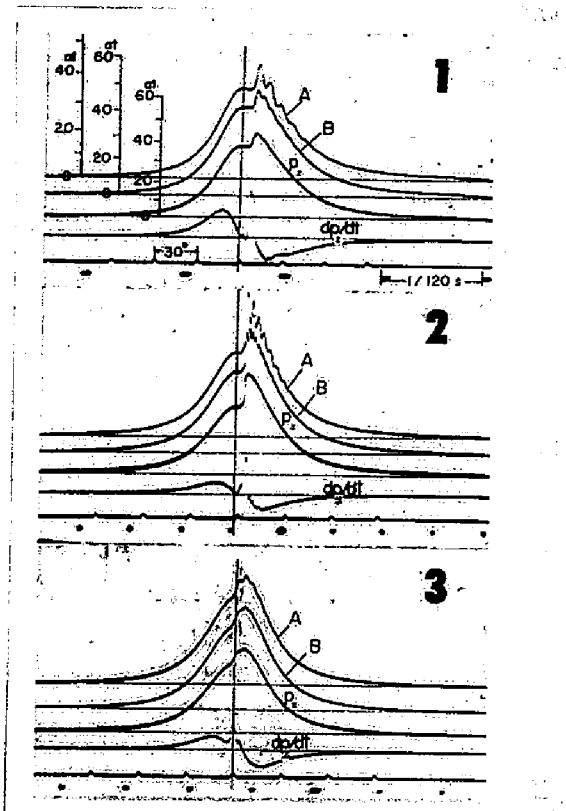


A: $l$=110 mm, $V/fl$=0.40
B: $l$=50 mm, $V/fl$=0.89

| No. | $\omega_0/2\pi$ c/sec | $t_c$ msec | $\xi$ $(=t_c/t_0)$ | $\theta_0$ deg | $\bar{p}$ kg/cm² | $\Delta p$ kg/cm² | $\phi$ $(=\bar{p}/\Delta p)$ | $p_0$ kg/cm² | $dp_z/d\theta$ kg/cm²/deg | $n$ rpm |
|---|---|---|---|---|---|---|---|---|---|---|
| 1 A | 1 280 | 0.31 | 0.40 | 6.7 | 2.5 | 7.6 | 0.55 | | | |
| B | 1 970 | 0.31 | 0.62 | 4.3 | 0.9 | 7.6 | 0.16 | | | |
| $p_z$ | — | 0.31 | — | — | — | 7.6 | — | 37.4 | 2.2 | 1 420 |
| 2 A | 1 220 | 0.37 | 0.45 | 3.2 | 6.1 | 15.9 | 0.42 | | | |
| B | 2 050 | 0.37 | 0.76 | 1.9 | 1.7 | 15.9 | 0.13 | | | |
| $p_z$ | — | 0.37 | — | — | — | 15.9 | — | 37.7 | 8.6 | 650 |
| 3 A | 1 230 | 1.16 | 1.42 | 3.9 | 1.0 | 6.2 | 0.12 | | | |
| B | 2 000 | 1.16 | 2.32 | 2.4 | 0.4 | 6.2 | 0.05 | | | |
| $p_z$ | — | 1.16 | | — | — | 6.2 | — | 37.1 | 2.0 | 800 |

Fig. 2.12 Examples of indicator diagrams

typical pressure diagrams each of which involves three pressure-time traces simultaneously taken in different ways; namely, the case using an adapter of length $\ell$ =110 mm (denoted as "A" in Card), the case of $\ell$=50 mm (denoted as "B"), and the case of direct measurement. The corresponding plots are shown with numbering in the $\phi$ versus $\xi$ diagram of Fig. 2.11 and their data are shown in the attached table. Cards 1 and 2 are examples of almost the same magnitude of $\xi$ and $\phi$ but largely differ in the engine speed. Maximum pressure can possibly be estimated from Card 2 by joining smoothly each of neighboring centers of pressure vibration. But, in Card 1, the vibration is too coarse to apply such a method in measuring the maximum pressure. For this reason, the primary requirement for the pressure record is that the frequency of vibration relative to the engine speed is to be raised above an allowable value. In the table is shown the period of vibration in crank angle $\theta_0$ (n: engine speed in rpm, $t_0$: period of vibration in msec) against each pressure curve. By comparing these values with the pressure patterns, we can deduce that, if $\theta_0$ is less than 2°, the real pressure development can be tolerably estimated from the diagram taken by the use of the adapter, while it is difficult if $\theta_0$ is more than 3°. By the way, Card 3 shows pressure-time records with large values of $\xi$. In the case of 3B, the pressure through a passage follows the actual course of pressure fairly well. Consequently, a reliable pressure diagram is expected when the condition that $\xi$ is more than 2 is fulfilled.

3) Considerations on available range of an adapter

The natural frequency of the passage prescribes the upper limit of the frequency spectrum of the measured pressure, so that the natural frequency must be raised as high as possible. Speaking from the viewpoint of installation of a pressure sensitive element, however, a longer passage will be desirable in most cases. Consequently, there arises a problem to know the availability of the passage for a given length.

As one of the parameters describing the suitability of the passage, the ratio of the rising time to the period of vibration $\xi(=t_e/t_0)$ has been adopted. But, because the rising time $t_e$ is not a very familiar variable, it is rewritten by using some well-known variables such as the maximum rate of pressure rise $(dp/d\theta)_{max}$ and the magnitude of pressure rise $\Delta p$. Their standard values can be known from the knocking and the strength of

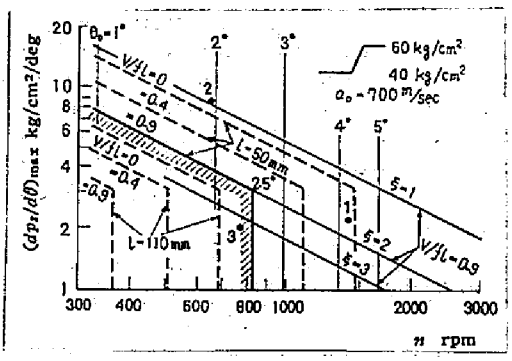


Fig. 2.13 Estimation of available range of an adapter

structure respectively. Provided that the course of the cylinder pressure is of ramp-step function, the maximum rate of pressure rise measured by the actual time $(\dot{p})_{max}$ is, according to the definition of the rising time, as follows:

$$(\dot{p})_{max} = \frac{\Delta p}{t_1} = \frac{\Delta p}{k_1 t_e}, \qquad k_1 = 5/4 \tag{2.15}$$

By using the relation $d\theta/dt=6n$, where n is the engine speed, the rate of pressure rise is expressed on the crank angle basis. Eliminating $t_e$ and $t_o$ from the relations $t_o=2\pi/\omega_o$ and $\xi = t_e/t_o$, we obtain

$$\frac{\omega_o}{2\pi} = \frac{15}{2} \frac{n}{\Delta p} \xi \left(\frac{dp_z}{d\theta}\right)_{max} \qquad \text{c/sec} \tag{2.16}$$

Now, we consider an indicator passage whose diamensions are $l$ =50 mm and V/fl = 0.9, and assume that $p_z$ changes from 40 kg/cm$^2$ to 60 kg/cm$^2$ and that the sound velocity before the pressure rise occurs is $a_o$ =700 m/sec. In this condition, the non-dimensional frequency $l\omega_o/a_o$ is estimated to be 0.893 from Eq. (2.11), so that the natural frequency of the passage $\omega_o/2\pi$ amounts to 1990 c/sec. Considering that the magnitude of pressure rise $\Delta p$ is 20 kg/cm$^2$, Eq. (2.16) is then reduced to

$$5.31 = \left(\frac{n}{1000}\right) \xi \left(\frac{dp_z}{d\theta}\right)_{max} \tag{2.17}$$

Fig. 2.13 shows the relationship between the engine speed and the maximum rate of pressure rise, in which Eq.(2.17) is expressed in fine solid lines for various values of $\xi$, together with the period of vibration measured on crank angle $\theta_o$. The hatched part in the diagram gives such a domain as is able to measure the pressure with this passage, where $\xi>2$ and $\theta_o<2.5^\circ$ as assumed from the experimental results as the allowable limits. Besides, plots of 1, 2 and 3 correspond to the running conditions of Indicator Cards 1,2 and 3 of Fig. 2.12. The fact that plots 1 and 2 are out of the hatched domain but the plot 3 is in it, seems to fairly agree with what was deduced from the experimental results; namely, 1B is poor because of too high speed, 2B because of too large amplitude of pressure vibration, and 3B is the card taken with an adequate condition. Judging from these, it will be concluded that the availability of a passage can be examined through this procedure. In the same diagram, the limits for volume ratios V/fl=0 and 0.4 are presented on the same conditions for the

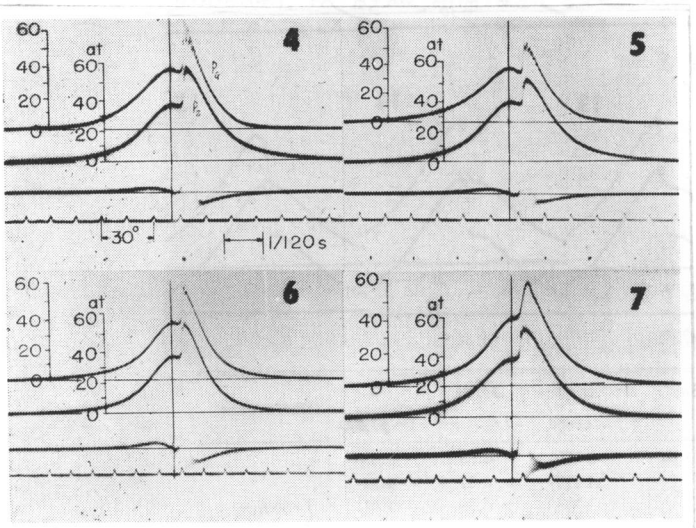


| No. | $d$ mm | $V/fl$ | $\omega/2\pi$ c/sec | $\xi$ | $\hat{p}$ kg/cm² | $n$ rpm |
|---|---|---|---|---|---|---|
| **4** | 4.0 | 1.54 | 3 150 | 0.80 | 8.2 | 460 |
| **5** | 2.2 | 5.14 | 2 150 | 0.71 | 2.2 | 490 |
| **6** | 1.45 | 11.7 | 1 430 | 0.50 | 1.1 | 380 |
| **7** | 0.9 | 30.5 | 715 | 0.35 | 0.2 | 490 |

$l = 31$ mm, $V = 0.60$ cm³

**Fig. 2.14 Vibration absorbing by narrowing the passage**

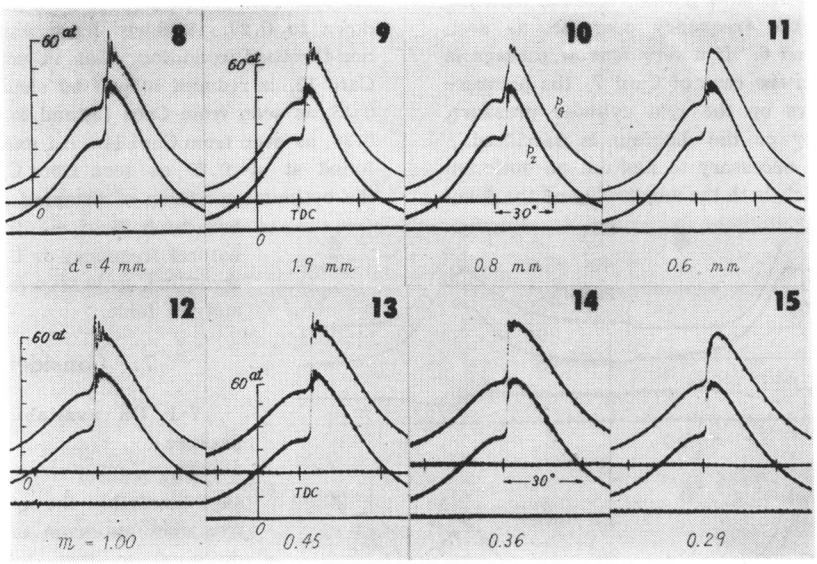


| No. | $d$ mm | $m$ | $\omega/2\pi$ c/sec | $\Delta p/p_0$ | $\phi$ $(=\hat{p}/\Delta p)$ | Reference |
|---|---|---|---|---|---|---|
| **8** | 4.0 | 1.00 | 1 570 | 0.58 | 0.39 | |
| **9** | 1.9 | | 1 410 | 0.54 | 0.22 | |
| **10** | 0.8 | | 1 340 | 0.55 | 0.07 | $l = 50$ mm |
| **11** | 0.6 | | 1 210 | 0.57 | — | $V/fl = 1.1$ |
| Average | | | | 0.56 | | |
| **12** | 3.0 | 1.00 | 1 720 | 0.73 | 0.37 | |
| **13** | | 0.45 | 1 720 | 0.74 | 0.20 | $l = 50$ mm |
| **14** | | 0.36 | 1 580 | 0.69 | 0.08 | $V/fl = 0.144$ |
| **15** | | 0.29 | — | 0.69 | — | $l/d = 16.7$ |
| Average | | | | 0.71 | | |

**Fig. 2.15 Vibration absorbing (a) by narrowing the passage under constant V/fl (Card 8 to 11) and (b) by throttling (Card 12 to 15)**

passage lengths $\ell$ =50mm and 110 mm. Because the point 1 is on the safe side when $V/f\ell=0$ at $\ell$ =50 mm, the Indicator Diagram 1B will probably be converted into a satisfactory diagram if the clearance space of the adapter is reduced to be very small. In the case of $\ell$ =110 mm, however, no satisfactory results will be expected when the measurement is intended to be made with any condition of 1, 2 or 3.

4) Improvement of accuracy by absorbing the pressure vibration

In order to evaluate the effectiveness of absorbing the pressure vibration, several kinds of indicator passages were prepared. In this investigation, the following three methods were taken up: namely, (1) narrowing the passage at a constant clearance volume, (2) narrowing the passage at a constant $V/f\ell$ and (3) throttling the inlet.

First of all, a number of indicator diagrams were obtained with various diameters of the passage d at a constant clearance volume V= 0.6 $cm^3$. Cards 4 to 7 in Fig. 2.14 show pressure records obtained. Through visual observation there is no great variation among pressure developments of cylinder $p_z$. Card 4 involves a pressure curve taken with the use of a passage having a relatively large diameter. In this case the amplitude and the frequency of pressure vibration are large. As the diameter of the passage is reduced, both the amplitude and the frequency decrease, as seen from Cards 5 and 6. If a very narrow passage is once used, as in the case of Card 7, the pressure no longer follows up the real cylinder pressure, and the accuracy of the diagram is sacrificed. Therefore, it is necessary to find out an optimum diameter at which both the amplitude and the delay are minimum, and we can recognize that Card 6 almost fulfills this condition.

Since the passage was narrowed at a constant clearance volume in the above mentioned experiment, the volume ratio $V/f\ell$ at the optimum condition came up to a large value, thus leading to a low natural frequency of pressure vibration. Consequently there arises a question whether or not it is possible to absorb the vibration without any increase in $V/f\ell$. In order to find out the solution, a test was made at the constant volume ratio. Some pressure diagrams are shown in Fig. 2.15 (a), for the case of $V/f\ell=1$ and $\ell$=50 mm. As can be seen from Card 10, a very small amplitude of oscillation is materialized with a 0.8 mm-diameter passage. Moreover, the decrease in the natural frequency

is not large, as seen from the table.

Another damper was the throttle placed at the passage inlet of the combustion chamber side. Indicator Cards 12 to 15 were obtained by varying the area ratio of throttle to passage m from unity down to 0.29. A fairly large amplitude in the non-throttled condition, that is corresponding to Card 12, is reduced to half by changing m below 0.45, as seen from Card 13, and to a quarter with 0.36, as seen from Card 14. An excessive delay is found at m=0.29 as seen from Card 15. Hence the optimum condition of damping is considered to be near 0.36 of m. In addition, the natural frequency is little affected by throttling, as is seen from those Cards and the table.

5) Estimation of optimum condition of absorbers

As has been reported previously, if the degree of vibration absorbing exceeds a limit, an improvement in accuracy by reducing the amplitude of oscillation will be spoilt because of a long time of the indicated pressure in following up the real cylinder pressure, thus causing some inaccurate pressure diagrams such as Cards 7, 11 and 15. Hence there is an optimum condition in the degree of vibration absorbing. As seen from Eq. (2.9), however, the damping term of the equation governing the gas system inside the passage is so strongly nonlinear that we cannot find out this condition in general. Fortunately, in the special case where the cylinder pressure is assumed to develop step-functionally, we can approximately estimate the optimum by putting the following assumptions: namely, that the optimum damping holds merely when the cylinder pressure is changing, and that, under the optimum damping condition, the rate of pressure rise of output $p_G$ is nearly constant during the pressure rise. If, in the second term of Eq. (2.9), $|\dot{p}_G|$ is assumed to be constant, then the equation governing pressure in the clearance space becomes a linear differential equation as follows:

$$\ddot{p}_G + 2\{\vartheta(\dot{p}_G)_M\}\dot{p}_G + \omega_0^2 p_G = \omega_0^2 p_2 \qquad (2.18)$$

where $(\dot{p}_G)_M$ is the average rate during the pressure rise. The mode of response is determined from the relative magnitude of the damping coefficient, namely,

$$\left.\begin{array}{ll} \vartheta(\dot{p}_G)_M/\omega_0 < 1 & \text{Vibrational response} \\ =1 & \text{Critical damping} \\ >1 & \text{Non-vibrational response} \end{array}\right\} \qquad (2.19)$$

Consequently, the critical damping condition for the present case clearly depends on the choice of the mean rate of pressure rise. In order to give it a reasonable value, we consider about the duration of pressure rise at the optimum damping. In the case of a non-loss system ($\vartheta=0$), it takes a quarter of the period of oscillation, i.e. $t_0/4$, for the response $p_G$ to change from the initial pressure $p_0$ to the equilibrium pressure $(p_0+\Delta p)$. Consequently, we can make the assumption that, in the system submitted to some degree of damping force, this duration cannot be less than $t_0/4$. Hence, the upper limit of the mean rate of pressure rise is

$$(\dot{p}_G)_M < \frac{\Delta p}{t_0/4} = (2/\pi)\,\Delta p\omega_0 \qquad (2.20)$$

If an arbitrary value less than the right hand side of this relation is given to $(\dot{p}_G)_M$, there is a chance to cause an excessive damping because the smaller value of $(\dot{p}_G)_M$ will give the higher degree of damping. On the contrary, if the upper limit is used, then the response will be of somewhat poor damping but never of an excessive one; namely, it is always on the safe side. The critical damping condition thus safely estimated is then described from Eq. (2.19), as follows:

$$\vartheta(2/\pi)\Delta p = 1$$

or, according to Eq. (2.9),

$$(1+V/fl)\left\{\frac{1}{\mu^2}+\lambda\left(\frac{l}{d}\right)\right\} = 2\pi k\,\frac{p_0}{\Delta p} \qquad (2.21)$$

By solving this equation, we can predict the optimum throttle ratio m in the experiment of the throttle damper. In this case, the flow coefficient $\mu$, in the above equation, is replaced by $\mu m$ and the following numerical values are given.

$$\Delta p/p_0 = 0.71, \qquad V/fl = 0.144, \qquad l/d = 16.7,$$
$$k = 1.40, \qquad \lambda = 0.020, \qquad \mu = 0.80.$$

Then we obtain m=0.39. This value roughly agrees with the throttle ratio of Indicator Card 14, that is, m=0.36, where the measured pressure was described almost to be in the optimum damping condition. As regards the

other type absorbers, Eq. (2.21) may be applied in estimating the optimum damping condition, if an accurate value of the friction coefficient $\lambda$ is once known.

## 2.4 Conclusion

As the result of the theoretical and experimental study on the indicator adapter for the cylinder pressure measurement, the following conclusions are obtained:

(1) The passage works as a comb-type filter in transmitting the cylinder pressure to the pressure sensitive element. The magnitude of pressure amplitude caused by a pressure rise in cylinder is decided by the ratio of the rising time to the period of oscillation, if the effect of damping is not considered.

(2) A distortion-free diagram can be safely gained by using an indicator passage if the rising time of pressure is twice the period of gas oscillation and if the crank angle of the period of oscillation is less than two.

(3) Concerning the availability of the vibration absorbers: Extreme narrowing of the passage at a constant volume ratio of clearance space to the passage makes it possible to effectively absorb the oscillation without a large sacrifice in the frequency. Throttling is also effective as a mean of suppressing vibration. Moreover, an approximate method of finding out the optimum damping condition was derived against a step-functional pressure change occurring in the cylinder.

## CHAPTER 3

## Influence of Connecting Passage on Combustion Noise in Divided Chamber Type Diesel Engines

### 3.1 Purpose of the Study

According to CHAPTER 1, the combustion noise of a diesel engine is originated by some mechanical cause involved with a sharp pressure rise in the main combustion chamber. As regards the pre-chamber type engine, the pressure rise in the main chamber is the key to determining the intensity of the combustion noise, rather than the course of pressure in the pre-chamber, which, of course, has a close connection with the pressure in the main chamber. This fact is also supported by Nagao and others[17]. Hence, it may be stated as the general tendency of the noise formation in the divided chamber type diesel engine that the rate of pressure rise in the main chamber is determined by the rate of heat release in it as well as by the transmission of the sharp pressure rise in the auxiliary chamber into the main chamber. How the latter influences the pressure rate in the main chamber will be closely concerned with the cross-sectional area of the connecting passage.

In this study, this effect is theoretically investigated by introducing idealized models. Firstly, on the assumptions that the process is quasi-static and that a step-functional pressure rise happens in the auxiliary chamber, the influence of the area of the connecting passage on the pressure development is evaluated and then experimentally by an air tank that simulates the main combustion chamber. As the second stage of the study, a thin water sheet is applied to reveal the phenomena of pressure wave propagation from the auxiliary chamber to the main chamber as well as that taking place in the main chamber. Finally, based on these results, considerations are made on the maximum rate of pressure rise in the actual engine.

### 3.2 Quasi-Static Pressure Development in the Main Chamber

#### 1) Idealized system of the combustion chamber

At first, the following model of combustion chamber system was con-

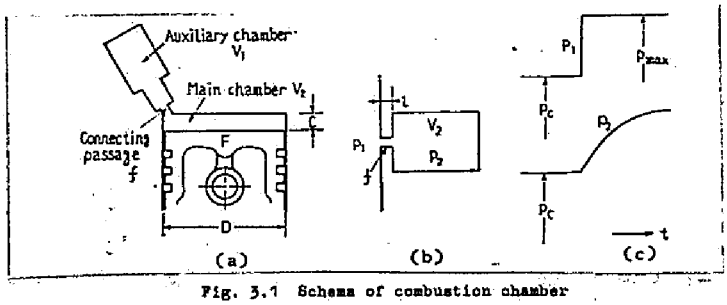


Fig. 3.1 Schema of combustion chamber

sidered: The occurrence of the sharp pressure rise due to combustion being usually confined to the neighborhood of the top dead center of crankshaft, the space of the main combustion chamber virtually remains constant during the combustion. The pressure jumps step-functionally in the auxiliary combustion chamber, although its actual course may be too complicated in nature to be calculated. There is no heat release in the main chamber. And, after the pressure jumps in the auxiliary chamber, the pressure in this chamber is held constant.

The state of main chamber under these assumptions is analogous to that of an evacuated tank being filled with air through an entrance from the surrounding of the infinite space. Fig. 3.1 illustrates the actual system (a) and the analogous system (b). The present problem is then reduced to finding out the pressure response in such a tank where the pressure at the inlet is suddenly changed.

The relationship between pressures in the auxiliary chamber $p_1$, whose space volume $V_1$ is infinite for the present case, and in the main chamber $p_2$, can be derived from the mass-and the energy-equilibriums of gas flowing in through the connecting passage whose cross-sectional area is denoted as f. Consequently, the quantity of gas transferred dG at an infinitesimal duration dt can be expressed as follows:

$$dG = \mu f \sqrt{2g \frac{p_1}{v_1}} \sqrt{\frac{\kappa}{\kappa-1}\left\{\left(\frac{p_2}{p_1}\right)^{2/\kappa} - \left(\frac{p_2}{p_1}\right)^{(\kappa+1)/\kappa}\right\}} \cdot dt \qquad (3.1)$$

where, $g$: acceleration of gravity, $v_1$: specific volume of gas in the auxiliary chamber, $\mu$: flow coefficient, $\kappa$: ratio of specific heats of gas.

If pressure in the main chamber rises by $dp_2$ due to the gas inflow dG, the energy balance equation may be represented as follows:

$$dG = \frac{V_2}{\kappa R T_1} \cdot dp_2 \qquad (3.2)$$

where, $V_2$: volume of the main chamber, $T_1$: temperature in the auxiliary chamber, R: gas constant. Eliminating dG in Eqs. (3.1) and (3.2), we obtain the final relation,

$$\frac{dp_2}{dt} = \frac{\sqrt{2\kappa a_1 p_1}}{D} \cdot \frac{\mu f D}{V_2} \times \sqrt{\frac{\kappa}{\kappa-1}\left\{\left(\frac{p_2}{p_1}\right)^{2/\kappa} - \left(\frac{p_2}{p_1}\right)^{(\kappa+1)/\kappa}\right\}} \qquad (3.3)$$

where D is the cylinder diameter and $a_1$ is the sound velocity in the auxiliary chamber ($a_1=\sqrt{kgRT_1}$). Denoting the pressure and the sound velocity before combustion as $p_c$ and $a_c$ respectively, and adopting them as a reference state, we can rearrange Eq. (3.3) to give

$$\frac{d}{dt}\left(\frac{p_2}{p_c}\right)=\frac{\sqrt{2k}K_0}{t_0}\frac{a_1}{a_c}\frac{p_1}{p_c} \times\sqrt{\frac{\kappa}{\kappa-1}\left\{\left(\frac{p_2}{p_1}\right)^{2/\kappa}-\left(\frac{p_2}{p_1}\right)^{(\kappa+1)/\kappa}\right\}} \tag{3.4}$$

where,

$$\left.\begin{aligned} K_0 &= \mu f D/V_2 \\ t_0 &= D/a_c \end{aligned}\right\} \tag{3.5}$$

$K_0$ is a non-dimensional number characterized by the geometry of the combustion chamber, containing the cross-sectional area of the connecting passage; $t_0$ represents the unit of time. In this case, cylinder diameter D is not necessary for the present analysis because the uniformity of pressure inside the combustion chamber is assumed here and no attention is paid to the phase distortion of pressure due to gas inertia. Eq. (3.5) has been presented only for giving a room for some further discussion on such a transient process. Consequently, the present treatment will be limited to a study using a ratio of them: namely,

$$K=\frac{\sqrt{2k}K_0}{t_0} \qquad \sec^{-1} \tag{3.6}$$

Thus the maximum rate of pressure rise, caused by a rapid pressure rise in the auxiliary chamber, is derived by putting in Eq. (3.6) the relations of $p_1=P_{max}$ and $p_2=p_c$, as follows:

$$\left[\frac{d(p_2/p_c)}{dt}\right]_{max}=K\left(\frac{a_1}{a_c}\right)\left(\frac{p_{max}}{p_c}\right) \times\sqrt{\frac{k}{\kappa-1}\left\{\left(\frac{p_c}{p_{max}}\right)^{2/\kappa}-\left(\frac{p_c}{p_{max}}\right)^{(\kappa+1)/\kappa}\right\}} \tag{3.7}$$

This formula yields the maximum rate of pressure rise as a function of K, and means that the maximum rate due to the inflow of gas into the main chamber does not exceed a definite value given by the coefficient K.

As Eq. (3.4) refers to the case of a quasi-static inflow of gas, so the pressure in the main chamber $p_2$ will approach asymptotically to $P_{max}$

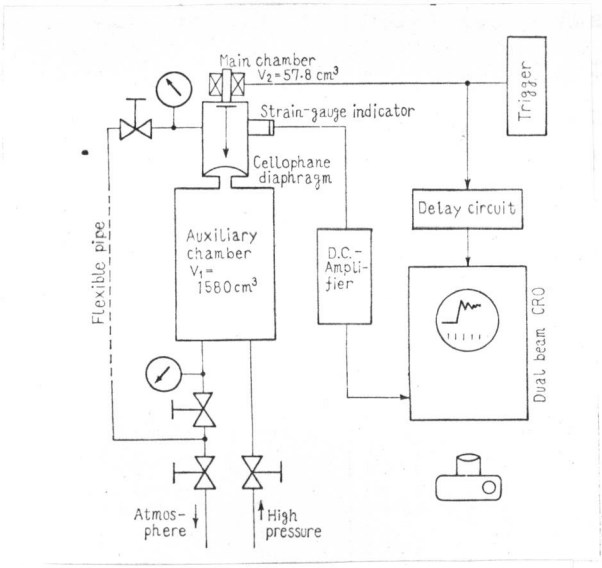


Fig. 3.2 Experimental arrangement for realizing a sudden pressure rise in the main chamber

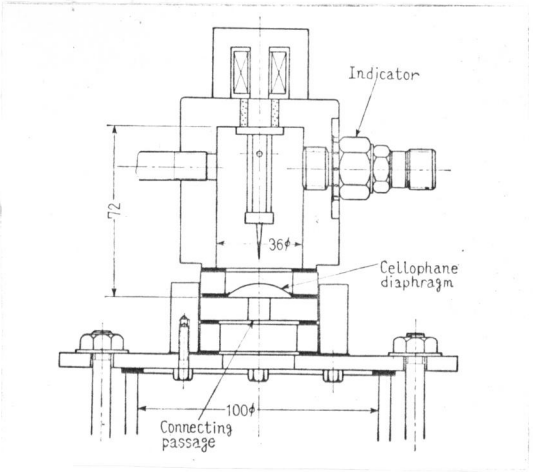


Fig. 3.3 Details of main-chamber tank

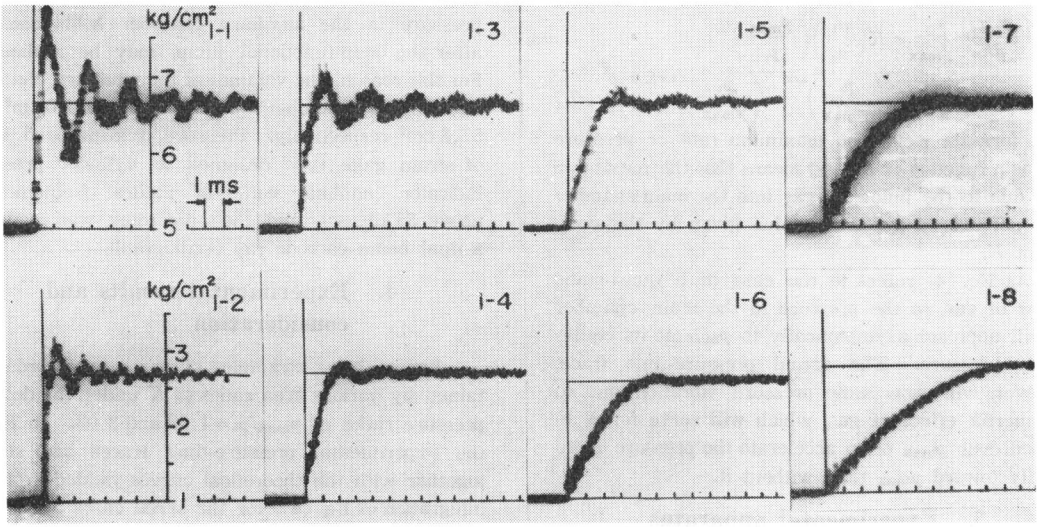


| No. | K $sec^{-1}$ | $p_{max}/p_c$ | $d(p_2/p_c)/dt$ $sec^{-1}$ Theoretical | Measured | $t_e$ sec |
|---|---|---|---|---|---|
| 1-1 | $19.1 \cdot 10^2$ | 1.39 | $11.7 \cdot 10^2$ | $11.8 \cdot 10^2$ | $0.30 \cdot 10^{-3}$ |
| 1-2 | | 3.03 | 36.5 | 45.2 | 0.29 |
| 1-3 | $8.4 \cdot 10^2$ | 1.39 | 5.2 | 4.1 | 0.52 |
| 1-4 | | 3.03 | 16.1 | 9.6 | 1.4 |
| 1-5 | $3.7 \cdot 10^2$ | 1.39 | 2.3 | 1.5 | 1.5 |
| 1-6 | | 3.03 | 7.0 | 4.6 | 3.2 |
| 1-7 | $1.72 \cdot 10^2$ | 1.39 | 1.06 | 0.89 | 3.8 |
| 1-8 | | 3.03 | 3.3 | 2.2 | 6.7 |

Fig. 3.4 Oscillograms of pressure changes

at its equilibrium pressure. The actual pressure-time trace, however, will show some pressure vibration due to the inertia effect of gas, which will serve for $p_2$ to exceed over $p_{max}$ or to accelerate the pressure more rapidly toward $p_{max}$ than without it.

2) Experimental approach by simulation tank

In order to realize the foregoing idealized system of the combustion chamber arrangement for observation of the pressure rise in such a process, an air simulation tank was employed. Its total arrangement is shown in Fig. 3.2 and the full sketch of the main chamber with its entrance in Fig. 3.3. The sudden pressure rise in the auxiliary chamber and the air flowing into the main chamber are simulated by a break-off of the cellophane diaphragm which initially endures the pressure difference of two chambers. The diaphragm is pierced through a needle triggered electrically by an external signal. The volume of the auxiliary chamber is so large as compared with the main chamber that the assumption that the pressure in the auxiliary chamber holds constant after the step-functional jump, may be realized. For this reason, the volumes of the auxiliary chamber and the main chamber were chosen as 1570 $cm^3$ and 57.8 $cm^3$ respectively. Pressure pickups used were of strain gage type designed as cylinder pressure indicator (nominal value of natural frequency is above 35 kc/sec), and their recording was made on a dual beam cathode ray oscillograph.

Fig. 3.4 shows examples of pressure records obtained by various area ratios of K under the definite pressure ratios of $p_{max}/p_c$=1.39 and 3.03. In Fig. 3.5 the experimental pressure-time traces are shown together with the theoretical curves yielded from the integration of Eq. (3.4), for the serial cases of $p_{max}/p_c$=1.39. Numerical values for this computation were as follows:

$\kappa$=1.40, $\mu$=0.65, $p_{max}/p_c$=1.39,

$a_1=a_c$=340 m/sec (15°C)

The theoretical curves drawn in the figure virtually coincide with the experimental ones, especially in the earlier stages of pressure rise, although the theoretical ones were obtained on the assumption of a quasi-static process. Therefore, it may be probable that the departure from the quasi-static process is so small except in the later stages of pressure rise that effects of gas inertia in the system are negligible as compared with the throttle effect of the connecting passage. In the later

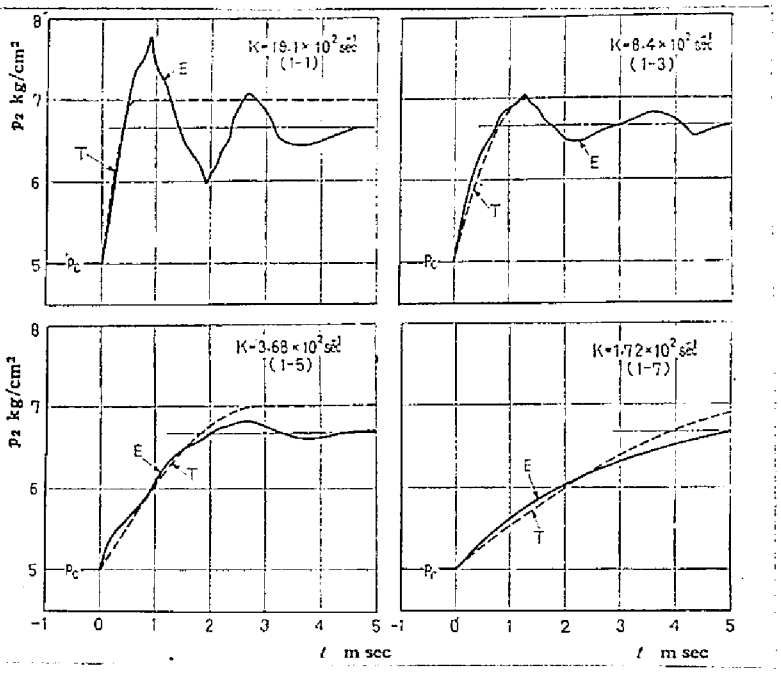


Fig. 3.5 Measured pressure changes at $p_{max}/p_c = 1.39$, together with theoretical changes (T)

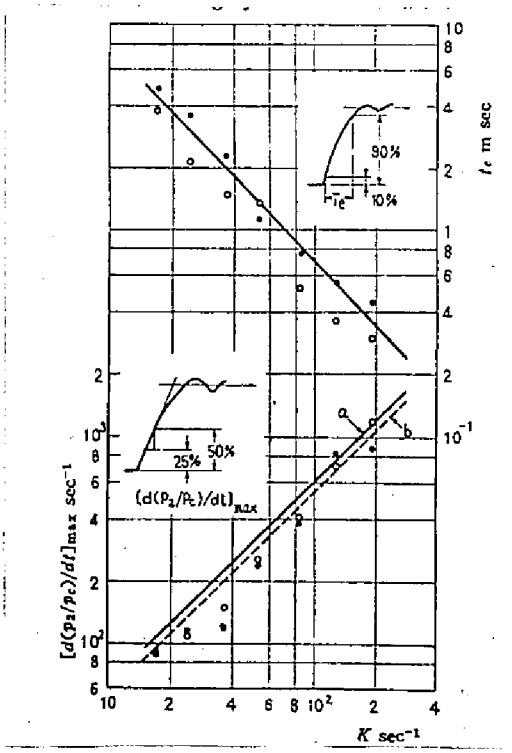


$p_{max}/p_c = 1.39$, o: passage length $l = 5$ mm, ●: $l = 10$ mm, a and b are theoretical values at the beginning of pressure rise and at its 38 % respectively.

Fig. 3.6 Effect of K on pressure rate $d(p_2/p_c)/dt$ and on rising time $t_e$

stages of pressure rise, however, a remarkable gas oscillation is observed with a large value of K. This may be due to the inertia effect of gas.

In the actual engine, the knock intensity and the criterion of whether it is knocking or not are predominantly governed by the maximum rate of pressure rise or by the maximum pressure and the rising time of pressure rise due to combustion, as stated in CHAPTER 1. For this reason, the availability of Eq. (3.7), in which inertia of gas has been neglected, for the pressure rising rate obtained experimentally with the simulation tank, was examined. In order to avoid the complexity of the pressure rise at its very beginning, as has been seen in the oscillograms, an average rate from 25% to 50% of pressure rise was conveniently adopted as the rate of pressure rise to be compared with. The measured rate was plotted in Fig. 3.6 by $d(p_2/p_c)dt$ $sec^{-1}$, as the function of K. In the same figure are shown the corresponding theoretical lines: One is the line calculated by Eq. (3.7) and the other is the value of pressure rise at 38% which corresponds to the middle pressure at 25% and 50%. In the upper half of the figure are shown the plots and theoretical line, of the rising time $t_e$, defined as the duration of pressure rise at 10% to 90%. This figure indicates that the average rate of pressure rise and rising time virtually coincide with their theoretical values of a relatively wide range of K. Consequently, the validity of the equation with the inertia effect neglected seems proved when applied to the practical system containing such a transient process.

By the way, in Fig. 3.6 the effect of the length of the connecting passage $\ell$ is shown as the plots of dark circular mark. It can be seen that there is almost no influence given on the rate of pressure rise but that a slight change is observed in the rising time $t_e$ for different lengths.

Concerning the vibrations at the end of pressure rise, the pressure was measured at different positions in the test tank, and was compared with that at the original measuring position. Fig. 3.7 (a) shows a simultaneous record of pressure in the case of $K=19.1\times10^{-2}sec^{-1}$: One is of the original position and the other is of the different position in the same chamber as indicated as Loc. 2 in the figure. No great phase difference can be seen for the fundamental component of vibration, although higher frequency components do not show any remarkable general rule. Fig. 3.7 (b) shows comparison between pressure at the original measuring position and that at a different position in the auxiliary chamber indicated as Loc.3. It can be seen from it that two principal frequencies are not identical with each

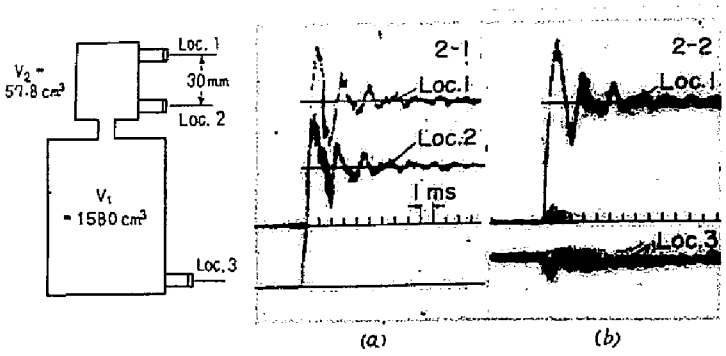


Fig. 3.7 Pressure changes at various locations of pick-up, in comparison with those of original location

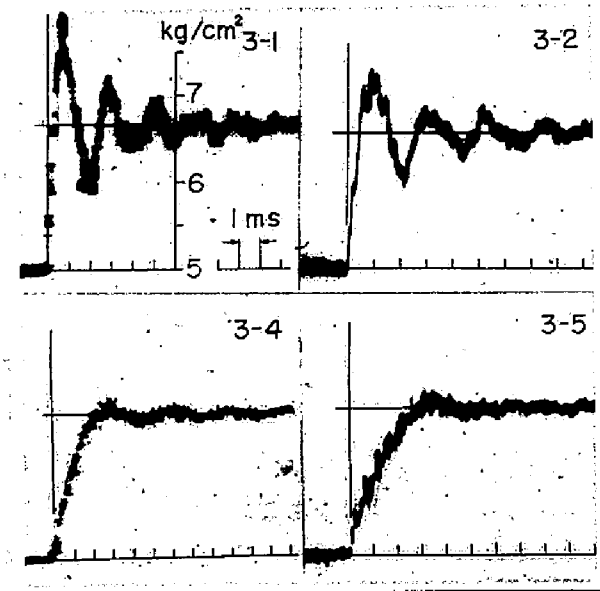


| No. | K $sec^{-1}$ | $\ell$ mm | $d(p_2/p_c)/dt$ $sec^{-1}$ | $t_e$ sec | Angular frequency rad/sec |
|---|---|---|---|---|---|
| 3-1 | $19.1 \cdot 10^3$ | 5 | $11.8 \cdot 10^3$ | $0.30 \cdot 10^{-3}$ | $3.0\ 10^3$ |
| 3-2 | | 10 | 8.7 | 0.45 | 2.8 |
| 3-3 | $3.7 \cdot 10^3$ | 5 | 1.45 | 1.46 | 2.0 |
| 3-4 | | 10 | 1.20 | 2.32 | 1.8 |

Fig. 3.8 Influence of length of connecting passage on pressure change

other. Therefore, it is ascertained that the pressure vibration is not of the category of resonance of the whole gas system. Judging from these experiments, the vibration system may be considered as a sort of Helmholz' resonator consisting of the space $V_2$ and the connecting passage. From other experiments with different passage lengths $\ell$ as summarized in Fig. 3.8, we can notice that a longer passage generally has a lower frequency.

## 3.3 Dynamic Process in Cylinder Simulated by a Thin Water Sheet

In the previous Section, little attention was paid to the dynamic aspect of the matter, that is, the pressure wave propagation produced in the combustion chamber by such an unsteady flow phenomenon which is completed within a very short duration, assuming it as a quasi-static process. In order to estimate more accurate course of pressure in the actual combustion chamber, the engine cylinder was simulated by a two-dimensional unsteady water analogue tank.

An analogy between pressure waves in compressible gas and gravity waves on the free surface of a liquid has long been known. By a proper selection of state parameters, analogous relationships are derived about pressure and specific volume in gaseous system. This technique has a wide applicability in analyses of complicated flow phenomena; e.g. simulations of a two-dimensional supersonic steady flow, of development of gaseous detonation in a unidimensional flow field[18], and of sound waves in a room. Because the wave speeds are low, the hydraulic analogue is especially convenient for the study of unsteady flows as occur in the inlet and exhaust ducts of reciprocating machinary[19][20]. As the theory and practice of the simulation technique of a two-dimensional unsteady flow were recently developed and achieved by Dinkelacker[21], the present study on the pressure propagation phenomenon in the combustion chamber of diesel engine is made on his work.

### 1) Basis of the analogy

A free surface liquid flow is firstly taken up. Ignoring vertical components of velocity and acceleration, the pressure will vary in the vertical direction according to the hydrostatic law, and thus the resultant velocity will be constant on vertical lines. Taking the bottom of

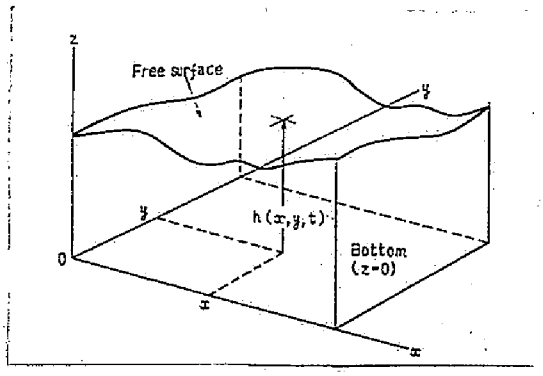


Fig. 3.9

the channel to be in the x, y-plane, as shown in Fig. 3.9, whose non-dimensional representation is X,Y-plane, and using h so as to denote the depth of water, where the non-dimensional form is H, the governing equations are as follows:

$$\left.\begin{aligned} &\frac{\partial H}{\partial \tau}+\frac{\partial (HU)}{\partial X}+\frac{\partial (HV)}{\partial Y}=0 && \text{(Equation of continuity)}\\ &\frac{\partial U}{\partial \tau}+U\frac{\partial U}{\partial X}+V\frac{\partial U}{\partial Y}=-\frac{\partial H}{\partial X},\cdots && \text{(Momentum equation)} \end{aligned}\right\} \quad (3.8)$$

where $\tau$ is the non-dimensional time of t. All non-dimensional variables are represented by reference length, depth, time and velocity $\ell_0$, $h_0$, $t_0$ and $a_0$ respectively. The last one is the propagation speed of an infinitely small amplitude wave. The non-dimensional numbers are then expressed as follows:

$$X=x/\ell_0,\quad Y=y/\ell_0,\quad H=h/h_0,\quad U=u/a_0,\quad V=v/a_0,\quad \tau=t/t_0 .$$

Consequently, the following relationships must hold in the reference time: $t_0=\ell_0/a_0$.

If the corresponding state parameters for the two-dimensional gaseous flow are distinguished from parameters for a free surface liquid flow by putting the asterisk*, then the governing equations can be given as follows:

$$\left.\begin{aligned} &\frac{\partial P^*}{\partial \tau^*}+\frac{\partial (P^*U^*)}{\partial X^*}+\frac{\partial (P^*V^*)}{\partial Y}=0\\ &\frac{\partial U^*}{\partial \tau^*}+U^*\frac{\partial U^*}{\partial X^*}+V^*\frac{\partial U^*}{\partial Y^*}=-\frac{1}{P^*}\frac{\partial \Pi^*}{\partial X^*}\frac{p_0^*/\rho_0^*}{a_0^{*2}},\cdots \end{aligned}\right\} \quad (3.9)$$

where $\rho_0^*$ and $p_0^*$ are reference density and pressure respectively. P* and $\Pi^*$ are non-dimensional density and pressure defined as follows:

$$X^*=x^*/\ell_0^*,\quad Y^*=y^*/\ell_0^*,\quad U^*=u^*/a_0^*,\quad V^*=v^*/a_0^*$$
$$P^*=\rho^*/\rho_0^*,\quad \Pi^*=p^*/p_0^*,\quad \tau^*=t^*/t_0^*,$$

where there is a similar relationship of $t_0^*=\ell_0^*/a_0^*$.

It may be noted from comparison between Eqs. (3.8) and (3.9) that the equations for gas motion are formally similar to those for the free surface liquid motion, hence the following correspondence providing the analogous relationships: namely.

$$H=P^*,\quad U=U^*,\quad V=V^*,\quad X=X^*,\quad Y=Y^*$$

If the adiabatic law of specific heats $k^*$ holds good in the gas, then we

have

$$\Pi^* = P^{*\kappa^*} , \quad \rho_o^* a_o^{*2} = \kappa^* p_o^* \tag{3.10}$$

By using these relations we can rearrange the right hand side of the second formula of Eq. (3.9) as follows:

$$-\frac{1}{P^*}\frac{d\Pi^*}{dP^*}\cdot\frac{\partial P^*}{\partial X^*}\cdot\frac{p_o^*/\rho_o^*}{a_o^{*2}} = -(P^*)^{\kappa^*-2}\cdot\frac{\partial P^*}{\partial X^*} \tag{3.11}$$

Therefore, $\kappa^*=2$ is necessary to satisfy the similarity of this to the term of right hand side of the momentum equation in Eq. (3.8). In other words, the relations of isentropic gas dynamics are to be applied to the hydraulic analogue by setting $\kappa^*=2$. Hence, the density ratio P* is equivalent to the depth ratio of model H and the pressure ratio $\Pi^*$ to $H^2$.

In the water channel experiments the selection of reference depth of model $h_o$ must be of importance. In the free surface water flow the propagation speed of infinitesimal amplitude disturbance is generally a function of the wavelength because of surface tension, while the sound velocity $a^*$ in the still gas does not depend on the wavelength. The calculation results of the relation between propagation speed and wavelength indicate that capillary waves behave most like gravity waves for depths of about 3 to 4 mm[21]. In a practical sense, however, a larger reference depth is more favorable than the optimum for the conveniences of depth measurement and of escaping from the effect of friction produced at the bottom, thus the reference depth being made as large as about 14 mm in the present experiment.

One of the benefits of the simulation is time magnification of the exceedingly fast phenomena occurring in the engine. Considering the engine having a bore of 95 mm in diameter, which has been employed in the previous chapters as an example, the sound velocity at the end of compression reaches 550 m/sec. If we select 14.2 mm as the water depth $h_c$ at the end of compression for simulation, the propagation speed $a_c$ is

$$a_c = \sqrt{gh_o} = 0.373 \text{ m/sec} \tag{3.12}$$

Cylinder bore D being occasionally made 190 mm in the model, thus the unit of time $t_o = D/a_c$ is 0.51 sec. In contrast, $t_o^* = 0.173\times10^{-3}$ sec being estimated for the actual gaseous system, the time magnification factor $t_o/t_o^*$ is of the order of 3000 in the present case.

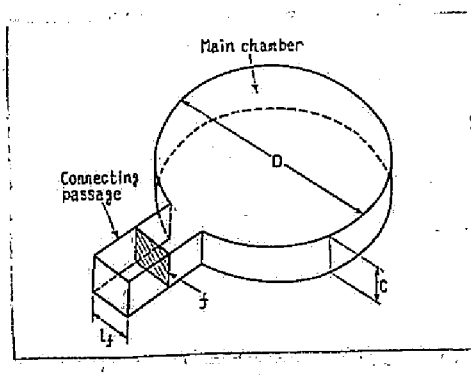


Fig. 3.10

In the main combustion chamber of the divided chamber type, combustion chamber having a connecting passage of the cross-sectional area f, the maximum rate of pressure rise due to the quasi-static inflow of gas into the main combustion chamber was induced on the assumption that there happens a step-functional pressure jump in the auxiliary combustion chamber. Its non-dimensional rate $r_2$ is, according to Eq. (3.7) in the previous section,

$$r_2 = \frac{d(p_2/p_c)}{d(t/t_0)} = \sqrt{2\kappa}K_0 \left(\frac{p_{max}}{p_c}\right)^{(3\kappa-1)/2\kappa} \times \sqrt{\frac{\kappa}{\kappa-1}\left\{\left(\frac{p_c}{p_{max}}\right)^{2/\kappa} - \left(\frac{p_c}{p_{max}}\right)^{(\kappa+1)/\kappa}\right\}} \tag{3.13}$$

where $t_0$ and $K_0$ are the unit time and the non-dimensional cross-sectional area of connecting passge respectively. They are expressed as follows:

$$\left.\begin{aligned} t_0 &= D/a_c \\ K_0 &= \mu f D/V_2 \end{aligned}\right\} \tag{3.14}$$

where, D: diameter of bore, $a_c$: sound velocity at the end of compression, $\kappa$: ratio of specific heats, $\mu$: flow coefficient of the connecting passage. As being rigorous without the inertia effect of gas, Eq. (3.13) may be considered to be an asymptotical formula for the small value of $K_0$.

In arriving at the analogy, we assume that the water flow is two-dimensional. Consequently, this would call for a special consideration in representation of $K_0 = \mu f D/V_2$ on the water model in the two-dimensional sense. Fig. 3.10 illustrates the concept in which a fictitious combustion chamber of constant thickness c is presented. The connecting passage of area f is then reduced to a rectangular of c in height and $l_f$ in breadth, namely,

$$f = l_f \cdot c$$

In the same manner, the volume of main combustion chamber $V_2$ is

$$V_2 = F \cdot c = \pi/4 \cdot D^2 c.$$

According to these relations, $K_0$ may be rearranged as follows:

$$K_0 = \frac{\mu f D}{V_2} = \frac{\mu l_f \cdot cD}{\pi/4 \cdot D^2 c} = \frac{4\mu}{\pi} \cdot \frac{l_f}{D} \tag{3.15}$$

The ratio of specific heats being $\kappa = 2$ in the water model, Eq. (3.13) is finally reduced to be

$$r_2 = 2K_0 \pi_{max}^{3/4} \sqrt{2\left(\pi_{max}^{-1} - \pi_{max}^{-3/2}\right)} \tag{3.16}$$

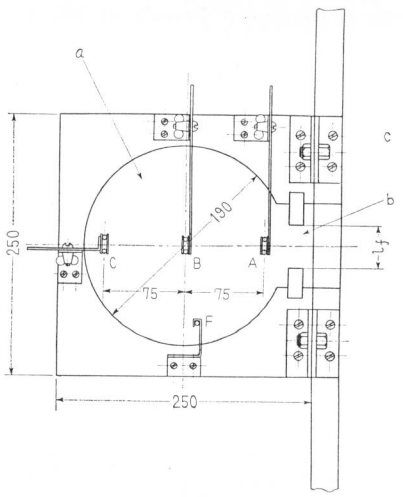


a: tank analogous to main chamber
b: connecting passage
c: tank analogous to auxiliary chamber
A,B and C: probes for sensing the water depth
F: calibrator for setting initial water depth

Fig. 3.11 Details of water simulation tank

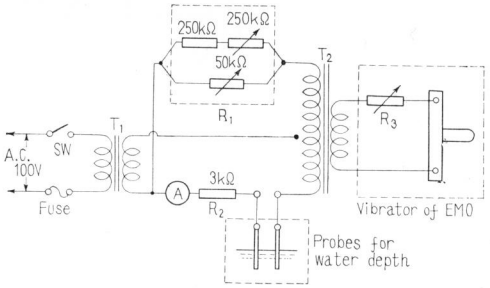


Fig. 3.12 Circuit for measuring water depth

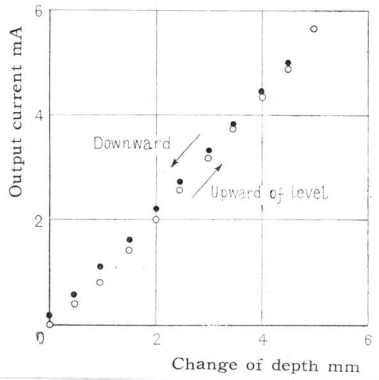


Fig. 3.13 Output current against water depth by static calibration

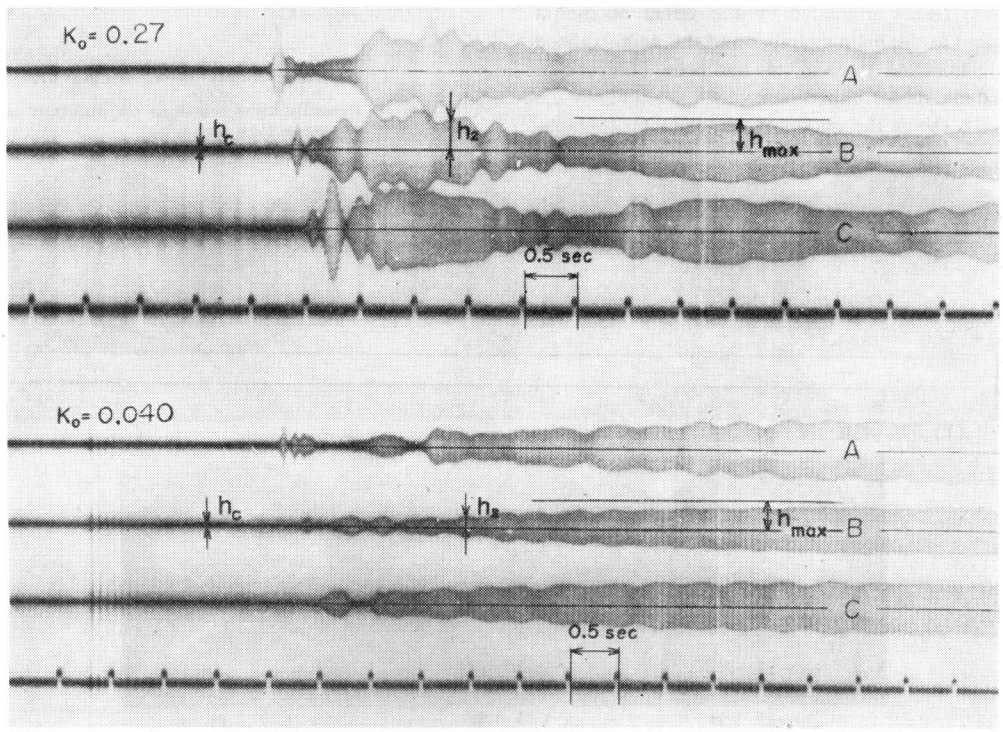


Fig. 3.14 Records of depth-time relations at different measuring positions of A, B and C

where

$$p_{max}/p_c = \pi_{max} .$$

2) Experimental results and considerations

Experimental apparatus

The water channel analogue is illustrated in Fig. 3.11, showing the top view of the apparatus, where a is the tank equivalent to the main chamber of the divided chamber type combustion chamber and b to the connecting passage. The part c corresponds to the auxiliary chamber with which such a condition is almost satisfied that a step-functional pressure jump may happen in the auxiliary combustion chamber and the pressure may be held constant after the jump. Therefore, the surface area of the auxiliary chamber is made to be about ten times the piston area to be simulated, and its depth at the beginning to be ten times the reference depth in the main chamber so that it is possible to recover the height of water near the connecting passage as fast as possible by multiplying the propagation speed in the auxiliary chamber by several times.

The water depth is measured from the electric resistance of water through 0.3 mm-diameter stainless electrodes steeped in the liquid at a distance of 10 mm in parallel. Thus the resistance which varies according to the water level is coupled with solid resistors, composing a kind of electric bridge, and an alternative current of 60 c/sec is supplied on it. As is seen in the circuit diagram of Fig. 3.12 impedance matching is made to an electromagnetic vibrator of an oscillograph, by falling down the output fraction of about 1/50 the primary voltage through a differential type transformer. The measured current versus actual change of depth is shown in Fig. 3.13 showing a relatively excellent linearity. However, the curve shows a hysterisis due to effect of meniscus formation around the electrodes so that the error amounts to as high as 0.3 mm in water level if the level is put back again to the starting position. This error seems inevitable as far as the electrodes of finite diameter are used. Three couples of electrodes are located in the positions indicated as A, B and C in Fig. 3.11 and the one in the auxiliary chamber tank. Fig. 3.14 is an example of oscillograms taken with those installations. It is noted that the envelope on the 60 c/sec-carrier waves indicates a deviation of water depth from the reference in each measur-

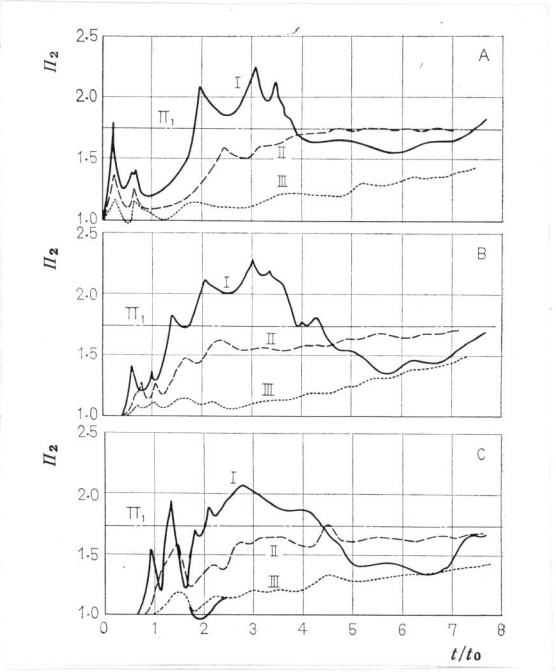


I: $K_o$= 0.27, II: $K_o$= 0.107, III: $K_o$= 0.040

Fig. 3.15 Pressure-time relations for different areas of connecting passage

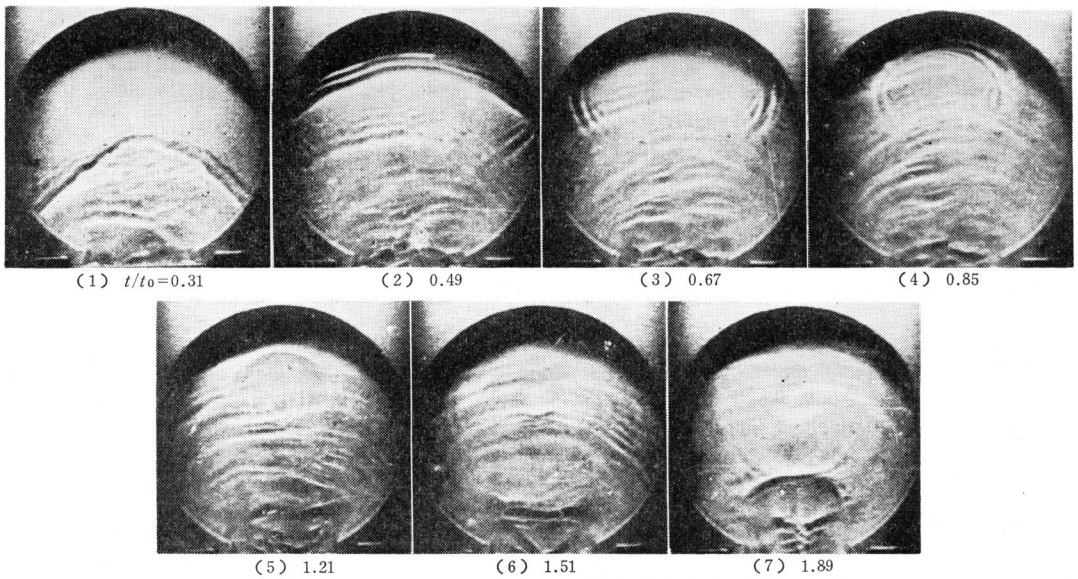

(1) $t/t_0$=0.31 (2) 0.49 (3) 0.67 (4) 0.85

(5) 1.21 (6) 1.51 (7) 1.89

Fig. 3.16 Snapshots of water propagation at $K_o$= 0.27

ing position.

Experimental results and considerations

The water analogue was applied to such a transient process as the gas in the auxiliary chamber suddenly streaming out into the main chamber owing to a combustion taking place in the auxiliary chamber. In Fig. 3.15 the pressure-time traces reproduced from the oscillograms are shown for each measuring position. They are derived at constant pressure ratio, $\Pi_{max}=p_{max}/p_c$ being 1.73, for three different ratios of connecting passage, namely, $K_o$=0.27, 0.107 and 0.040.

The abscissa of the diagram is the non-dimensional time, that is, the ratio of actual time to the unit time of $t_o=D/a_c$. The pressure is obtained from the square of water depth and is presented in the ratio to the initial pressure. It can be seen from the figure that there is a considerable distortion of pressure concerning the measuring position, especially in the very beginning of the influx of gas from the auxiliary chamber: A sharp pressure pulse is formed near the connecting passage and spreads and concentrates in the main chamber. It is deformed later by the reflection of waves from the boundary.

Wave height of this pulse is generally low at the spot B, that is, the center of the chamber. On the contrary, the water level rises at the spot C due to the convergence of reflected waves, and, with $K_o$=0.27, it exceeds the equilibrium pressure ratio only through the accumulation of such reflected waves. After successive influxes, the pressure overshoots the equilibrium, causing an oscillation of relatively low pitch. This oscillation is remarkable when $K_o$ is large. Owing to this, the pressure ratio at each measuring position exceeds the unity between 1.5 and 4.0 of $t/t_o$, with $K_o$=0.27. This low pitch oscillation originates from the effect of inertia distributed in the main chamber and the neighborhood of the connecting passage, as has been observed in the air-tank model experiment.

Fig. 3.16 shows the successively taken photographs of wave propagation, with $K_o$=0.27. Film (1) corresponds to the earliest stage of an influx showing an arc-shaped wavefront of discontinuity. It rolls fast in the field of the main chamber [Film (2)] and reflected waves are concentrated near the spot C [Film (3) and (4)]. After fully developed [Film (5)], the waves spread producing a negative pressure region. At the inlet, a new wavefront is formed which assists the further inflow of fluid into the main chamber [Film (6) and (7)].

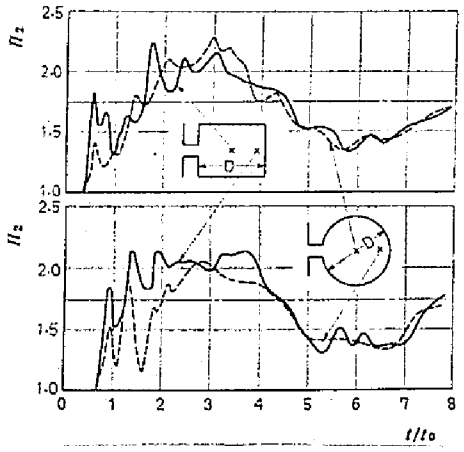


$K_0$ corresponds to 0.27

Fig. 3.17 Pressure-time relations in a rectangular tank, in contrast to the cylindrical tank

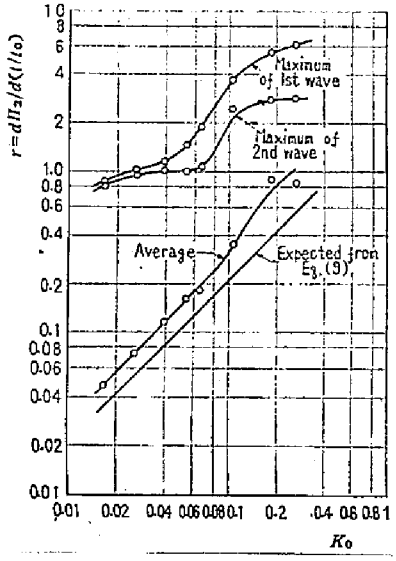


Fig. 3.18 Effect of $K_0$ on non-dimensional rates of pressure rise at spot B

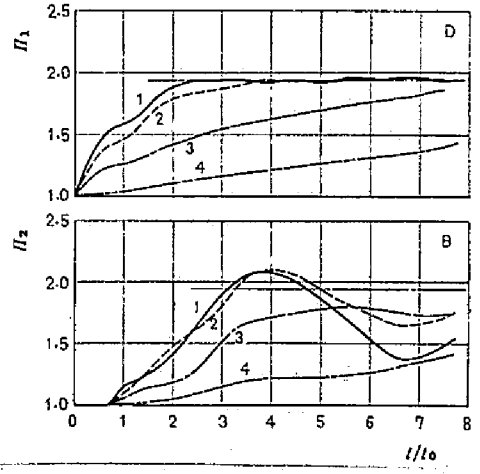


Fig. 3.19 Pressure-time relations for various inputs of pressure in the auxiliary chamber for $K_0 = 0.27$

As shown above, in the cylindrical water-tank, the wave reflected by the wall plays an important role in the development of a pressure rise in the main chamber. In order to clarify the effect of this wall reflection, another test was made with a rectangular tank. Its size was chosen so that its surface area might be equal to that of the cylindrical tank and the distance between the inlet and the opposite side of boundary might be equal to the cylinder diameter. In Fig. 3.17 a pressure-time trace achieved with the rectangular tank is shown together with that of cylindrical tank, where the connecting passage is of $K_0$=0.27 for both cases. It is seen that the pressure changes more sharply with the rectangular tank than with the cylindrical tank, especially at the beginning. Waves in the rectangular tank propagate somewhat one-dimensionally across the chamber, so that the degree of wave attenuation due to the reflection and interaction is less than that of the cylindrical tank. On account of this, a relatively sharp pressure rise will occur with the rectangular tank.

Fig. 3.18 shows maximum and average rates of pressure rise, measured at the spot B, that is, the center of the cylindrical tank. They are given as functions of $K_0$ in the form of $d\Pi_2/d(t/t_*)$. Maximum rate of first pressure impact is always largest in the total course of pressure rise, and the rate of second impact comes after it. In them, the average rate is the tangent of pressure rise, fine waves in it being ignored, and the line drawn in the figure denoting the theoretical value calculated from Eq. (3.16) in which inertia effect is ignored. The figure shows that the average rate is nearly proportional to the theoretical in the entire range of $K_0$, but that the maximum rates of early pressure rise are exceedingly large compared with the theoretical. Steep acclivities are seen in both maximum rates, in the range of $K_0$ between 0.06 and 0.10, and these rates will approach certain definite values at the extremes of the large $K_0$ as well as of the small one.

Finally, the effect of the course of pressure in the auxiliary chamber on the pressure response in the main chamber was studied by fitting up the test tank with a device for realizing a variety of water depth-time relations: The water level was initially set up by amassing in a bell-shaped tank that was immersed in a liquid at the auxiliary chamber tank, and, by keeping its cock open to the atmosphere, various speeds of water level were materialized in the test tank. The test results for $K_0$=0.27 are shown in Fig. 3.19, contrasting the pressure-time traces

measured at the spot B with those in the auxiliary chamber, namely the input waveform $\pi_1$. All curves gained by a gently sloping input are smoother than the curve gained by the step-functional input as has already been seen in Fig. 3.15, and no sharp pulse is seen at the beginning of influx of fluid with those curves. In the response waveforms of 1 and 2, there occurs the same kind of low pitch oscillation of pressure as experienced with the step-functional input. Its amplitude will diminish with a decrease of the slope of input waveform. Lastly, as regards the rising rate, a rapidly ascending step is observed in the pressure of the main chamber of 3, the maximum rate of which reaches a far larger value than that seen in the corresponding input curve, being as high as those of responses 1 and 2.

Summarizing the above, the hydraulic analogy to a two-dimensional unsteady gas flow is a suitable mean in shedding light on the qualitative aspects of pressure wave propagation in the combustion chamber. Some important revelations of the study are as follows: When pressure in the auxiliary chamber changes step-functionally, a sharp pressure pulse spreads in the main chamber, followed by a rapid pressure rise and a pressure vibration of relatively low pitch. Such pulse and vibration decline with the decrease in the cross-sectional area of the passage and with smoothing the pressure change in the auxiliary chamber.

## 3.4 Pressure Rate in the Actual Engine

As shown above, the maximum rate of pressure rise in the main chamber is, owing to the pressure pulse, exceedingly higher than the theoretical value predicted on the assumption of quasi-static process. As has been observed on the last experiment of the water model, however, this pulse disappears as soon as the pressure change in the auxiliary chamber is slowed down by a little. Since the pressure course in the actual engine is far from a step-function, the pressure rate in the main chamber predicted by Eq. (3.7) will give a value not distant from the practical. On the other hand, according to CHAPTER 1, the intensity and existence of knock in the actual motor may be roughly expressed by the rate of pressure rise on crank-angle basis: 3 $kg/cm^2/deg$ may be a limit of audible knocking while 5- to 6 $kg/cm^2/deg$ gives intense knocking, and 4 $kg/cm^2/deg$ may be considered to be an allowable limit for knock intensity. These knowledges will give an area ratio of connecting passage with which the pressure rise

is not influenced by the sharpness of the pressure rise in the auxiliary chamber.

If $p_c$ and $a_c$ denote the pressure and sound velocity at the end of compression as the reference state and if it is assumed that gas which flows out of the auxiliary chamber just after the pressure jump is simply of the adiabatic compression from the initial state of $p_c$ and $a_c$, although the actual change will be far from this owing to high temperature product due to combustion, then the following relationship holds between $p_1$ and $a_1$:

$$\frac{a_1}{a_c} = \left(\frac{p_1}{p_c}\right)^{(k-1)/2k}$$

Transforming time variable t sec to crank angle $\theta$ deg by using the relation $d\theta = 6ndt$, where n is the engine speed in rpm, we obtain the following maximum rate of pressure rise on crank-angle basis:

$$\left(\frac{dp_2}{d\theta}\right)_{max} = \frac{\sqrt{2k}K_0}{6Dn} p_c a_c \left(\frac{p_{max}}{p_c}\right)^{(3k-1)/2k} \times \sqrt{\frac{k}{k-1}\left\{\left(\frac{p_c}{p_{max}}\right)^{2/k} - \left(\frac{p_c}{p_{max}}\right)^{(k+1)/k}\right\}} \qquad (3.17)$$

In this formula, $K_0$ may be represented by the design parameters of engine and of its combustion chamber; namely,

$$K_0 = \frac{\mu f D}{V_2} = \mu(\varepsilon - 1)\left(\frac{f}{F}\right)\left(\frac{D}{S}\right)\left(\frac{V_c}{V_2}\right) \qquad (3.18)$$

where, $\varepsilon$: compression ratio, F: area of piston surface, S: stroke, $V_c$: clearance volume, $V_2/V_c$: volume ratio of main chamber to total compression volume. It can be seen from Eq. (3.17) that the same $K_0/Dn$ gives the same rate of pressure rise if $p_{max}/p_c$ is constant.

These relations are applied to a high speed engine with typical combustion chambers arranged. Specifications of the engine to be illustrated are as follows:

Stroke S and bore D: 115 mm and 95 mm respectively

Nominal speed: 1400 rpm

$p_c$, $p_{max}$ and $a_c$ have been estimated from indicator diagrams, as follows:

$p_c$=35 kg/cm$^2$, $p_{max}$=50 kg/cm$^2$, $a_c$=550 m/sec.

Combustion chambers are of pre-chamber type and of swirl chamber type as follows:

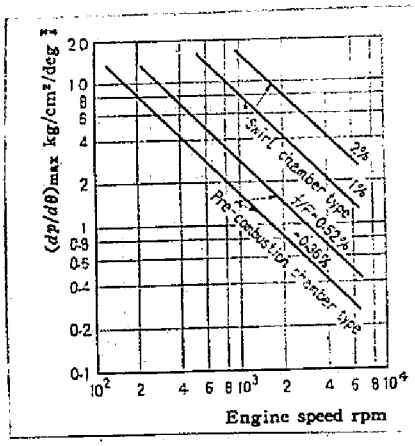


Fig. 3.20 Maximum rate of pressure rise estimated in the actual motor

| | Pre-chamber type | Swirl chamber type |
|---|---|---|
| f/F | 0.52% | 2.0% |
| $V_2/V_c$ | 67% | 37% |
| $\varepsilon$ | 19 | 16 |
| $K_o$ | 0.075 | 0.436 |

where $\kappa$ =1.40, $p_{max}/p_c$=1.50 and $\mu$=0.65

Fig. 3.20 shows the maximum rate of pressure rise calculated from Eq. (3.17) by using the numerals presented above. A chain line drawn in the figure indicates the upper limit of knock-free running condition, corresponding to 4 kg/cm$^2$/deg. With the pre-chamber type, the estimated rate of pressure rise exceeds the limit of below 700 rpm for f/F =0.52% and, for 2% of f/F with the swirl chamber type, it falls below the limit at higher than 4000 rpm. By considering that the nominal engine speed is 1400 rpm, it may be predicted that for the pre-chamber type engine the sharp pressure rise in the auxiliary chamber is not transmitted to the main chamber because of its relatively small cross-sectional area, thus leading to a knock-free condition in the regular speed range.

On the other hand, the swirl chamber type combustion chamber has generally a larger area ratio of connecting passage and has a smaller volume of the main chamber for the sake of such a design concept that the greater portion of fuel may be completely burned in the swirl chamber. Therefore, the value $K_o$ of the swirl chamber type usually reaches from three to ten times the value of the pre-combustion chamber type, so that the swirl chamber type engine does not fulfil the knock-free condition even if it runs at the maximum speed as has been seen in the illustration presented above.

Since the greater part of fuel can burn in the auxiliary chamber in the idling run of the pre-chamber type engine, the assumption presented earlier may actually be almost materialized. It should be borne in mind that the idling knock phenomenon of this type engine, which prevails with the decrease of engine speed, corresponds to the fact that the maximum rate of pressure rise $(dp/d\theta)_{max}$ augments with the decrease of engine speed. However, this is still an unsatisfactory explanation for the idling knock if considerable amount of unburned fuel has been brought into the main chamber to autoignite in it [17].

## 3.5 Conclusion

The present investigation on the effect of the connecting passage area on the course of pressure in the main combustion chamber has led to the following results:

(1) Under an ideal condition where there happens a pressure jump in the auxiliary combustion chamber and there is no heat release in the main chamber, the maximum rate of pressure rise in the main chamber is proportional to the area ratio of the passage and inversely proportional to the volume ratio of the chamber, if the gas flows quasi-statically into the main chamber.

(2) When pressure in the auxiliary chamber changes step-functionally, a sharp pressure pulse spreads in the main chamber, followed by a rapid pressure rise and a pressure oscillation. Such a pulse declines with narrowing the connecting passage and with smoothing the pressure change in the auxiliary chamber.

(3) Application of these results to the engine shows that, with the pre-chamber type engine, a rapid combustion in the auxiliary chamber is not transmitted to the main chamber because of the throttle effect of the connecting passage, resulting in a smooth pressure in the main chamber. On the contrary, it will be with the swirl chamber type.

CHAPTER 4

# Combustion and Knock in the Swirl Chamber Type Diesel Engines

## 4.1 Outline of the Problem

The development goal of the combustion research on diesel engine is to obtain a combustion system in which fuel introduced can burn completely near the top dead center with a low combustion noise throughout the entire range of running. The swirl chamber type engine is considered to be one of realizations on this line. Much has been known hitherto on the characteristics of the engine, i.e. the performance and quietness: First of all, Ricardo made a foreseeing experiment on the effect of intensity of air swirl on the characteristics, using a sleeve-valve four-cycle engine, and revealed that its performance was remarkably improved by increasing the swirl intensity but an excessive vorticity would invite a rough firing with a knock occurring, accompanying a simultaneous drop in the quality of performance(1). On the other hand, the ecconomy and output of the engine is largely influenced by the direction of fuel spray relative to the air swirl. According to the investigation of Nagao and Kakimoto through an observation in high-speed motion pictures, the performance is not as good when the fuel spray is directed against the air swirl because the spray is apt to be concentrated in the central part of the combustion chamber, and a good performance is materialized when the fuel spray is concentrated in the peripheral area of the swirl chamber so that it may be trnasferred earlier into the main combustion chamber(22). Further, the effect of peripheral wall of the combustion chamber upon the combustion was investigated by Pischinger and Pischinger after tests on a constant-volume bomb under several conditions similar to those occurring in the actual motor(23). They have revealed that, if the wall is hot enough and if a sufficiently strong swirl is present, the injection along the wall causes a perfect combustion with a low rate of pressure rise in spite of poor interaction between fuel and air.

Much more information on the good combustion has been given than that enumerated above. In the present stage of investigation, however, prescriptions on improving performance seem more stressed than those on reducing the combustion noise. It does not seem that we have proper understandings on the phenomenon of knock occuring in the swirl chamber

type engine. In the present status each of the following problems has not been made clear:

(1) Essential roll of swirl on the velocity of burning,
(2) Influence of dimension of connecting passage on the velocity of pressure rise,
(3) Influence of combustion in the main combustion chamber,
(4) Influence of direction of spray,
(5) Influence of interaction between combustibles and wall,
(6) Influence of wall temperature,
(7) Influence of shape of combustion chamber, etc.

The aim of this study is to reveal these influences and their mechanisms. As the first step of it, problems (1) and (2) were tried to solve inclusively through changing the area ratio of the connecting passage. Details of it will be found in Section 4.2. In the course of this study the present author noticed the special importance of problem (3) concerning the burning in the main combustion chamber; the phenomenon of outflowing of unburned mixture from the swirl chamber to the main chamber was theoretically considered. This analysis is described in Section 4.3. A further investigation was made on problems (4) to (6) in the lump by observing combustion development through high-speed photography and indicator diagrams syncronized. Its detailed description will be seen in Section 4.5.

## 4.2 Relation between Pressure Rate and Dimension of the Connecting Passage

### 1) Pressure developments in the swirl chamber and the main chamber

As has been described in CHAPTER 3, a swirl chamber type diesel engine usually has a relatively large area of the connecting passage and a small volume of the main chamber, compared with the pre-chamber type engine. Owing to this, a rapid pressure rise in the swirl chamber, if it may happen, can propagate to the space of the main chamber with negligible decay of its sharpness. Consequently, an engine of this type will be noisy by nature even if no combustion takes place in the main chamber. It is then expected that the combustion noise is to be abated by either lowering the rate of pressure rise in the swirl chamber with some appropriate means, or narrowing the connecting passage with a view to removing the transmission of a

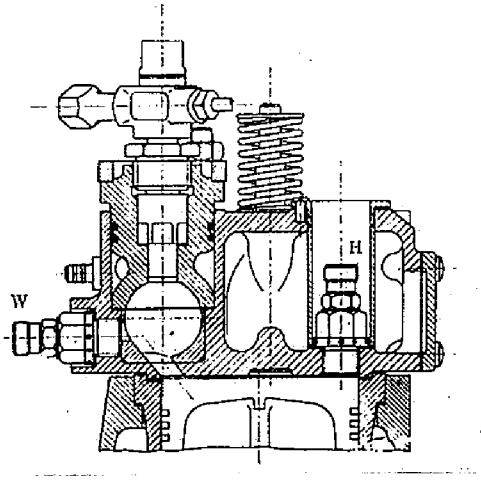


W: Indicator for the swirl chamber
H: Indicator for the main chamber

Fig. 4.1 Cross-sectional view of the combustion chamber

sharp pressure change or to releaving the influx of unburned fuel from a rapid explosion. However, a very small area of the connecting passage might result in an increase in the intensity of air-swirl thus changing the course of the mixture formation and the subsequent combustion. The flame photographs already presented[22] reveal that the fuel spray, when injected downstream of the swirl, rapidly reaches the connecting passage, hence quickening the outflow of a rich mixture into the main chamber, and that, when injected at the center of the chamber, fuel particles are accumulated in the middle part of the swirl chamber, thus causing a rapid pressure rise in the swirl chamber.

As seen from these observations, if the fuel spray is directed to the center of the combustion chamber, then the combustion will be such that a rapid pressure rise occurs in the swirl chamber and the amount of fuel, which takes part in the earlier stages of combustion in the main chamber, will be minimum. The present experiment was made under such a condition.

A water-cooled four-cycle single cylinder engine was used with a Ricardo Comet Mk. I type head arranged as shown in Fig. 4.1. The specifications of the engine are as follows: Cylinder diameter and stroke are 95 mm and 115 mm respectively, nominal output 7 PS at 1400 rpm, volume ratio of the swirl chamber to total compression space 65%, compression ratio 16.0, injection pump Bosch type PE1A70 B101, injection nozzle DN30S2 and fuel heavy oil "A" (specific weight 0.845, cetane number 45). Measurement was made with the area ratio of the connecting passage to piston surface f/F ranging from 0.53% to 2.2%.

Pressures in the swirl and the main chambers were detected by strain gage type pickups, whose diaphragms were placed flush with the combustion-chamber wall without any indicator passage arranged, as shown in Fig. 4.1, in order to obtain distortion-free diagrams of pressure-time relations. Their recordings were made on a dual beam cathode ray oscillograph by photographing images on it.

Indicator diagrams were taken with various engine speeds at a constant rack position of fuel controlling lever of the injection pump. The diagrams were analyzed in order to obtain the values of ignition delays, maximum rates of pressure rise and maximum pressures. There were considerable irregularities in each set of readings, so that the average values were obtained from two to five cards. The results were summarized in Fig. 4.2 and 4.3. In Fig. 4.3 are shown the maximum rates of pressure

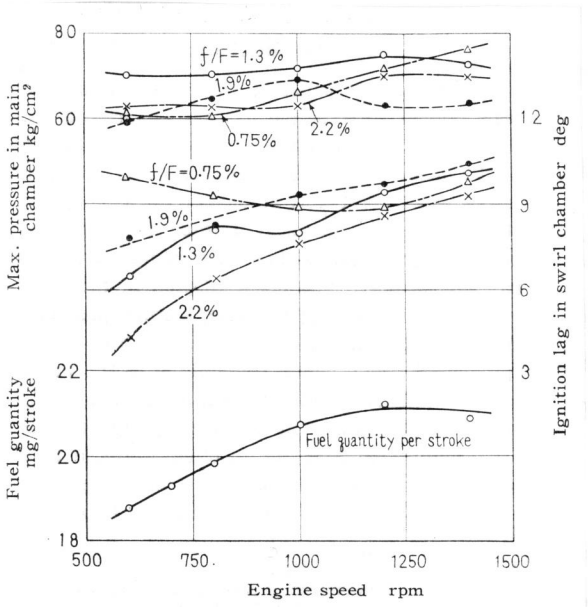


Injection timing: 14° before TDC

**Fig. 4.2 Effect of engine speed on ignition delay and maximum pressure for various area ratios of the connecting passage**

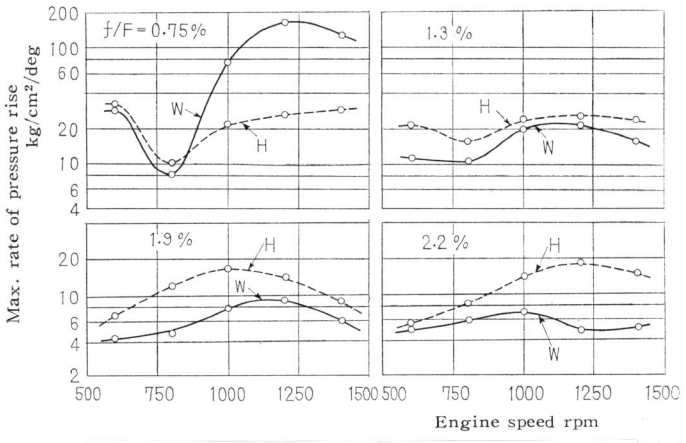


**Fig. 4.3 Effect of engine speed on the maximum rates of pressure rise in the swirl chamber (W) and the main chamber (H)**

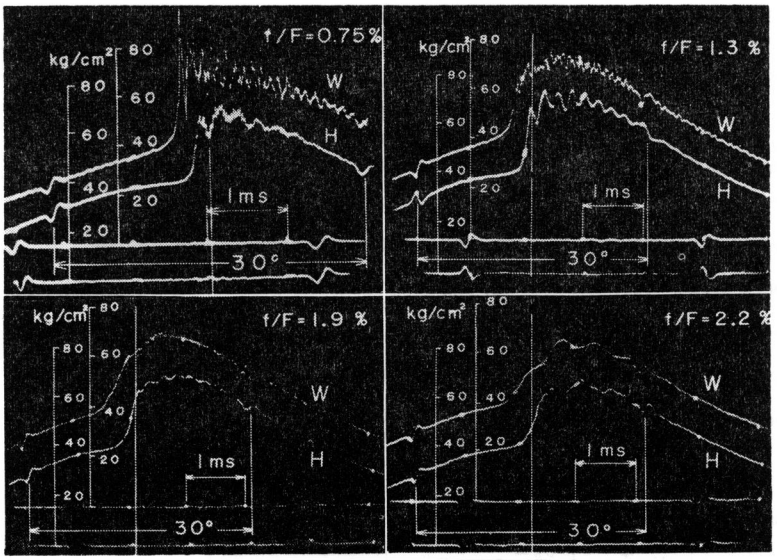


Engine speed: 1400 rpm,
Injection timing: 14° before TDC,
Timing mark: 1/1000 sec

Fig. 4.4 Example of indicator diagrams

rise in the swirl chamber (W) and those in the main chamber (H). Fig. 4.4 illustrates some typical indicator diagrams gained at 1400 rpm. From these the following facts are known:

(1) The maximum rate of pressure rise in the swirl chamber generally increases with the decrease in the area ratio of the passage.

(2) With f/F larger than 1.3% the rate of pressure rise in the main chamber is always larger than that in the swirl chamber, while, with 0.75% passage, the rate in the main chamber is lower than that in the swirl chamber in the range of engine speed above 1000 rpm.

(3) When f/F is 0.75%, the rates of pressure rise are lowest at 800 rpm, namely relatively less noisy. When it is 1.9% and 2.2%, the rate of pressure rise in each chamber will decrease as the speed is reduced.

Table 4.1 Predominant frequencies of pressure oscillation

| f/F % | Swirl chamber kc/sec | Main chamber kc/sec |
|---|---|---|
| 0.75 | 8.9 | 4.1 |
| 1.3 | 9.8 | 4.3 |
| 1.9 | 12.9 | 4.5 |
| 2.2 | 1.89 | 1.93 |

(4) It can be seen from indicator diagrams that the frequency and amplitude of pressure oscillation are largely influenced by the area ratio of the passage. Table 4.1 summarizes the measured values of principal frequencies of both chambers. At 2.2% of f/F, the frequency in the main chamber coincides with that in the swirl chamber whilst the phase of oscillation shifts by about 180°. Consequently, the total vibration system will approximately be a kind of Helmholz' resonator. When f/F is below 1.9%, the frequencies of the two chambers are not the same; 9 to 13 kc/sec in the swirl chamber and 4 to 5 kc/sec in the main chamber. The amplitude increases as the area ratio is lowered.

Another experiment was made under somewhat different test conditions. Fuel was injected downstream of the air-swirl through a DN8S1 type nozzle at an angle of 8° from the center line of the swirl chamber, and the brake mean effective pressure was held constant at 2.0 kg/cm$^2$. The combustion noise was picked up by a microphone whose signal was introduced to a sound level meter as well as to a cathode ray oscillograph: The

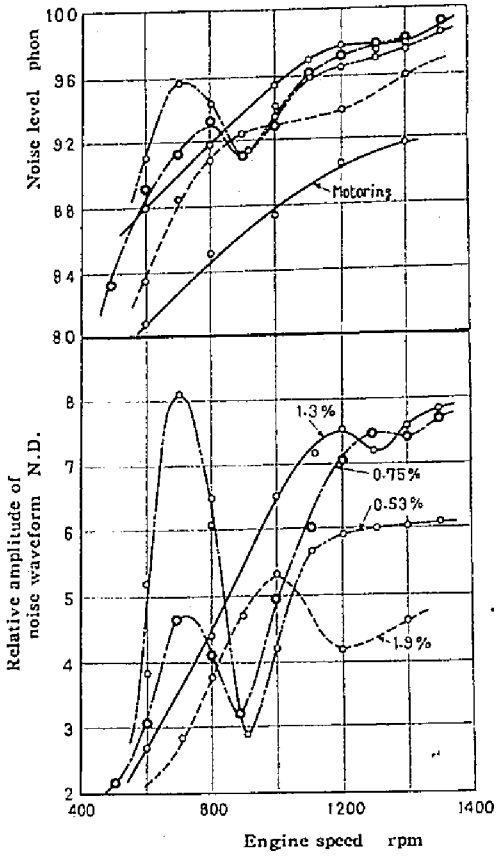


Fig. 4.5 Noise level and maximum amplitude of noise waveform at a constant load ($p_e$=2 kg/cm²)

Table 4.2

| Vibration system (Combustion chambers) concerned | Isobar surfaces of normal mode of vibration | Fundamental frequency of normal mode | Thecretical value for the testing engine $a$=750 m/sec | |
|---|---|---|---|---|
| Spherical cavity (Swirl chamber) |  | $\nu_{WA}=1.430\frac{a}{d}$ (concentric) | 29.0 kc/sec | $d$=37 mm |
| |  | $\nu_{WD}=0.633\frac{a}{d}$ (transverse) | 12.8 | |
| Cylindrical cavity (Main chamber) |  | $\nu_{HA}=1.218\frac{a}{D}$ (concentric) | 9.60 kc/sec | $D$=95 mm |
| |  | $\nu_{HD}=0.586\frac{a}{D}$ (transverse) | 4.63 | |
| Coupled resonator (Both chambers) | 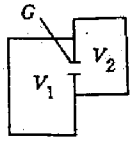 | $\nu_R=\frac{a}{2\pi}\left(\frac{f}{F}\right)^{1/4}\sqrt{\frac{D\left(\frac{1}{V_1}+\frac{1}{V_2}\right)}{1+\frac{4}{\pi}\frac{l}{D}\left(\frac{f}{F}\right)^{-1/2}}}$ | 1.93 kc/sec for 0.75%<br>2.39 1.3%<br>2.76 1.9%<br>2.63 2.2% | $V_1$=35.3 cm³<br>$V_2$=19.0 cm³<br>$l$=10 mm<br>$l$=15 mm for 2.2% only |

former informed the median of noise level and the latter the relative peak-to-peak amplitude of the noise waveform. In Fig. 4.5 the test results are summarized. It can be seen that in the higher speed range the area ratios of 0.75% and 1.3% give nearly the same noise intensity which is larger than those of 1.9% and 0.53%. In the former experiment with a constant rack position, the measurement was not made with 0.53% of f/F for the sake of an intermittent firing. This phenomenon was probably due to too small fuel quantity. Again from the figure presented above, we can see that a strong knocking occurs at the area ratios 0.53% and 0.75%. The noise intensity rapidly grows with a decreasing engine speed in the range below 900 rpm, and it attains to a maximum at near 700 rpm. This knock diminishes with a further decrease in the speed. And such a knock appearing at a low speed is absent with the larger area ratio, which is similar to what occurs with a pre-chamber type engine; namely the so-called idling knock[17].

2) The pressure oscillation in combustion chambers

As has been seen from Table 4.1, pressure oscillations in the combustion chamber can be classified into three categories. Their modes may possibly be; (1) vibration modes of the swirl chamber, (2) those in the main chamber and (3) that of vibration as coupled resonator system of Helmholz type which consists of the swirl chamber and the main chamber. They are briefly explained as follows:

(1) If the swirl chamber approximates to be fully enclosed, then the pronounced vibration modes are theoretically known according to acoustics[24]. Table 4.2 summarizes the fundamental modes and the formulae of their frequencies, where $a$ denotes the sound velocity and d the diameter of the spherical chamber. In the Table, $\nu_{WA}$ corresponds to the simplest concentric mode, and $\nu_{WD}$ to the transverse one where a fluid inside the chamber swings side to side as in a fluid in a double closed tube. The latter frequency is always lower than the former.

(2) If the main chamber is taken as a cylindrical space of an infinitely small thickness, then we can easily find out the two normal modes in the same manner as before. One of them is concentric mode $\nu_{HA}$ and the other transverse mode $\nu_{HD}$. The latter frequency also gives a lower magnitude than the former.

(3) The coupled resonator system has been also treated on the

theory of acoustics. When two chambers of $V_1$ and $V_2$ are combined with an aperture of conductivity G, the following equation of free oscillation holds with respect to the quantity q of a fluid which passes through the aperture:

$$\frac{d^2q}{dt^2} + a^2G\left(\frac{1}{V_1} + \frac{1}{V_2}\right)q = 0 \qquad (4.1)$$

where G is equal to the diameter of the aperture if it is circular and if its length is negligibly small as compared with its diameter. The conductivity of a non-circular aperture may be reasonably assumed to be that of an equivalent circular aperture of diameter $d_e$, whose area is the same as the non-circular one under consideration. If the length of the aperture $l$ is not negligible, the following correction is to be made:

$$G = \frac{d_e}{1 + \frac{4l}{\pi d_e}} \qquad (4.2)$$

Consequently, the frequency of free oscillation $\nu_R$ due to the combination of two chambers is represented, by using the cylinder diameter D and the area ratio of the connecting passage area f/F, as follows:

$$\nu_R = \frac{a}{2\pi}\left(\frac{f}{F}\right)^{1/4} \times \sqrt{D\left(\frac{1}{V_1} + \frac{1}{V_2}\right)\left\{1 + \frac{4}{\pi}\frac{l}{D}\left(\frac{f}{F}\right)^{-1/2}\right\}^{-1}} \quad c/sec \qquad (4.3)$$

In addition, it has been proved that the normal frequency of each chamber is not altered by an attachment of any resonator.

In order to compare this theory with the experimental results, it is necessary to estimate the sound velocity $a$ at the end of pressure rise. Now we denote the temperature and pressure at the compression beginning as $T_b$ and $p_b$ respectively and the temperature, pressure and sound velocity at the atmosphere as $T_o$, $p_o$ and $a_o$ respectively. If the effect of the residual gas on the volumetric efficiency of the charge $\eta_v$ is neglected, then we obtain

$$\eta_v = \frac{p_b}{p_o}\frac{T_o}{T_b}$$

If the maximum pressure appears at TDC, the relationship between the maximum gas temperature $T_{max}$ and $T_b$ is given by

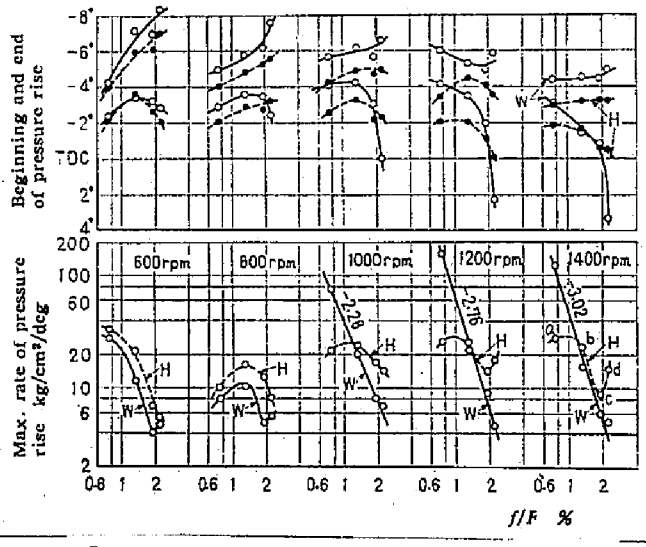


Fig. 4.6 Relationship between f/F and maximum rates of pressure rise together with the period of pressure rise

$$\frac{T_{max}}{T_b} = \frac{1}{\varepsilon} \frac{p_{max}}{p_b}$$

where $\varepsilon$ denotes the compression ratio. We can rewrite this formula by using the volumetric efficiency, as follows:

$$\frac{T_{max}}{T_o} = \frac{1}{\varepsilon \eta_v} \frac{p_{max}}{p_o}$$

or

$$\frac{a}{a_o} = \frac{1}{\sqrt{\varepsilon \eta_v}} \left(\frac{p_{max}}{p_o}\right)^{1/2} \qquad (4.4)$$

Here the numerical values are: $\varepsilon$=16.0, $\eta_v$=0.80 (assumption), $a_o$= 340 m/sec, $p_{max}$=65 kg/cm$^2$; $p_{max}$ is an average peak pressure obtained from the indicator diagrams where the pressure overshoots due to the oscillations being neglected. The sound velocity corresponding to the maximum pressure is then 750 m/sec.

In Table 4.2 are shown the frequencies of the normal modes of pressure oscillations calculated from the dimensions of the testing engine. Comparing these with the measured frequencies, it is known that, excluding the case of 2.2% of f/F, the predominant frequency in the swirl chamber is more related to $\nu_{WD}$ and that in the main chamber to $\nu_{HD}$. When f/F is 2.2%, the mode of oscillation will probably be of the combined chambers, notwithstanding that the theoretical value of the frequency is considerably larger than the measured value. The discrepancy between them may be due to the fact that the assumption of the theory that the main chamber is to be a space without depth, will give too small component which acts as inertia in the system.

3) Pressure rate in the swirl chamber

In Fig.4.6 the maximum rates of pressure rise versus the area ratio of the connecting passage are replotted for each engine speed. At the engine speed higher than 1000 rpm, the maximum rate of pressure rise in the swirl chamber $(dp_W/d\theta)_{max}$ roughly obeys the following rule:

$$(dp_w/d\theta)_{max} \propto (f/F)^{-(2.3\sim3.0)} \qquad (4.5)$$

It may be seen that a slight decrease in f/F causes a rapid growth of the maximum rate of pressure rise. This will be partly because the combustion development approaches a constant-volume one as the area

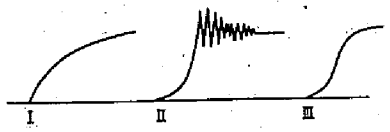


Fig. 4.7 Typical modes of pressure development in cylinder

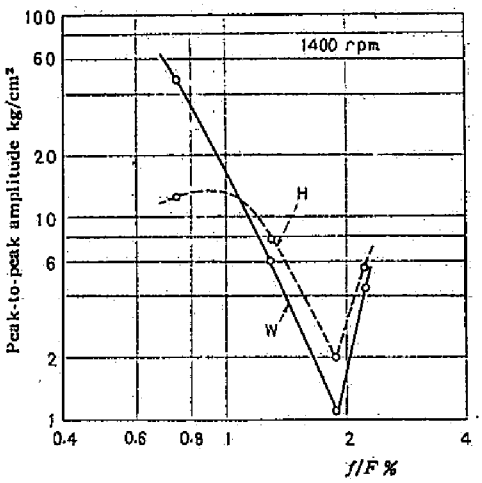


Fig. 4.8 Peak-to-peak amplitude of pressure oscillation in each combustion chamber

ratio is reduced, and partly because the rate of mixture formation increases as the velocity of air streaming into the swirl chamber, thus deepening the feature of an explosion.

Recently, Sitkei refers to the variety of combustion development in the diesel engine, in the relation between chemical reaction and the rate of heterogeneous mixture formation, as follows[25]:

(1) When the velocity of the mixture formation is surpassed by the velocity of reaction, there arises a so-called diffusion type combustion. This is characterized by a short ignition delay and the pressure-time trace is like curve I in Fig. 4.7.

(2) When the mixture formation velocity is considerably higher than the reaction velocity, the mass velocity of burning changes according to the S-shaped curve as III. In these cases there is a homogeneous mixture in the entire space at the beginning where flame is spreading, in the same way as in a carburetter engine.

(3) If the duration of mixture formation accords with the duration of chemical reactions, then the phases of mixture formation and of pre-oxydation process become interwoven with one another and fields of different concentrations will develop. In these cases, the combustion is very rapid and occurs in a detonation-like manner as curve II.

It can be seen in the present experiment that the pressure-time trace in the swirl chamber becomes nearer to curve II as f/F is lowered. From this, we can deduce that the pre-oxydation process is largely influenced by the intensity of air swirl present in the swirl chamber. When an ignition is made by an ignition agent with a gasoline engine, we can observe a similar rapid pressure rise accompanied with an intense pressure oscillation, under a proper condition of running[26].

Fig. 4.8 shows the amplitude of pressure oscillation against the area ratio of the connecting passage at 1400 rpm. The oscillation is weakest with 1.9% of f/F and rapidly grows as the area ratio decreases. With 2.2% the amplitude is larger than with 1.9% but its mode is not the one of 1.9%; namely the transient vibration of two chambers. According to the analysis by a water model in CHAPTER 3, the amplitude of such a transient vibration increases with f/F, which accords with the fact mentioned above.

4) Pressure rate in the main chamber

As seen from Fig. 4.6, the rate of pressure rise in the main chamber follows quite different trends from that in the swirl chamber, and, above 1000 rpm, the curves are wavy. In the upper half of the same figure are shown the beginning and the end of a rapid pressure rise for each combustion chamber. It can be seen that the relative timings of pressure rise are changed by the area ratio, and that the curves have some trends in common with each other in the speed range above 1000 rpm. If the case of 1400 rpm is taken as an example, the following elucidations will be made for the maximum rate of pressure rise and its timing:

In the case of a very small area ratio (a), the pressure rise in the main chamber begins belatedly after the swirl chamber has completed its pressure rise. Owing to this delay and to the repressed transmission of a sharp pressure rise due to the narrow passage, the main chamber shows a lower rate than the swirl chamber. As the area ratio increases, the rate in the swirl chamber becomes smaller but the transmission of rapid pressure rise to the main chamber is facilitated, so that the rate of pressure rise in the main chamber tends to approach that in the swirl chamber and the rates in both chambers coincide with each other at the point b. An increase in the area ratio over the point c yields a rapid combustion probably due to an easy outflow of unburned combustible mixture, thus the rate in the main chamber exceeding that in the swirl chamber and the end of pressure rise in the main chamber coming before the rise in the swirl chamber is completed. In the case of point d, we may consider that the gas inside the main chamber is sent back to the swirl chamber owing to the gas oscillation at the end of pressure rise. At the point c, therefore, the growth of the rate of pressure rise due to combustion in the main chamber is cancelled by the inclination of the rate of pressure rise diminishing in the swirl chamber, thus resulting in a minimum value of the rate at the point c.

In the lower speed range below 800 rpm, no general tendency can be found out and the rate of pressure rise in the main chamber is always higher than that in the swirl chamber. A feature of idling knock is remarkable at 600 rpm where the rates of pressure rise in the swirl and main chambers grow as the area ratio is reduced. When f/F is 0.75% at


Fig. 4.9

this speed, the pressure-rises in both chambers begin at nearly the same moment and complete simultaneously. So we can conclude that a considerable amount of unburned fuel must have exploded in the main combustion chamber.

## 4.3 Unburned Mixture Issuing from the Swirl Chamber to the Main Chamber

### 1) Thermodynamics of the process

In the previous section, it was found that the rate of pressure rise in the main chamber of a swirl chamber type diesel engine was higher than that in the swirl chamber except when the area ratio of the passage connecting both chambers was very small, and that the larger the area ratio the greater was the difference between the rates of pressure rise. It can be predicted from this fact that there is a considerable amount of fuel which outflows from the swirl chamber into the main chamber in an unburned state. Since the amount of fuel and its burning velocity are probably governed by the area of the connecting passage, we have to consider this effect as one of the important action of the connecting passage upon knocking. For this purpose, a thermodynamic consideration was carried out through finding out the relationship between the quantity of unburned mixture discharging from the swirl chamber and the area of the connecting passage.

In a swirl chamber having a volume V and an area of the connecting passage f, as shown in Fig. 4.9, a homogeneous mixture of air and finely atomized fuel well distributed over the combustion chamber ignites at t=0 and burns uniformly at a given local mass-fraction x=x(t). Denoting pressure, temperature and total weight of gas inside the chamber as p, T, and G respectively, the heat release in the chamber in an infinitesimal duration is

$$dQ = h_u G \, dx \quad \cdots\cdots\cdots \qquad (4.6)$$

As the unburned mixture occupies the fraction (1 - x) of the total weight of gas, the unburned mixture d $G_u$ contained in the gas passing the connecting passage is

$$dG_u = -(1-x)\, dG$$

Consequently, summation of the unburned mixture transferring to the main chamber is

$$G_u = -\int_{x=0}^{x=1} (1-x)\, dG$$

Denoting $G_o$ as the initial weight of gas in the swirl chamber and using $y = G/G_o$ and $y_u = G_u/G_o$, we can rewrite the above formula as follows:

$$y_u = \frac{G_u}{G_o} = -\int_{x=0}^{x=1} (1-x)\, dy \tag{4.7}$$

For the convenience, $y_u$ will be called fraction of unburned mixture or discharge of unburned mixture.

If the ideal gas rule holds inside the chamber and if there is no increase in the number of molecules of gas, then the energy balance of the considering system is

$$C_u d(GT) = dQ + \kappa C_v T\, dG \tag{4.8}$$

where $\kappa$ is the ratio of specific heats and $c_v$ the specific heat at constant volume. The equation of discharge of gas through the connecting passage is

$$-\frac{dG}{dt} = \mu f \sqrt{2g \frac{pG}{V}}\ \psi$$

where

$$\psi = \begin{cases} \sqrt{\dfrac{\kappa}{\kappa-1}\left\{\left(\dfrac{p_o}{p}\right)^{2/\kappa} - \left(\dfrac{p_o}{p}\right)^{(\kappa+1)/\kappa}\right\}} & \text{for } \dfrac{p_o}{p} \geq \left(\dfrac{2}{\kappa+1}\right)^{\kappa/(\kappa-1)} \\ \left(\dfrac{2}{\kappa+1}\right)^{-(\kappa-1)} \sqrt{\dfrac{\kappa}{\kappa+1}} & \text{for } \dfrac{p_o}{p} < \left(\dfrac{2}{\kappa+1}\right)^{\kappa/(\kappa-1)} \end{cases} \tag{4.9}$$

where $\mu$ is coefficient of discharge of the connecting passage. In the present case, pressure outside the chamber $p_o$ is assumed to be constant. By Eqs. (4.6) to (4.9), $y_u$ can be determined. Denoting $T_o$ as the initial temperature, we can rewrite Eq. (4.8) as follows:

$$d\left(\frac{p}{p_o}\right) = \frac{h_u}{C_v T_o} \frac{G}{G_o} dx + \kappa \left(\frac{p}{p_o}\right) \frac{dG}{G} \tag{4.10}$$

or, using $P = p/p_o$ and $\theta = T/T_o$,

$$\frac{dP}{dt} = \frac{h_u}{C_v T_o}\, y \frac{dx}{dt} + \kappa \frac{P}{y} \frac{dy}{dt} \cdots \tag{4.11}$$

Similarly, Eq. (4.9) is reduced to

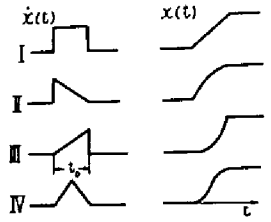


Fig. 4.10 Mass fraction of burning x(t) and its velocity ẋ(t)

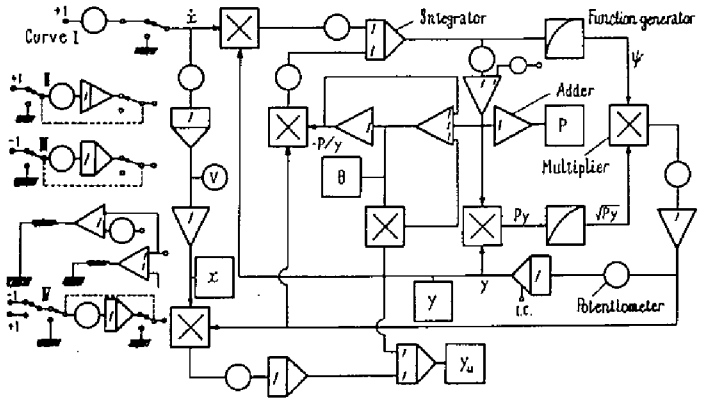


Fig. 4.11 Analog circuit diagram

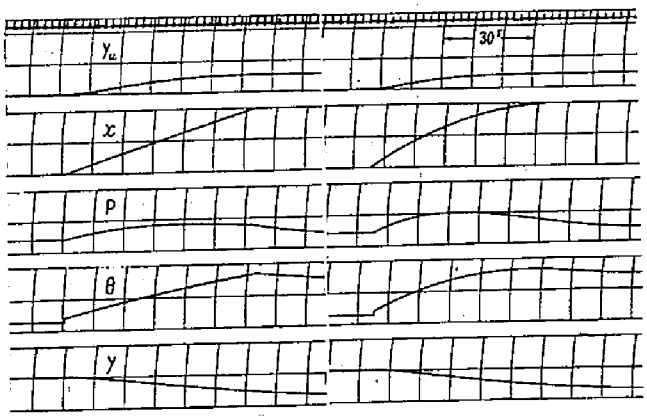


Fig. 4.12 Curves of solution

$$-\frac{dy}{d\tau} = \frac{\mu f}{V}\sqrt{2gRT_o}\sqrt{Py}\,\psi \tag{4.12}$$

where R denotes gas constant. Besides, the ideal gas rule is

$$P = y\theta \tag{4.13}$$

Further, using the non-dimensional time $\tau = t/t_o$, where $t_o$ is period of burning in the swirl chamber, we obtain the following non-dimensional equations from Eqs. (4.11) and (4.12).

$$\frac{dP}{d\tau} = \frac{hu}{c_v T_o}\, y\frac{dx}{d\tau} + k\frac{P}{y}\frac{dy}{d\tau} \tag{4.14}$$

$$\frac{dy}{d\tau} = -k\sqrt{Py}\,\psi \tag{4.15}$$

where characteristic number of the area of connecting passage k is

$$k = t_o \cdot \frac{\mu f}{V}\sqrt{2gRT_o} \tag{4.16}$$

From these equations we calculate

$$y_u = -\int (1-x)\,dy \tag{4.17}$$

2) Solution of equations

As it was impossible to integrate the simultaneous equations in an analytical form, they were solved by using an electric analog-computer. In Fig. 4.10 are shown the mass fractions of burning x(t) and its rates x(t), which were adopted in the analogue computation: Curve I is the case when the burning rate is constant during combustion, curve II the case when the rate decreases with time, curve III the case when the rate increases with time or the fraction of burning increases in proportion to square of time, and curve IV the case when the burning rate changes like an equilateral triangle. Fig. 4.11 shows the circuit for the computation of Eqs. (4.13) to (4.17). In the circuit, diode-function generators were used for realizing functions $\psi = \psi$ (P) and $\sqrt{yP}$. As their solutions, typical oscillograms are shown in Fig. 4.12. In this, the numerical number of calorific value $h_u/c_v T_o$ was determined by the following data: Air temperature at the beginning of compression stroke $T_b$ is 100°C, average magnitude of polytropic index during the compression stroke m=1.35, compression ratio $\varepsilon$=16, lower calorific value of fuel

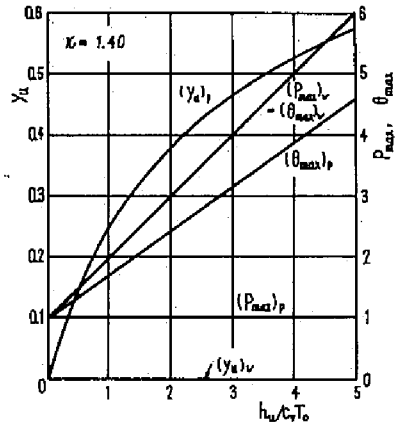


Fig. 4.13 $h_u/c_vT_o$ versus $y_u$, $P_{max}$ and $\theta_{max}$ at constant volume burning $(\ )_v$ and constant pressure burning $(\ )_p$

$H_u = 10^4$ kcal/kg, specific heat at constant pressure $c_p$=0.24 kcal/kg°C (air), ratio of specific heats $\kappa$ =1.40, stoichiometric air consumption $L_o$=14.0 kg air/kg fuel. The air temperature at the end of compression stroke reaches $T_c$=973°K, which we can approximate as the initial temperature of burning $T_o$ of the present problem. Thus, for excess-air coefficients $\lambda$ =1 and 2, $h_u/c_vT_o$ give 4 and 2.07 respectively. These values will be used in the present computation.

When the characteristic number k or its reciprocal 1/k is naught, combustion process of constant volume or constant pressure is materialized. For such cases we can analytically find out the pressure change and discharge quantity of unburned fuel, as in the following manner.
(1) Case of k=0 (correponding to constant-volume burning): Because $dy/d\tau$ =0 holds as seen from Eq. (4.15), we have y =1 and $\theta$= P throughout the process. Integrating Eq. (4.14), we obtain

$$P = \theta = \frac{h_u}{c_v T_o} x + 1 \quad , \quad y_u = 0 \tag{4.18}$$

(2) Case of 1/k=0 (corresponding to constant-pressure burning): Although such a situation can be realized by no means, it is meaningful in making a border on the value of $y_u$ for large area of the connecting passage. In this case, instead of Eq. (4.15), $dp/d\tau$ in Eq. (4.14) can be assumed to be naught because the pressure in the swirl chamber is always equal to the ambient pressure $p_o$. So we obtain

$$\frac{h_u}{c_v T_o} y \frac{dx}{d\tau} + \kappa \frac{P}{y} \frac{dy}{d\tau} = 0$$

By using the notation $\beta = h_u/c_vT_o$ and the initial condition y = 1 at x = 0, the above equation is easily integrated to produce

$$y = \frac{1}{\beta x + 1} \quad , \quad \frac{dy}{dx} = -\frac{\beta}{(\beta x + 1)^2}$$

Therefore $y_u$ becomes

$$y_u = 1 - \frac{1}{\beta} \ln (1 + \beta) = 1 - \frac{\kappa c_v T_o}{h_u} \ln \left(1 + \frac{h_u}{\kappa c_v T_o}\right) \tag{4.19}$$

and, from Eq. (4.13), $\theta$ becomes,

$$\theta = 1 + \beta x = 1 + \frac{h_u}{\kappa c_v T_o} x(t) \tag{4.20}$$

In Fig. 4.13 are summarized the maximum pressure $P_{max}$, maximum temperature $\theta_{max}$, together with the total discharge of unburned mixture $y_u$,

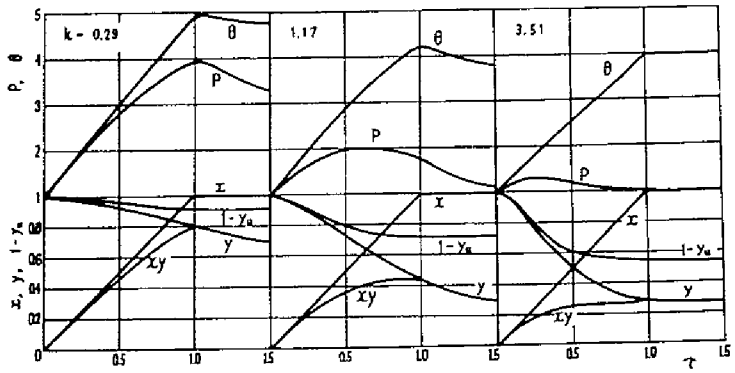


Fig. 4.14 Course of burning for $h_u/c_vT_0 = 4$

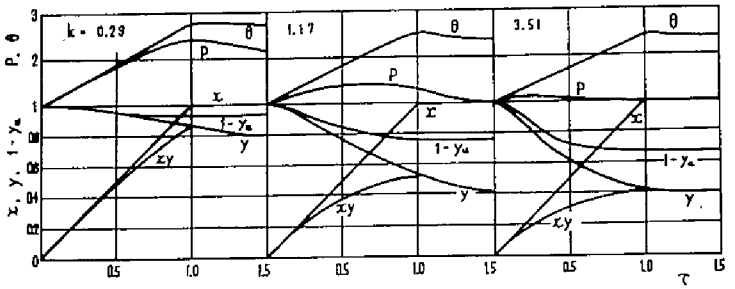


Fig. 4.15 Course of burning for $h_u/c_vT_0 = 2$

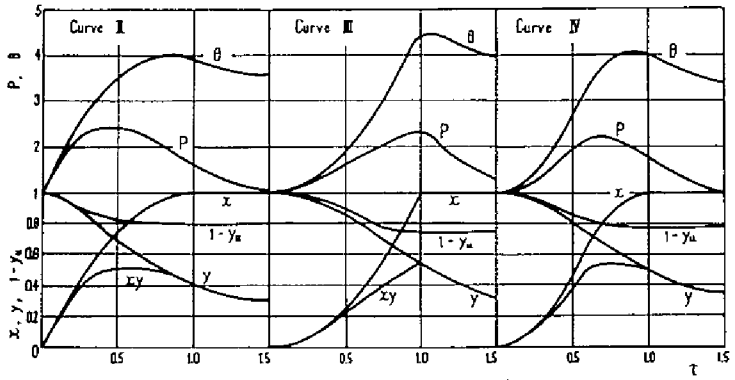


Fig. 4.16 Course of burning for various x(τ)'s at $h_u/c_vT_0 = 4$ and k = 1.17

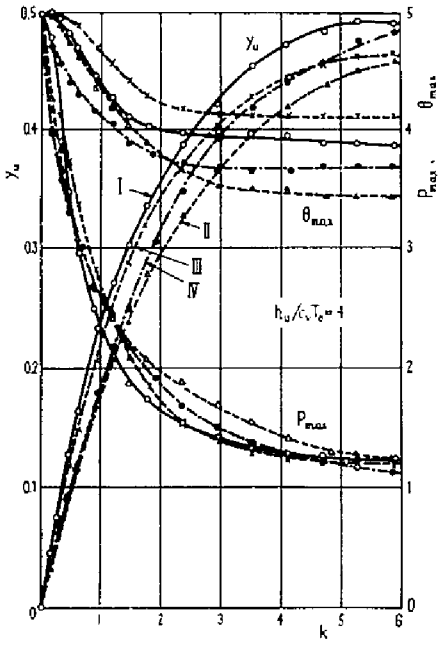


Fig. 4.17 Effect of k on $y_u$, $P_{max}$ and $\theta_{max}$ at $h_u/c_vT_0 = 4$

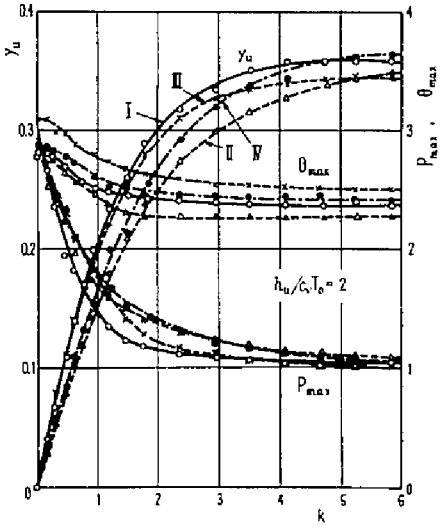


Fig. 4.18 Effect of k on $y_u$, $P_{max}$ and $\theta_{max}$ at $h_u/c_vT_0 = 2$

for each case of constant volume $(\ )_v$ and constant pressure $(\ )_p$.

In Figs. 4.14 and 4.15 are shown the courses of combustion obtained by the analog-computer for various values of k and $h_u/c_vT_o$, where the mass fraction of burning is curve I. In each diagram, the following curves are drawn; namely, temperature of gas $\theta$, pressure P, weight of gas inside the chamber y, accumulation of unburned mixture outside the chamber $y_u$ and product of x and y. At the instant of ignition, the temperature and pressure begin to rise, and the mixture of burned and unburned gases issues from the connecting passage. Of course, the smaller is k the more the pressure rise in the swirl chamber and the longer the outflow continues. After the mixture burns itself out at $\tau=1.0$, the outflow of gas produces no further increase in $y_u$. Final value of $y_u$ clearly increases with k, and, at k=3.5, reaches 46% and 33% for $h_u/c_vT_o$=4 and 2 respectively. The corresponding value at constant pressure $(y_u)_p$ is, from the previous figure, 53% and 38% for each carorific value.

Fig. 4.16 shows the effect of curve form of $x(\tau)$ on the course of burning. It can be seen that the fraction of unburned mixture outflown is passably dependend on the course of heat release in the swirl chamber; for a given value of k, final magnitudes of $y_u$ are 28% for curve I, 20% for curve II, 25% for curve III and 22% for curve IV. Among curves II to IV, II is the nearest to the constant volume combustion in the earlier stages and III the furthest, so that the discharge of unburned mixture is the most with III and the least with II. It is worthy of special attention that curve I gives a far larger value than curve III.
Figs. 4.17 and 4.18 show $y_u$, $\theta_{max}$ and $P_{max}$ against k for each type of burning. It can be seen that $y_u$ increases monotonously with k.

3) Application to practical case

In the previous section, we have seen that the rate of pressure rise in the main chamber becomes out of proportion to that in the swirl chamber when the area ratio of the connecting passage is very large or small. In the bottom of Fig. 4.19, a portion of previous test results is reproduced. As seen from this,the pressure rate in the main chamber becomes higher and lower than that in the swirl chamber for large and

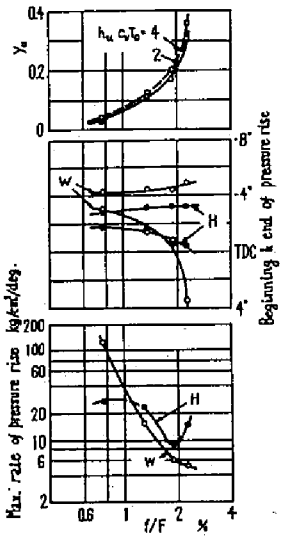


W denotes the swirl chamber and H the main chamber.

Fig. 4.19 Rate and period of pressure rise with a swirl chamber type motor, together with the amount of unburned mixture outflown

small f/F respectively. This inclination was attributed to the fuel burning in the main chamber.

For the sake of a better confirmation of it, it was attemped to know a rough estimate of fraction of unburned mixture outflown into the main chamber to the total mixture initially present in the swirl chamber, in the practical case, by applying the result of computation presented above. If the system is approximated to be the simple model, then the mass fraction of transferred mixture can be given by replotting $y_u$ from Figs. 4.17 and 4.18. When we rewrite the characteristic number of the connecting passage k by using f/F, engine speed n in rpm and duration of burning $\varphi$ in degree of crank angle, we obtain

where

$$k = k_0 \frac{100\, f/F}{n/1000}\,\varphi \qquad (4.21)$$

$$k_0 = \frac{\mu F}{6V}\sqrt{2gRT_0} \times 10^{-5}$$

Here $k_0$ represents the characteristic number at f/F=1 %, n=1000 rpm, $\varphi = 1^{\circ}$. Dimensions of the testing engine were as follows: Cylinder diameter and stroke were 95 mm and 115 mm respectively, engine speed 1400 rpm, compression ratio 16, ratio of volume of the swirl chamber to the total compression space $V/V_c$=0.63 and volume of the swirl chamber V=34.2 $cm^3$. Thereupon the magnitude of $k_0$ represents 0.168. The duration of burning $\varphi$ is known from the measured rising time of pressure in the swirl chamber, which is illustrated in the middle of Fig. 4.19. As the mass fraction of burning x(t) remains unknown, curve I is conveniently adopted here.

In the top of Fig. 4.19 is shown the result of estimation of $y_u$ for two kinds of $h_u/c_vT_0$. Comparing $y_u$ with maximum pressure-rates, the following things are known: In the case of 0.75% of f/F, gross amount of unburned mixture outflown is from 2 to 3%; the main bulk of the fuel injected burns in the main chamber and thereby the substantial part of pressure rise seems produced by an ejection of hot gas from the swirl chamber. With an increase in the area ratio, the outflow of unburned mixture grows. Since, in the range of f/F from 1.3% to 1.9%, a considerable amount of unburned mixture outflows and burns in the main chamber, thus assisting the pressure rise in it, the pressure rate in the main chamber is nearly equal to, or slightly higher than that in the swirl chamber. In the case of large dimension of the connecting passage, an unburned mixture can be transferred much from the swirl chamber to the main chamber; it attains a fraction of 30% to 35% of the initial weight at 2.2% of f/F.

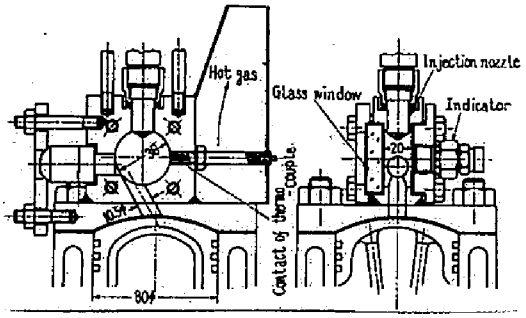


Fig. 4.20 Apparatus for photographing combustion

In such a range pressure rise is accelerated powerfully by the combustion in the main chamber, while the outflow of high temperature gas becomes weakened, therewith resulting in a high rate of pressure rise in the main chamber compared with that in the swirl chamber.

## 4.4 Influences of Direction of Fuel Spray and Wall Temperature upon Combustion

As has been described in Section 4.1, the aim of the further study is to reveal the influences of both the spray direction and the wall upon the mixture formation of fuel and combustion process in a full scale engine with a strong swirl present in the swirl chamber. The observation of the combustion process was made mainly by means of high-speed photography and indicator diagrams. Some further study was carried out to grasp the essentials of the combustion mechanism of the so-called M-combustion system[3] which has been characterized by an extreme utilization of the wall and the air swirl.

### 1) Apparatus for observing combustion

In order to visualize the progress of the mixture formation, ignition, and subsequent combustion, a cylindrical swirl chamber with a specially strengthened glass window has been mounted on a loop-scavenged two-cycle engine; cylinder bore 80 mm, stroke 90 mm, and stroke volume 0.452 $\ell$. The combustion chamber has dimensions of 36 mm in diameter and 20 mm in width, as shown in Fig. 4.20. The volume ratio of the swirl chamber to the total compression volume was chosen as large as 86% so that the greater part of the combustion might be completed in it. The area ratio of the connecting passage to the piston area has been 1.72%, while the compression ratio being 19.0 and the effective ratio being 13.0. With this configuration, one can estimate the maximum air velocity in the swirl chamber attainable as high as 135 m/sec during the compression stroke, at an engine speed of 1250 rpm.

To remove the influence of the residual gas and to simulate the better scavenging efficiency obtainable in a four-stroke engine, the engine was fired in every other revolution, thus affording double scavenging to every power stroke. The amount of 17 mg fuel was injected for every firing stroke through a 0.35 mm -orifice injector at four

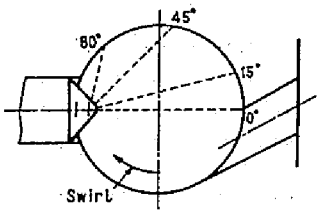


Fig. 4.21 Directions of fuel injection

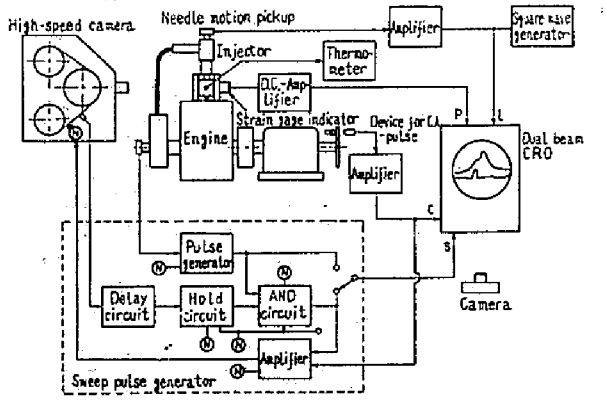


p: pressure in the combustion chamber,
l: injector needle motion,
c: crank angle,
s: signal for sweeping,
N: neon indicators

Fig. 4.22 Schematical arrangement of apparatus

different directions, namely 0-, 15-, 45-, and 80 deg., as shown in Fig. 4.21, the angle measured from the diametral line of the chamber toward the down stream of the swirl, which will be designated as the direction of fuel injection. The fuel used was a diesel oil of specific weight 0.785 and cetane number 72, and the injection pump was Bosch type PE1A50B101.

The temperature of the chamber wall was controlled by a gas burner and measured with an Alumel-Cromel thermccouple inserted close to the wall surface, as shown in Fig. 4.20. Since the temperature distribution of the wall would be considerably influenced by the period of the motored and/or fired running, the measured wall temperature may only be used as a qualitative indication of the surface temperature. For this reason, time for preparation was made as short as possible to make the test condition even. The maximum temperature attainable was 350°C, which, limited by the use of a glass window, seems nevertheless sufficient for the practical engine.

A 16mm Hitachi KPC-25 type high-speed camera was used as a viewer, having a maximum speed of 2500 frames per second, which corresponds to about a hundred pictures per revolution of the engine shaft at a speed of 1250 rpm. On the photographed film marks of the timing and crank angle were recorded.

The indicator diagrams were single-swept on the cathode-ray tube of a dual-beam oscillograph equipment, in such way that they might be sampled among cycles that were taken by the high-speed camera. As the transducer of the pressure in the combustion chamber, a strain-gage type indicator, which has a natural frequency higher than 35 kc/sec, was attached to the chamber wall directly as shown in Fig. 4.20, for the sake of avoiding a harmful pressure vibration caused by any indicator passage. The injector needle motion was detected by a magnetic pickup, whose output was, after amplification, superposed upon 0.1 kc/sec-square wave for timing mark, then led to one of the Y-axes of the oscillograph. The crank-angle pulses of every 20 degrees were generated photoelectrically by a slit disk fixed on the engine shaft, and were recorded in the oscillograph as well as in the high-speed camera. Fig. 4.22 shows the measuring system schematically, including a control unit devised to synchronize the indicator diagrams with high-speed photographs or to take indicator diagrams only.

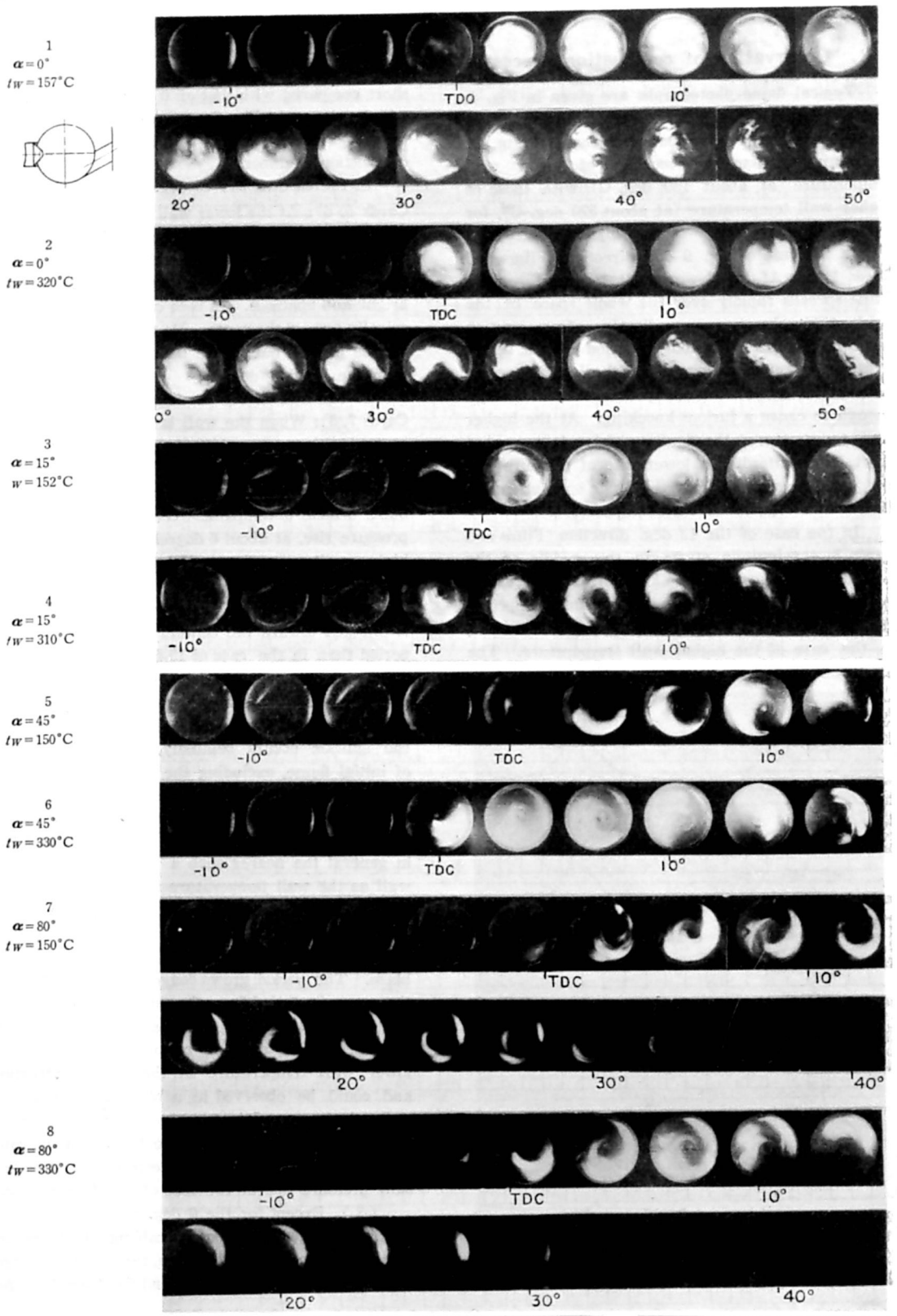


Film speed is 1900 to 2100 frames per second.

Fig. 4.23 Flame photographs for various angles of fuel injection α and wall temperatures $t_w$

2) Observation of combustion process

Typical flame photographs are given in Fig. 4.23, and corresponding indicator diagrams in Fig. 4.24 (numerical numbers are equivalent to those of Fig. 4.23), contrasting combustion processes of lower wall temperature (at about 150°C) with those of higher wall temperature (at about 320°C) for four different directions of fuel injection.

In the case of the 0 deg. direction (Films and Cards 1,2): At the lower wall temperature, the flame spreads rapidly over the whole space of the combustion chamber immediately after the ignition occurs, and lasts for a longer period with a bright light, to get out of shape in the later stage of combustion. The rate of pressure rise is high enough to cause a furious knocking. At the higher wall temperature, the ignition delay is somewhat short, thus affording a lower rate of pressure rise and peak pressure. The flame has a smaller spread than that of the lower wall temperature.

In the case of the 15 deg. direction (Films and Cards 3,4): Ignition starts in the middle of the chamber in the case of the lower wall temperature, and in the vicinity of the wall near the connecting passage to where spray particles move in an arc, in the case of the higher wall temperature. The flame never ceases to rotate until its extinction, in the meanwhile there is a dark space left in the center of the swirl. The flame is bright when the wall is hot. The duration of combustion is fairly short compared with that of 0 deg. direction.

In the case of the 45 deg. direction (Films and Cards 5,6): At the lower wall temperature, ignition starts from about the middle part of the chamber, but in the vicinity of the wall at the higher wall temperature. In the latter case the flame appears bright and spacious. In both cases the flame moves spirally toward the center. No remarkable difference can be pointed out in the indicator diagrams, other than the ignition delay.

In the case of the 80 deg. direction (Films and Cards 7,8): When the wall is at the lower temperature, ignition starts close to the connecting passage after a longer delay, and an initially dark flame with a slow pressure rise is followed by a regular blaze which accompanies the maximum rate of pressure rise, at about 6 degrees after TDC. At the higher wall

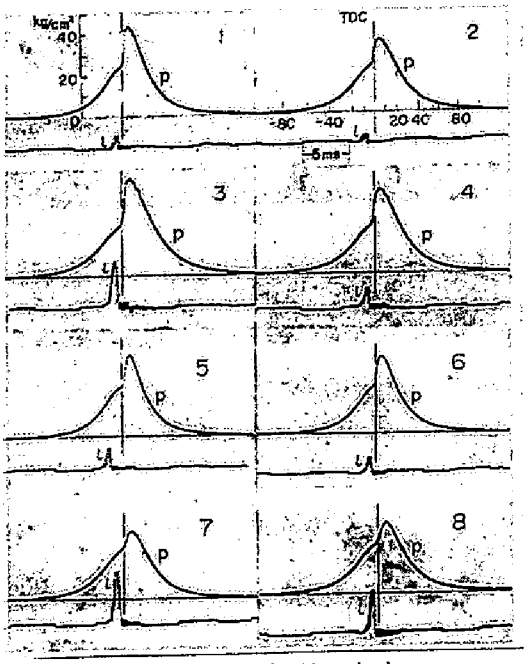


p: pressure in the combustion chamber,
l: injector needle motion,
Numerical numbers correspond to those in Fig. 4.23.

Fig. 4.24 Indicator diagrams

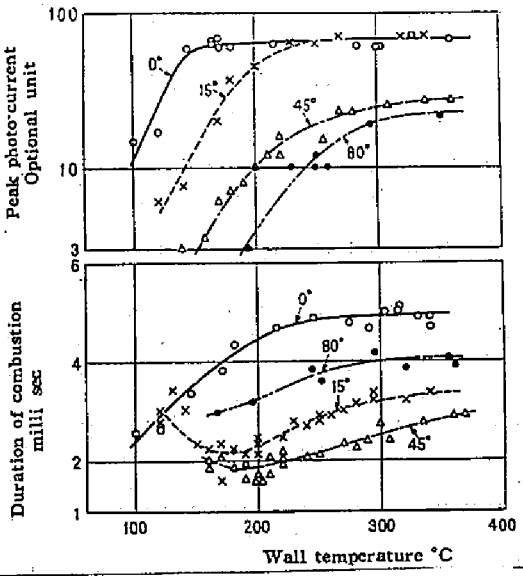


Fig. 4.25 Duration of burning and peak current of the photo-transistor

temperature, no initial dark flame is present and the pressure rise rapid at first but decelerated later. In both cases, the steady flame is dragged toward the center and lasts for a longer period than in the case of 15-and 45 deg. directions.

From the above mentioned observations and experiments, the followings have been deduced:

(1) In the case of a lower wall temperature, the ignition occurs belatedly, the possible location of initial flame, excluding the case of the 80 deg. direction, being at the center of the chamber to where fuel particles have been dragged. It has been found from several flame photographs that in general the nearer such a spot appears to the wall as the wall temperature increases.

(2) Immediately after inflammation, there exists a period in which the combustibles emit a faint light before the flame turns into a regular blaze. This period grows longer as the direction of the spray is varied from the center toward the wall, and becomes shorter as the wall temperature increases. This appears remarkably long with a lower wall temperature at the 80 deg. direction and was observed to be a blue flame period by the naked eye, while for the other directions it could not be ascertained to be so. In indicator diagrams, such a period corresponds to the very slow pressure rise at the foot of rapid ascending.

(3) Except for the 0 deg. direction, the flame continues to swirl without crumbling till its extinction. For the 80 deg. direction, the flame is dragged towards the center with one end fixed steadily upon the wall. For the 0 deg. direction, however, the flame spreads out gradually from the center in the form like a cumulo-nimbus to cover the greater part of the chamber, changing into an irregular form in the final phase of combustion.

(4) The duration of visible light emission is long with 0 and 80 deg. directions, and short with 15 and 45 deg. directions. To inquire into this phenomenon, a photo-transistor was set in the position where the lens of the high-speed camera was located, measuring the intensity-time trace of visible light emission. The results are summarized in Fig. 4.25, from which we can see that, for a constant wall temperature, the duration is shortest with the 45 deg. direction, while with the 0 deg. direction it is longest, and that, although generally the duration of the flame increases with the wall temperature, there exist minimum points near 170°C of wall temperature, in the cases of 15

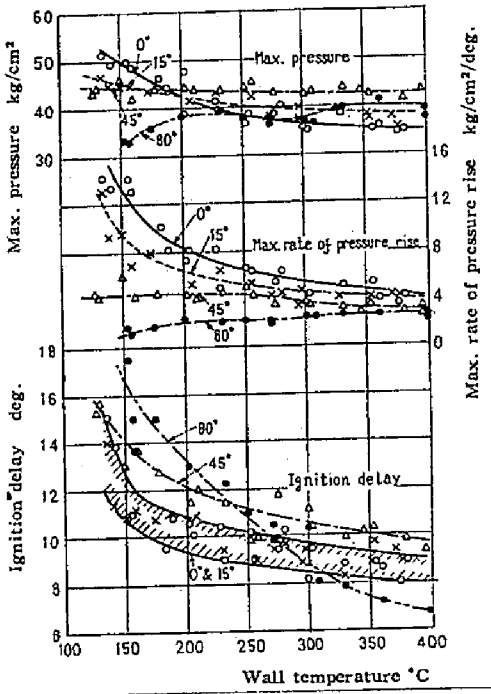


Fig. 4.26 Effect of wall temperature upon ignition delay, maximum pressure, and maximum rate of pressure rise

and 45 deg. directions.

(5) A finding concerning the maximum luminousity of the flame, also ascertained by measuring the photo-current, is that the luminousity increases as the wall temperature increases for a direction of injection and increases as the direction approaches the center of the chamber, as shown in the upper half of Fig. 4.25. No further conclusion, however, might be made out of the figure, because, besides the luminousity, the spread of the flame and the color-sensibility of the transistor must have influenced the photo-current.

(6) Several indicator diagrams were taken besides the ones synchronized with flame photographs such as Fig. 4.24. Measurement made with injection of the four directions and wall temperature ranging from 140°C to 400°C gives Fig. 4.26, which shows measured ignition delays, maximum rates of pressure rise and maximum pressures. First of all, the ignition delay is shortened with the increase in the wall temperature in every direction of fuel injection, and this trend is remarkable with the 80 deg. direction. In 0 and 15 deg. directions, considerable cycle-to-cycle variations are observed but held within the hatched domain in the figure. At a constant wall temperature, the rate of pressure rise increases definitely as the fuel is injected in more inward direction. An increase in wall temperature reduces the rate of pressure rise through the shortening of the ignition delay in the case of 0 and 15 deg. directions, while it causes no great effect in the case of the 45 deg. direction, In the meanwhile, it shows quite opposite tendency for the 80 deg. direction. At a high wall temperature, the rate of pressure rise tends to a constant value in every direction. The maximum pressure shows more complicated nature. In the 0 deg. direction, the value, very large at low wall temperature, decreases rapidly with the wall temperature, while in the 80 deg. direction, it increases with the temperature. Other directions show intermediate trends between 0 and 80 deg. directions, and the 45 deg. direction gives the highest value of all at the higher wall temperature.

3) Considerations on ignition and duration of burning

Ignition delay and location of ignition. Alcock and Watts have observed the combustion process in an engine with a transparent combustion chamber, by similar high-speed photograph technique[27]. Some of

their results are: (1) The fuel jet strikes the wall, and the resulting splash can spread some distance along the wall, playing an important part in fuel and air distribution, and (2) ignition occurs in small separate nuclei which never occur in the visible spray but usually near it or in the "wall splash".

Our observation does not conflict with these, although the behavior of the nuclei nor the splash cannot be observed because of the limitation of the film speedof camera used. Some new facts, however, are contributing to them, namely, that, for any direction of the fuel spray, ignition occurs from the middle part of the chamber in the case of a lower wall temperature, and in the vicinity of the wall when it is hot, as described in the previous paragraph. This shows that the fuel particles get more or less to the wall surface, and that, when the wall is sufficiently hot, ignition starts from the splash close to the wall, which has been heated up by the hot wall. Contrary to this, in the case of a lower wall temperature, the possibility of ignition is small, partly because the splash is cooled by the peripheral air stream which has been cooled by the wall at the upper reaches of the stream, and partly because the evaporation of the fuel adhered to the wall in the liquid phase is delayed by the cool wall surface. Consequently, ignition is apt to occur from the middle of the chamber to where the fuel is dragged.

Table 4.3 Minimum temperature able to fire

| Direction of injection | In the four-stroke operation | In the two-stroke operation |
|---|---|---|
| 0 deg. | 108°C | 94°C |
| 15 | 120 | 105 |
| 45 | 128 | 115 |
| 80 | 140 | 119 |

At a lower wall temperature of 0 and 15 deg. directions it takes long before the fuel reaches the opposite side of the wall, so that effect of the wall temperature on the ignition delay is less than that for other directions. The minimum wall temperature able to fire decreases as the direction of the injection is varied from the wall to the center, as shown in Table 4.3, in which the minimum temperature is given for the two-

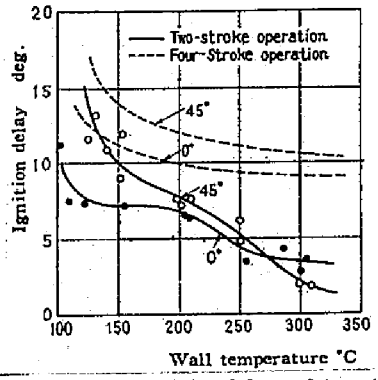


Fig.4.27 Comparison of ignition delays of two-stroke and four-stroke operations

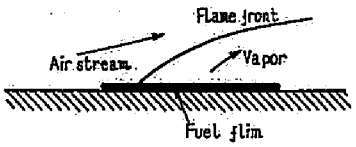


Fig. 4.28 Sketch of later flame stages of the 80 deg. direction of fuel injection

stroke operation as well.

In addition, Fig. 4.27 shows the ignition delays of the two-stroke operation, where the same amount of the fuel has been injected per firing stroke, setting forth evidently that the residual gas has a great effect for shortening the delay. Granting that, owing to the residual gas from the previous cycle, a higher gas-temperature before the ignition may bring this difference, it is interesting that raising the wall temperature shortens the delay with the two-stroke operation at higher rate than with the four-stroke operation.

On duration of combustion. The engine performance is largely effected by the later stages of combustion or the after-burning period. Hereupon, primary attention is paid to the fact that the duration of combustion is long with the two extreme directions of fuel injection, namely with the 0 and 80 deg. directions.

With the 0 deg. direction, only a smaller amount of the injected fuel is able to reach the wall, but there is apt to be generated a fuel-rich mixture in the central part of the combustion chamber where the air velocity is relatively low[22]. The combustion takes place in deficiency of air, and the unburned fuel comes to be exposed to the hot gas produced suddenly through the early explosive reaction, thus resulting in thermal cracking finally to lead to soot formation. For this reason, a longer duration is accompanied with a brighter flame. Pischinger and Pischinger have drawn illustrative examples from their bomb tests, about which they have stated that a longer ignition delay brings a shorter combustion period with a tendency to cause knocking, and that a shorter ignition delay causes a poor mixture which assists the thermal decomposition of itself[23]. With the 0 deg. direction, to which a likely explanation can be made, the duration of combustion becomes longer as the delay is shortened by the temperature rise in the wall.

In the 80 deg. direction, we have observed that the flame is dragged toward the center of the chamber with its end adhering to the wall, in the later stages of combustion. Fig. 4.28 shows a schematical view of this, where the curvature of the wall and the air stream is entirely neglected. Through the heat transfer from both the wall and the flame, the fuel adhering to the wall is gasified, and the vaporized fuel forms a flame front bordering on the fresh air stream, while the actual flame appears spread because of turbulence in the stream. According to this interpretation, it seems probable that the air velocity

of the peripheral stream of the swirl and the distribution of the liquid fuel-film spread upon the wall are most important for the burning velocity. In the swirl field weakened in the later stages of combustion, the flame lasts for a longer period But, the wall temperature being low compared to the flame temperature, the fuel is prevented from thorough cracking.

Considering these two extreme cases, we can recognize that both the incomplete combustion due to local deficiency of oxygen and the adhesion of the fuel to the wall in liquid phase are the most important governing factors for the duration of combustion. In the interim directions, combustion is protected from these influences successfully, materializing a shorter duration of combustion. In addition to these, the duration is also influenced by the outflow action, of the combustibles into the main chamber, which has been proved to govern engine performance largely [22]. According to these conceptions, the following elucidations are possible:

(1) In the 0 deg. direction of fuel injection, the duration of combustion is largely influenced by the wall temperature, as seen from Fig. 4.25, because shortening the delay causes a poor mixture. On the contrary, in the 80 deg. direction, the wall temperature has a relatively small effect upon the duration in spite of a large effect on the ignition delay, because the fuel absorbs heat for evaporation, not from the wall but mainly from the flame in the later combustion stages.

(2) There is a wall temperature to attain minimum duration of combustion, in the cases of 15- and 45 deg. directions. At less than this temperature the duration increases with the lowering wall temperature because the influence of the fuel adhering to the wall becomes predominant. At higher than that temperature, the duration increases with the wall temperature because the effect of the thermal decomposition becomes predominant.

(3) As seen from Fig. 4.26, the maximum rate of pressure rise is largely affected by the direction of fuel injection. This is because the fuel quantity that concerns the explosive autoignition, decreases as the direction of injection approaches the wall, the remainder staying at the wall.

4) Some phenomena occurring in the M-combustion system

With the 80 deg. direction, the combustible mixture formation is so

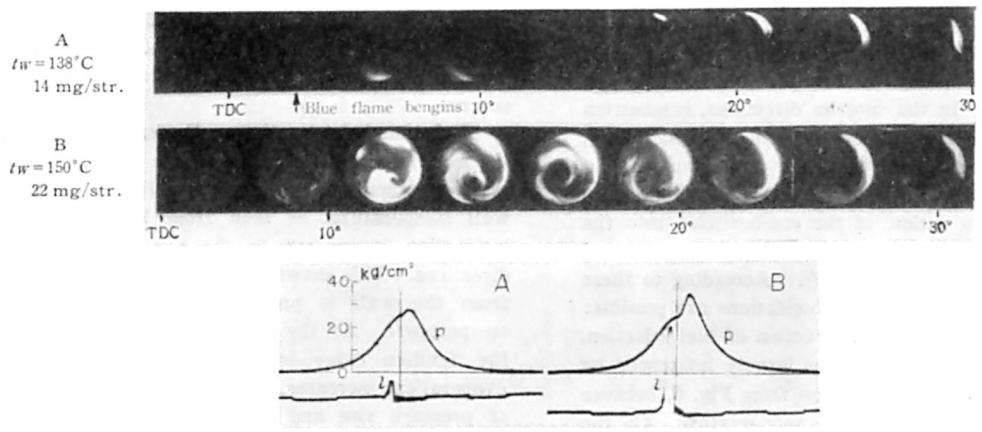


Fig. 4.29 Flame photographs and indicator diagrams of blue flame combustion (A) and ignition from several positions (B)

restrained by the wall that the maximum rate of pressure rise is very low, showing a distinctive character of M-combustion system[3]. The nature of this combustion system can be revealed to some extent by inquiring into the combustion system in the 80 deg. direction, although the situation is somewhat different from that of the actual M-engine. Some characteristic phenomena observed will be presented here for this purpose.

Relation between the wall temperature and the maximum rate of pressure rise: The maximum rate of pressure rise increases slightly with the wall temperature, as seen from Fig. 4.26, and this inclination is inverse to those of 0 and 15 deg. directions. This shows that the evaporation of fuel from the wall is prolonged when wall temperature is lower. As the wall temperature increases, the ignition delay is shortened but the rate of evaporation increases, so that the maximum rate of pressure rise and the peak pressure rise with the increasing wall temperature. As mentioned earlier in the description of the indicator diagrams, the pressure rise is slow at first but accelerated later when the wall is at a lower temperature, because the fuel is heated through the flame to be evaporated with an increasing rate by degrees.

Blue flame combustion: Under an adequate condition in the wall temperature and the fuel amount, a blue flame can survive for a relatively long period. An example of such a flame is given in Fig. 4.29 (A), showing that the first three frames are of the blue flame and that the ordinary yellow flame begins at about 17 degrees after TDC, although the only ascertainment was by the naked eye and the color film could not serve it. It is clear from the corresponding indicator diagram that the pressure attains a peak through the blue flame combustion. However, such a combustion becomes shorter or disappears with slight changes in the wall temperature or the fuel quantity, so that it seems difficult to realize a perfect evaporate-combustion throughout the whole stages of combustion in the M-system.

Ignition from several positions: Fig. 4.29 (B) shows a flame photograph of the ignition occurring simultaneously from several positions and its subsequent spread of combustion, which was taken with a relatively large amount of fuel injected. Because the flame spreads over from such several points near the wall, pressure rises more rapidly than else, and the flame is still vortical with its end fixed upon the wall. In the later stages of combustion, the form becomes similar to what has been mentioned previously, and the combustion is completed within a relatively short duration notwithstanding the larger amount of injected fuel.

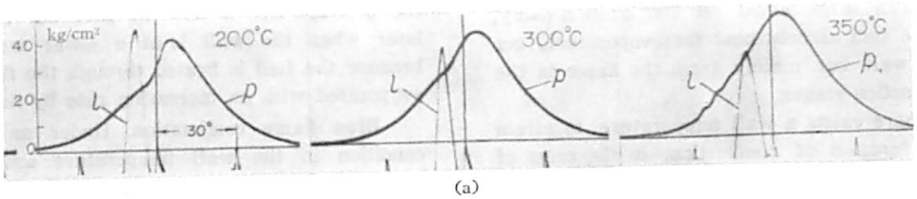


(a)

$t_W = 338°C$
17 mg/str.

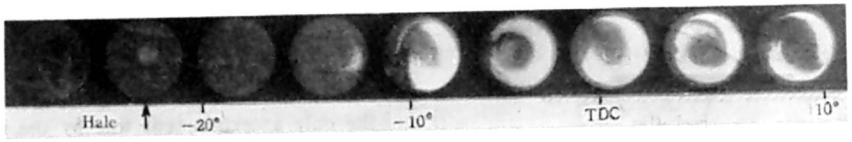


(b)

Fig. 4.30 Indicator diagrams of the 80 deg. direction in two stroke operation and flame photograph of abnormally shortened ignition delay

Abnormal shortening of ignition delay: Fig. 4.30 (a) shows indicator diagrams for different wall temperatures in the two-stroke operation. When the wall temperature is at 350°C, the pressure begins to rise above the compression line before injection, and the fuel introduced in the stroke ignites so rapidly that pressure attains a considerably high peak-pressure. It is obvious that the residue of the fuel in the chamber promotes the ignition, as observed in the flame photograph of Fig. 4.30 (b), in which there exists a faint blue flame at about 20 deg. before TDC. However, such a phenomenon cannot be found with the four-stroke operation.

## 4.5 Conclusion

The following results are obtained from the investigation on the combustion and noise of the swirl chamber type engine:

Concerning the pressure rate and dimension of the connecting passage:

(1) At an engine speed higher than 800 rpm with the testing engine, both the rate of pressure rise in the swirl chamber and the amplitude of detonation-like pressure oscillation rapidly increase with the narrowing of the passage.

(2) The relationship between the rates in the main chamber and in the swirl chamber shows three stages according to the area ratio. In the smallest area range the gas flowing out into the main chamber is delayed by the connecting passage, thereby producing a lower rate of pressure rise in the main chamber compared with that in the swirl chamber. In an intermediate area range the rate in the main chamber is nearly equal to, or slightly higher than, that in the swirl chamber.

(3) The amount of mixture outflown in an unburned state from the swirl chamber to the main chamber increases with the duration of burning as well as with the cross-sectional area of the connecting passage. Burning of such a mixture accelerates the velocity of pressure rise in the main chamber. Therefore, at a large area of the passage, pressure rises in the higher rate in the main chamber than in the swirl chamber.

(4) Pressure oscillations observed in the combustion chambers can be assorted into three modes; i.e., the normal modes of transverse vibration in the swirl chamber as well as in the main chamber, and the mode of vibration as a resonator of combined cavities. The last is remarkable when the area of the passage is large and the others increase in force when the area is small.

Concerning influences of spray direction and the wall temperature :

(5) With injections done from the center of the sphere to the periphery in downstream of an swirl, ignition delay concerns closely with the wall temperature. Ignition starts from a middle part of the chamber at a low wall temperature, and from the vicinity of the wall when the wall is hot.

(6) The lower the wall temperature, the higher becomes the maximum rate of pressure rise in the swirl chamber when fuel spray is directed at the center. In the peripheral injection, however, the lowering of the wall temperature does not produce the increase in the pressure rate despite of a long ignition delay.

(7) The duration of combustion lasts long at each of the following cases; when fuel particles are much gathered in the middle part of the chamber, when the ignition delay is short, and when the fuel is much adhered to the wall.

(8) When the fuel is injected onto the wall, several interesting features can be observed in combustion; low combustion noise over the entire range of wall temperature, blue flame burning, ignition from many positions, and abnormally short ignition delay.

# CHAPTER 5

## Idling Knock in Pre-Chamber Type Diesel Engines

### 5.1 Purpose of the Study

With a pre-chamber type diesel engine, a peculiar combustion noise often experienced at a low speed running under no load or a light load is called "idling knock", which is considered to be different from conventional diesel knock. According to the work of Nagao and others[17], its immediate cause is rapid pressure rise in the main chamber, which can be controlled by the following methods; reducing the rate of fuel injection during an ignition delay period, preventing fuel spray from escaping into the main chamber and reducing the ignition delay of fuel existing in the main chamber. As regards its origin, however, many points still remain unexplained, some of which are as follows:

(1) Idling knock usually occurs within a limit of a lower engine speed. At the same time, its intensity is very sensitive to the temperature of coolant, kind of injection nozzle, opening pressure of the nozzle and others.

(2) Among the engines having various types of combustion chamber, inclination to idling knock is utmost with the pre-chamber engine.

In the first half of the present study, the range of idling knock pertaining mainly to the above-mentioned item (1) is investigated, paying attention to relation between injection rate (rate of discharge of fuel) and engine speed. Following this, elimination of idling knock is undertaken by means of inlet throttling. According to a research into promotion of cold starting[28], a certain temperature rise occurs in air in cylinder at the end of suction stroke when the inlet port is properly throttled. The latter half of this chapter reports the effectiveness and limitation of this method when it is applied to elimination of idling knock.

### 5.2 Idling Knock and Transition of Injection Mode

1) Correlation between idling knock and injection rate

Experimental apparatus A water-cooled four-cycle single cylinder engine with a pre-chamber was employed in the test. Data of the engine were as follows: Cylinder diameter and stroke were 95 mm and 115 mm

Fig. 5.1 Device of measuring needle lift




| No. of diagram | Opening pressure kg/cm² | Revolutions per minute |
|---|---|---|
| 1 | 105 | 602 |
| 2 | " | 650 |
| 3 | " | 1 000 |
| 4 | " | 1 300 |
| 5 | 125 | 634 |
| 6 | " | 800 |

Fig. 5.2 Typical recorded diagrams of cylinder pressure $p_x$ and needle lift h

respectively, compression ratio 19.0, nominal output 7 PS at 1400 rpm, volume of pre-chamber 31% of the total compression space and area ratio of the connecting passage to piston surface 0.52%. The injection pump was Bosch PE1A type with a plunger of 7 mm diameter in its ordinary arrangement (PE1A70B); inner diameter of feed line to the injector 1.6 mm, its total length 0.736 m, injection nozzle pintle type DN4S1 and spring modulus of the needle valve 17.9 kg/mm. The fuel employed was heavy oil "A", whose specific gravity and cetane number was 0.845 and 45 respectively.

For the purpose of the present study, a needle-lift pick-up was specially made as is illustrated in Fig. 5.1: A magnetic coil is set up in the inner space of the injector spring, so that a change may be detected in its self-inductance caused by a movement of a magnetic core that is mounted on the terminal of the spring. The magnetic core is so small that the weight of the injector-needle assembly does not increase largely. A shank that supports the detecting coil has a micrometer screw which is serviceable to static calibration of the needle lift as well as to fine adjustment of coil setting. On an AC-bridge which consisted of the magnetic coil, a 200 kc/sec-alternative current was applied, whose unbalance current was amplified by about 40 dB through a vacuum tube circuit including a tuner and rectified by transistor diodes. All recordings were made on a dual-beam cathode-ray oscillograph.

Test results The cylinder pressure and the needle lift of the nozzle were simultaneously measured at various engine speeds with a constant rack position of the pump. In Fig. 5.2 their typical records are shown. The fuel quantity was 29 $mm^3$ per firing stroke at the engine speed of 800 rpm, at which the brake mean effective pressure was 2.5 $kg/cm^2$. Although this was not exactly an idling condition, knocking was most remarkable under this condition and cycle-to-cycle variation of knock intensity could be minimized. It can be observed from Cards 1 and 2 that at 600 rpm the cylinder pressure rises so rapidly that it causes an idling knock of rather hard intensity, while a very smooth rise of pressure occurs at 650 rpm. In the needle lift curves, an evident difference can be seen between these adjacent speeds: In Card 1 the needle swings only once, thus accumulating fuel at a higher rate in the combustion chamber among the intitial stages of injection, whilst in Card 2 a small charge is introduced prior to the main part of injec-

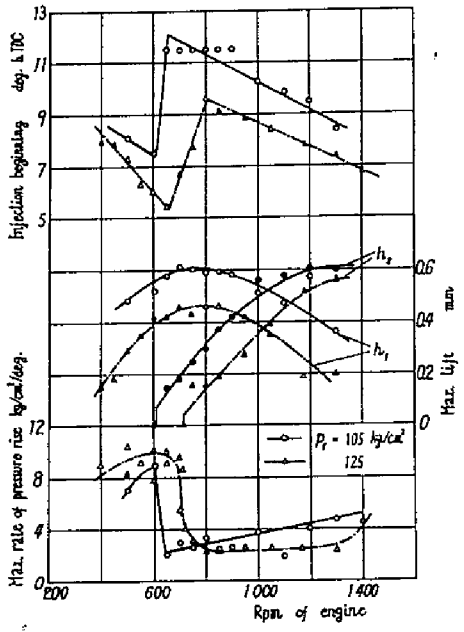


Fig. 5.5 Maximum rate of pressure rise at varying engine speed, together with injection timing and maximum lifts at the earliest and the subsequent stages $h_1$ and $h_2$ respectively

tion. The initial small skip grows to such an extent that its relative magnitude is counterbalanced with the later stages of needle lift at 1000 rpm, as shown in Card 3. Finally at 1300 rpm, the earlier stages of injection become greater than the later stages, losing smoothness of pressure-time curve as can be seen from Card 4. In Fig. 5.3 are shown the maximum rates of pressure rise in cylinder together with the measured values of injection timings and maximum lifts of injection nozzle, for the cases of 105 $kg/cm^2$ and 125 $kg/cm^2$ of opening pressure. From this the following facts are known:

(1) The enigne speed at which the first skip just appears depends on the opening pressure of the injection nozzle. For convenience sake such a speed will be called the "transition speed" hereafter. For the two kinds of opening pressures, this speed was accurately determined by observing patterns of needle lift drawn on a cathode-ray tube. According to the experimental results, the transition speeds were from 612 to 614 rpm for 105 $kg/cm^2$ and from 710 to 720 rpm for 125 $kg/cm^2$. Apropos of these, Cards 5 and 6 are the oscillograms taken at speeds adjacent to the transition speed at 125 $kg/cm^2$ of opening pressure.

(2) When the engine speed is higher than the transition speed, the earlier stages of the needle motion grow larger with speed, whilst the later stages diminish with it.

(3) The maximum rate of pressure rise is very low at higher than the transition speed. In other words, the transition speed prescribes the upper limit of idling knock.

(4) Above the transition speed, the maximum rate of pressure rise makes a slow ascent with the engine speed, attaining 4 $kg/cm^2$ at about 1100 rpm and 1400 rpm for opening pressures of 105 $kg/cm^2$ and 125 $kg/cm^2$ respectively, at which an audible knock regains. Thus the engine runs very quietly in the range between the transition speed and this speed. In such a range, the injection rate in the initial stages is so favorable, just like "pilot injection"[2], that it produces a low rate of pressure rise in the cylinder.

Summarizing the foregoing, the fact that the idling knock occurs at less than a certain speed closely relates difference in injection mode. This phenomenon has recently been pointed out also by Alcock and Scott[29], who call such a two-stage injection the "unintentional pilot injection."

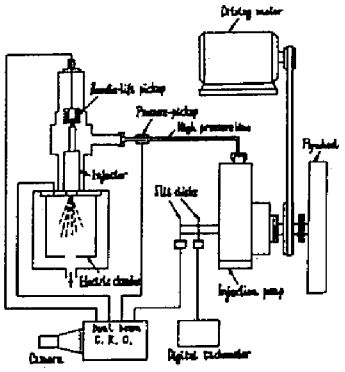


Fig. 5.4 Scheme of experimental apparatus

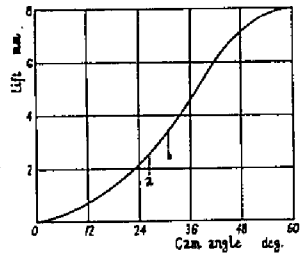


a and b indicate spill-valve closing of pumps mounted on the test bench and on the engine respectively.

Fig. 5.5 Cam lift curve of test pumps

2) Two-stage injection and transition speed

The two-stage injection accompanying a small pre-injection, chiefly that of injection system of marine diesels, has been treated both theoretically and experimentally by Kushiyama.[30] In the present study, the transition speed which prescribed the disappearance of idling knock was experimentally investigated. For this purpose, the injection system was individually equipped on a test bench as is shown schematically in Fig. 5.4. Fig. 5.5 shows the curve of cam lift against cam angle of the pump employed. In the present case, injection was done at atmospheric pressure as a matter of convenience. In order to evaluate the effect of ambient pressure, transition speeds were measured for three different conditions; the first case was of the operating engine, the

Table 5.1 Comparison of transition speeds in rpm

| Opening pressure of the nozzle $p_1$ | | 105 kg/cm$^2$ | 125 kg/cm$^2$ |
|---|---|---|---|
| With the operating engine ($2\,n_k'$) | | 612 ~ 614 | 710~720 |
| With the engine at atmospheric injection ($2\,n_k$) | | 698 ~ 699 | 790~796 |
| At the test bench (twice the pump rpm) | | 692 ~ 700 | 800~816 |
| $n_k'/n_k$ | Experimental (Average value) | 0.878 | 0.896 |
| | Theoretical | 0.816~0.889 | 0.847~0.910 |

second of atmospheric condition with the injector mounted on the test engine and the last of atmospheric injection at the bench. The test results are summarized in Table 5.1. It is observed from this that the transition speed at atmospheric injection is higher than that of operating engine by from 70 to 90 rpm.

In the following experiment, the approximate course of injection rate was picked up by electric-charge method which had been developed by Schacke and Straubel[31]. The foundation of this method is that, when particles of fuel spray are caught with an electrically insulated chamber, an electric charge induced is approximately proportional to

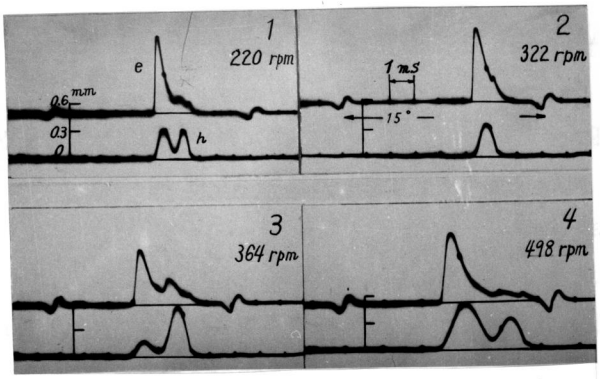


Fig. 5.6 Correlation between electric current e and needle lift h (opening pressure $p_1$= 105 kg/cm²)

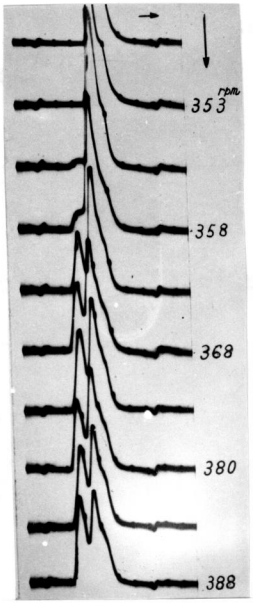


Fig. 5.7 Transition occurred in the course of acceleration of pump

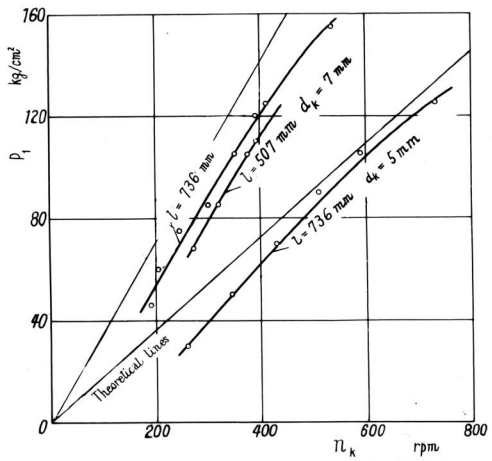


Fig. 5.8 Effect of opening pressure $p_1$ on transition speed $n_k$

the quantity of injection for a constant opening pressure of the injector. If this charge is discharged through a low resistor, its current indicates approximately the instantaneous rate of injection. In Fig. 5.6 are shown the simultaneous records of needle movement and the current, for several kinds of pump speeds. From them it may be possible to conclude that measurement of this current will serve in obtaining the relative timing of injection as well as in discriminating whether injection is of single stage or two-stage. With this method, then, the entire lot of injection-rate versus time relations were recorded during the acceleration of pump, in order to observe the phenomenon of transition from single-stage mode to two-stage mode. The successive recording was made so that every cathode ray image might be photographed on a streak camera by feeding a nagative film in the right angle to the direction of beam sweeping. Fig. 5.7 reproduces some portions of the records. It can be proved from this that the transition of injection mode suddenly occurs at a certain speed and that the earlier swing of the needle gets larger as the pump speed increases after the transition. However, in these cases the transition did not occur so stably and the transition speed often fluctuated among a small range. Moreover, at the transition rpm, repetition from mode of single-stage injection to that of two-stage injection was experienced in the course of experiment.

The influence of the opening pressure $p_1$ on the average pump speed of transition speed $n_k$ is illustrated in Fig. 5.8, in which are shown the cases of different pipe lengths ($l$=0.736 m and 0.507 m) and different diameters of pump plunger ($d_k$=7 mm and 5 mm). It can be seen from these results that $n_k$ increases monotonously with the opening pressure $p_1$. Furthermore, the transition speed seems to depend largely on the diameter of the plunger, but less on the length of high pressure line. It may be suggested from these facts that the state of pressure rise in the injection nozzle has a close connection with the phenomenon of transition of injection mode. In order to reach the essential recognition of the phenomenon, pressure development in the pipe line was measured at a section near the nozzle holder, by using a strain-gage type pick-up. Fig. 5.9 shows its typical records together with those of electric current induced by injection. Firstly, it can be seen from Card 1 that, at 334 rpm, the injector does not open with the initial pressure rise but lifts with the second pressure rise. Contrariwise, at 354 rpm,

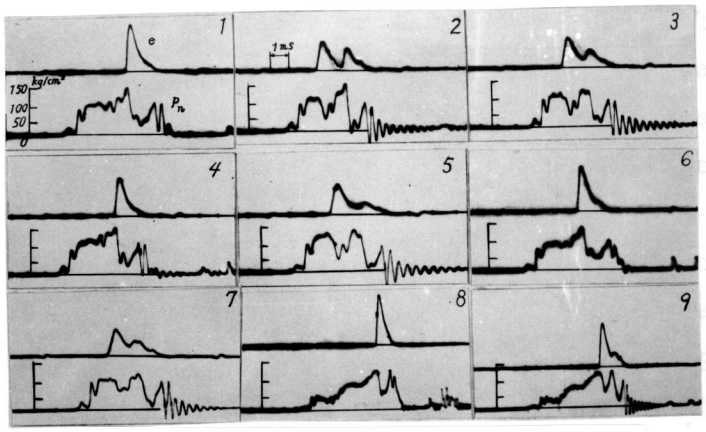


| No. | Dia. of plunger mm | Opening pressure kg/cm² | Rpm of pump |
|---|---|---|---|
| 1 | 7 | 105 | 334 |
| 2 | " | " | 354 |
| 3 | " | " | 490 |
| 4 | " | 125 | 386 |
| 5 | " | " | 404 |
| 6 | 5 | 105 | 550 |
| 7 | " | " | 610 |
| 8 | 7 | 105 | 144 |
| 9 | " ($l$=0.507 m) | " | 144 |

$l$= 0.736 m excluding No. 9

Fig. 5.9 Pressure change in the pipe at nozzle side $p_n$

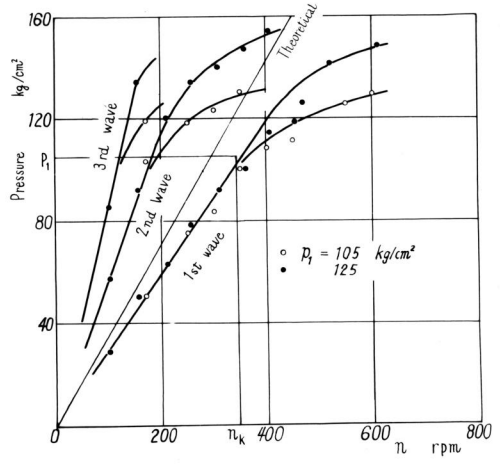


Fig. 5.10 Influence of pump speed on heights of pressure waves

injection starts with the earlier pressure rise as seen from Card 2, but, it does not rise to power until the arrival of the next pressure wave, owing to a sharp pressure drop during the period of application of first pressure rise. The difference in phase of injection-initiation between cases of 334 rpm and 354 rpm amounts to $3.1^{\circ}$ in angle of pump shaft, which corresponds to about 1.5 msec, at 334 rpm. As seen from Card 3, an increase in the pump speed above $n_k$ does not produce any essential variation in the pressure-time relations. Further, with the different opening pressure of the injector and the different diameter of the pump plunger, the trends in the pressure change around the transition speed do not show any great deviation from what was mentioned above, as observed from Cards 4 and 5 as well as from Cards 6 and 7. Finally, Fig. 5.10 shows measured values of the three pressure steps from the first till the third against the voluntary revolutions per minute in the cases of 105 $kg/cm^2$ and 125 $kg/cm^2$ of opening pressures for 7 mm of plunger diameter. Clearly this figure shows that the two-stage mode occurs only when the pressure rise of the first wave exceeds the opening pressure of the injector. Seeing from the figure, other types of injection advancement can take place; that is, transition from the first wave to the second wave, that from the second to the third, and so on. In fact these transitions could be experienced at low speeds with the operating engine. Cards 8 and 9 in Fig. 5.9 show the step-wise pressure changes at a speed low enough to open the nozzle with the third pressure wave.

3) Considerations on transition speed and knocking condition

Theoretical consideration on the transition speed Summarizing the results mentioned above, pressure wave initiated at the fuel pump is so weak at a low speed that the nozzle does not spray any fuel until the second or later wave arrives, thus resulting in a relatively high rate of discharge in the initial stages of injection. The amplitude of the first pressure wave, which increases with the pump speed, becomes sufficient to inject fuel at the transition speed. When the pump speed is not so high as this, the nozzle does not open wider until arrival of a new pressure wave, thereby the injection done in two steps. Finally, at a very high speed, the first wave is so powerful that the initial injection rate becomes high again.

As can be supposed, the transition speed may be governed by many factors of the injection system; namely, length of pressure pipe, design of nozzle and delivery valve, influence of residual pressure or void, influence of self-excited vibration occurring in nozzle, and so on. Since it is probably very difficult to take all of them into consideration in arriving at a theoretical solution, we now pay attention to relation between pressure wave and opening pressure only: Thus we consider a simplified injection system in which a plunger of diameter $d_k$ moves at a constant speed $w_k$ expelling fuel in a pipe of uniform inner diameter $d_l$ and length $l$. If compressibility of fuel inside the pump is neglected, then the amplitude of compression wave $\Delta p$, when the fluid inside the pipe suddenly gets a velocity from the state of repose, is given by

$$\Delta p = \frac{a\gamma}{g} w_k \left(\frac{d_k}{d_l}\right)^2 \tag{5.1}$$

where $\gamma$ denotes the specific gravity of fuel, $a$ the sound velocity and $g$ the acceleration due to gravity. Introducing geometric speed $r$, that is, cam lift per degree of cam angle, we have

$$w_k = 6 n_p r \tag{5.2}$$

where $n_p$ denotes pump speed in rpm. Neglecting the terminal spaces of the pressure pipe and motion of needle and assuming that a pressure rise produced at the nozzle $2\Delta p$ is equal to the opening pressure $p_1$ at the transition speed $n_k$, we can describe this speed from Eqs. (5.1) and (5.2) as follows:

$$n_k = \frac{p_1 g}{12 a r \gamma} \left(\frac{d_l}{d_k}\right)^2 \tag{5.3}$$

In Fig. 5.8 are described the theoretical speeds of transition against the opening pressure thus gained from Eq. (5.3), in which the following numerical values were used: r=0.183 mm/deg from Fig. 5.5, $\gamma$= 845 kg/cm$^3$ and $d_l$ = 1.6 mm. The sound velocity was given to be 984 m/s, from measurement of time interval of travelling pressure signal in the pipe line by using two pressure transducers. It is noted from the figure that the transition speed predicted theoretically always gives a lower value than that of the experimental one. On this point, the same theoretical line is described in Fig. 5. 10, the diagram of height of pressure wave versus pump speed. It may be said from this that the transition speeds can be more accurately predicted once a more accurate pressure development

is given by taking account of the factors described ealier.

When cylinder pressure is applied to the injection nozzle, the transition speed is justly lower than that of atmospheric injection, because the nozzle under application of the cylinder pressure can unlock at less than the opening pressure. At a constant opening pressure, the ratio of the transition speed of pump $n_k'$ when the engine is equipped with the nozzle, to the corresponding speed at atmospheric injection $n_k$ is given by

$$\frac{n_k'}{n_k} = 1 - \frac{p_c - p_o}{p_1} \cdot \frac{1}{f_n/f_s - 1} \tag{5.4}$$

where $p_c$ denotes cylinder pressure, $p_o$ atmospheric pressure, $f_n$ sectional area of the needle and $f_s$ the sectional area of valve seat to which cylinder pressure acts. Experimental value of $n'_k/n_k$ is presented in Table 5.1 in contrast with the theoretical ones calculated by Eq. (5.4) in which $p_c$ is assumed to be 35 kg/cm$^2$ and $f_s$ either the outer or the inner area of the seat. As the experimental value lies between the theoretical ones, the above matter proved to be correct.

Condition of idling knock Indeed the speed range of idling knock is determined by the generation of a small portion of fuel sprayed prior to the main part of the charge, but the condition of occurring knock would also depend on the mixture formation and combustion in the combustion chamber, namely, rate of mixture formation, distribution and transfer of the mixture and so on. The fact that the idling knock is most marked with a pre-chamber type engine as has already been mentioned in Section 5.1, may probably be understood by taking these factors into consideration. In Fig. 4.5 in Chapter 4, which is suggestive of this point, the noise characteristics of a swirl chamber type engine were presented for various area ratios of the connecting passage to the piston surface f/F. At an engine speed not distant from the nominal speed of the testing engine, the best performance was gained at an area ratio of the connecting passage between 1% and 2%. With this area ratio, the noise level at a higher speed is relatively high while it is low at a lower speed, as seen from the figure. With a smaller area ratio less than 0.75%, which seems to be unusual in the ordinary swirl chamber type engine, the combustion noise is very pronounced at a low speed, showing a typical feature of idling knock. Consequently, the idling knock of the pre-chamber engine would also be closely concerned with its small area ratio of the connecting

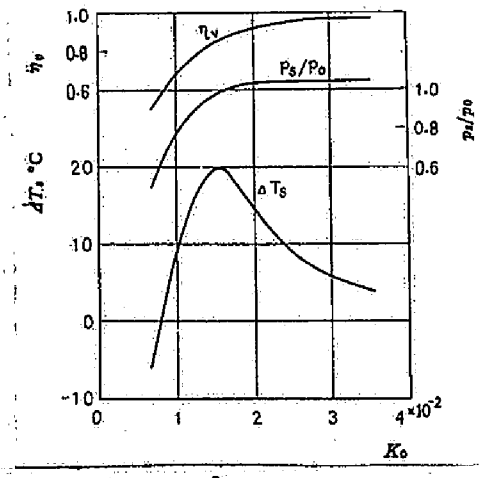


$k = 1.40$, $T_o = 300°K$, and $\mu = 0.65$

$P_o$ denotes atmospheric pressure.

Fig. 5.11 Theoretical temperature rise and pressure in cylinder at the end of suction stroke

passage. It may safely be said that in a pre-chamber type engine a strong air motion created in the pre-chamber by an incoming stream due to a narrow connecting passage assists a rapid formation of a combustible mixture from the fuel injected at a high rate of injection in the initiation, thereby bringing with it a strong idling knock at a low engine speed.

## 5.3 Elimination of Idling Knock by Means of Inlet Thottling

### 1) Predicted temperature rise

For a given rate of fuel injection, it is necessary to shorten the ignition delay in eliminating the idling knock. Among several possible means, inlet throttling is taken up here as a new practical one. Generally speaking, a throttled suction will given a longer ignition delay and this principle has been used for measuring cetane numbers of diesel fuels[32]. According to Nagao, Kakimoto and others, however, a certain temperature rise can occur in air in cylinder at the end of suction stroke if the volume between the throttle and the suction valve is small;[28] an increase in the work done by the inlet throttling during the suction stroke is converted into an increase in the internal energy of the air charged. This process was formulated with a four-cycle engine under appropriate assumptions, and the differential equations obtained were numerically integrated with several kinds of throttle ratios finally to know the pressure and temperature of the charge. In their calculation the following assumptions were made: The ideal gas law and the adiabatic law hold. Kinetic energy of gas behind the throttle is immediately converted into heat raising the charge temperature uniformly. And no heat exchange is present between the cylinder wall and the charge.

The case calculated was that of constant compression ratio $\varepsilon_0$ which was defined as follows:

$$\varepsilon_0 = \frac{V_s + V_c + V_{throttle}}{V_c + V_{throttle}} = 6.15$$

where $V_s$ denotes stroke volume, $V_c$ clearance volume and $V_{throttle}$ space between the suction valve and the throttle arranged. Further, the ratio of crank radius to the length of the connecting rod was 1/4. The results of calculation are summarized in Fig. 5.11, in which the temperature rise and the pressure of the charge at the end of the suction stroke, and the

volumetric efficiency, denoted as $\Delta T_s$, $p_s$ and $\eta_v$ respectively, are presented. $K_o$ in the abscissa is a parameter characteristic of the throttle area, which may be designated as throttle ratio, defined as follows;

$$K_o = \frac{\sqrt{2\kappa}\ \mu f\ \sqrt{kgRT_o}}{6n\,FS} \tag{5.5}$$

where, f: throttle area, $\mu$: flow coefficient of the throttle, F: surface area of piston, S: stroke, n: engine speed in rpm, $\kappa$: ratio of specific heats for air, $g$: acceleration due to gravity, R: gas constant for air, $T_o$: atmospheric temperature, $\sqrt{kgRT_o}$ : sound velocity in the atmosphere.

It can be seen from the figure that the maximum temperature of the charge is obtained at $K_o=1.63\times10^{-2}$ and that the charge temperature increases by 20°C above the atmospheric temperature at that ratio.

Denoting the temperature rise and pressure drop from the atmosphere at the end of suction stroke as $\Delta T_s$ and $\Delta p_s$ respectively, the resulting temperature rise at the end of compression stroke $\Delta T_c$ and the corresponding pressure drop $\Delta p_c$ are

$$\Delta T_c = \Delta T_s \cdot \varepsilon^{n-1}\ ,\quad \Delta P_c = \Delta P_s \cdot \varepsilon^{m} \tag{5.6}$$

where $\varepsilon$ denotes the real compression ratio of the engine and m the exponent of polytropic change during the compression stroke. For example, if $\varepsilon=19.0$ and m=1.33, then $\Delta T_c/\Delta T_s=2.64$ and $\Delta p_c/\Delta p_s=50.0$. As $\Delta T_s=20°C$ and $\Delta p_s=0.015$ kg/cm$^2$ with the optimum throttle ratio, we can expect $\Delta T_c=53°C$ accompanied with a pressure drop only by $\Delta p_c=0.75$ kg/cm$^2$. Such a temperature rise with a very small pressure drop will contribute to shorten the ignition delay of fuel reducing the combustion noise by a certain degree.

2) Virture of inlet throttling

Apparatus and procedure The numerical values presented above are able to actualize at the engine which was used in the experiment of the previous section. So the same testing engine was employed in the present test, in which no valve-overlap was arranged so that the exhaust gas might not re-enter into cylinder by negative pressure due to the inlet throttling. Injection nozzle was throttle type DN4SD24 and its opening pressure adjusted so as to be 100 kg/cm$^2$. Other conditions were the same

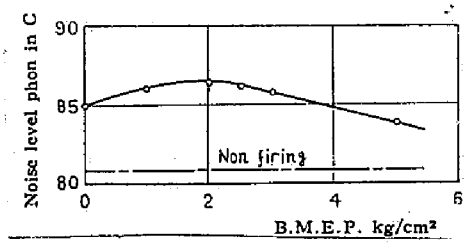


(a) Influence of load at constant engine speed of 600 rpm

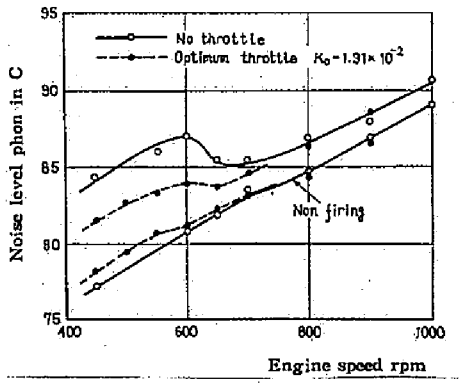


(b) Influence of speed at constant Bmep of 2.0 kg/cm²

Coolant temperature is 60°C at exit and fuel injection timing 4° before TDC.

Fig. 5.12 Influences of engine speed and load on median noise level

as before.

The engine noise was measured by a noise level meter ( Japan Electronic Instrument Co., SL-7B type), whose microphone was placed opposite the flywheel at a distance of 50 cm from the engine cover. The test procedure was in accordancewith JIS (Japanese Industrial Standards) Z8731 "Method of Sound Level Measurement". In order to employ the meter for determing the noise intensity of such repeated blows as the idling knock, the rapidly changing noise level was averaged by using a low-band-pass filter (time constant: 2 seconds) for its indication. The fired noise level was always observed in relation to the non-fired level. Because of cyclic irregularity in combustion, a statistical treatment was necessary to obtain reliable sets of data; the median of twenty five or fifty readings of every five seconds were assumed to be a measure of the engine-noise level. In addition, all levels were read of the C-scale in JIS, that is, the case without auditory correction.

Idling knock to be prevented First of all, preliminary tests were made to find out the test condition under which the availability of the inlet throttling would be examined. As their results, Fig. 5.12 portrays the influences of load and speed on the median noise level without a throttle at the inlet. As is shown in Fig.5.12 (a), when the load is varied with a constant speed of 600 rpm, maximum noise is heard at 2 kg/$cm^2$ of Bmep. In the meanwhile, if the engine speed is changed at a constant load of 2.0 kg/$cm^2$, the noise intensity increases with the engine speed as is shown in Fig. 5.12(b), holding 2 phon rise above the motored level at higher speed than 700 rpm and about 6 phon increase at higher than 600 rpm. A discontinuity is seen in the curve between 600 rpm and 700 rpm. And at about 600 rpm, a maximum intensity of the noise is given, showing a characteristic feature of idling knock.

In addition, at 600 rpm and 2.0 kg/$cm^2$ of Bmep, injection timing was chosen so as to be 4 degrees before TDC, and continuous advancement of the injection gave an increase in the noise level and in the specific fuel consumption. The effect of the inlet throttling was thus examined under the following test condition;

| | |
|---|---|
| Engine speed: | 600 rpm |
| Brake mean effective pressure: | 2.0 kg/cm2 |
| Injection timing: | $4.0^{\circ}$ before TDC |

An increase in the mechanical loss due to the throttling can theoretically

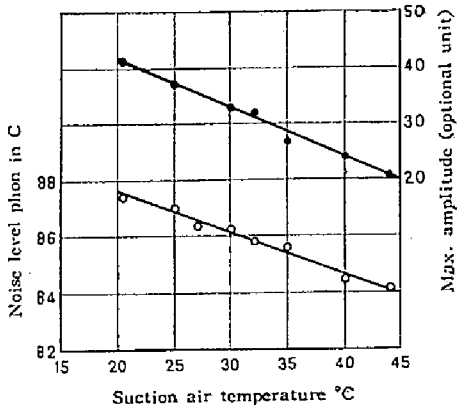


Room temperature is 20.5°C, engine speed 600rpm, Bmep 2.0 kg/cm² and coolant temperature 60°C.

Fig. 5.13 Reduction in noise level at pre-heated suction in the case without throttle

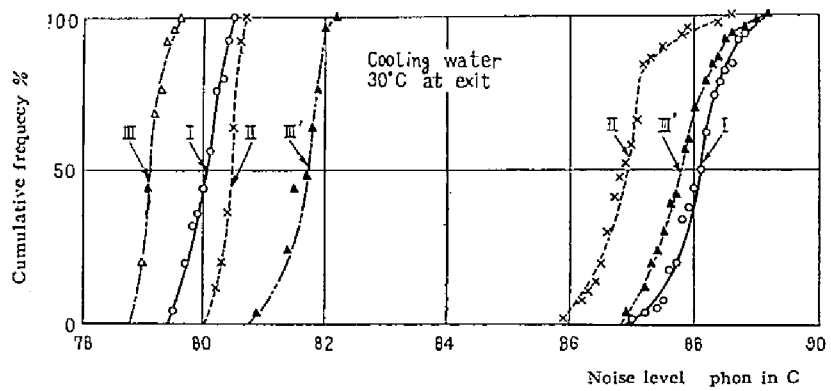


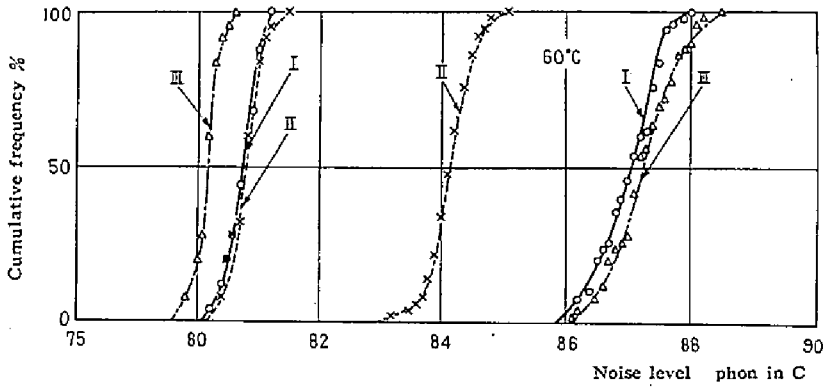


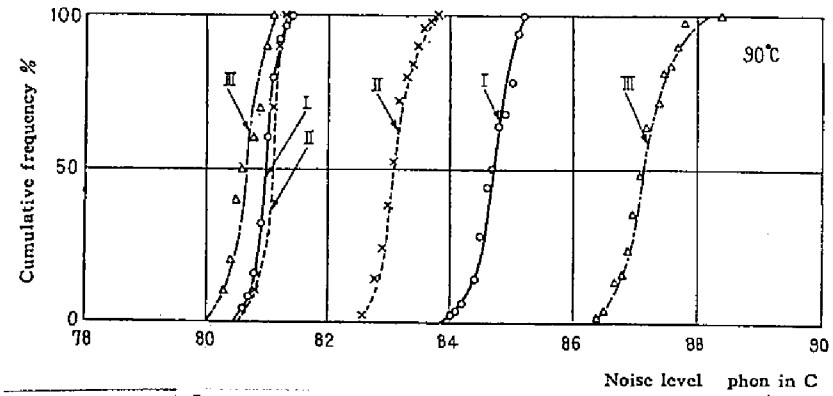


I: no throttle applied

II: optimum throttling at $K_o = 1.31 \cdot 10^{-2}$

III: excessive throttling at $K_o = 0.59 \cdot 10^{-2}$

III': excessive throttling at $K_o = 0.92 \cdot 10^{-2}$ (peculiar to the case of 30°C of coolant temperature)

Speed and load are 600 rpm and 2.0 kg/cm².

Fig. 5.14 Cumulative frequency distributions of noise levels

be as high as 0.27 kg/cm$^2$ in Bmep, at $K_o$=1.6x10$^{-2}$, by which no great influence would be done on the noise level, as is recognized from Fig.5.12 (a).

Another preliminary experiment was carried out to know the relationship between the pre-heated suction and the noise. In Fig. 5.13 test results with variable suction-air temperature are shown at a constant temperature of cooling water exit. It can be seen that the median noise level decreases largely with the suction-air temperature and that the level reduction by 3.0 phon can be expected by about 20°C of temperature rise in the suction air.

Reduction of combustion noise The noise level was measured with the fired and the non-fired runnings at three kinds of typical inlet ports; namely, (I) one with no throttle applied, (II) one with the optimum throttling which had experimentally been obtained at $K_o$=1.31x10$^{-2}$, and (III) one with excessive throttling when $K_o$=0.59x10$^{-2}$. The engine was operated under these conditions with three different cooling-water temperatures of 30°C, 60°C and 90°C respectively at the exit.

In Fig. 5.14,distributions of cumulative frequency of the noise level are presented and in Table 5.2 several quantities measured from the curves are summarized; they are median noise level, mode, 90%-range, level increase above the non-fired level, and reduction from the non-throttled condition. Of these, the 90%-range signifies a magnitude of fluctuation in the noise level, being defined as the level width in which the measured levels from 5% to 95% of frequency are involved.

From these the followings are deduced:

(1) For every temperature of cooling water at exit, some degrees of noise level reduction from the non-throttled condition are materialized in the case of the optimum throttle condition (II); that is, 1.3 phon at 30°C and 1.9 phon at 90°C. Remarkable reduction by 2.9 phon at 60°C corresponds with the theoretical temperature rise of $T_s$=20°C in Fig. 5.13.

(2) Higher noise level from 87 to 88 phon is unavoidable with the excessive throttling (III) irrespective of the cooling water temperature. At 30°C of cooling water, the engine misfires in the case of $K_o$=0.59x10$^{-2}$, so that the case of $K_o$=0.92x10$^{-2}$ is shown in the figure and the table.

(3) Non-fired level depends considerably on the inlet condition. This is due to the difference in suction noise. The decrease of the non-fired level under the condition III from the corresponding level under the condition I amounts to 0.3 to 0.9 phon.

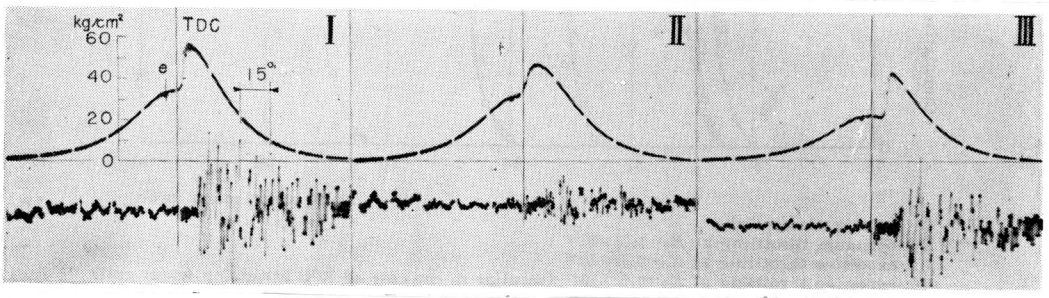


Same conditions as in Fig. 5.14 but coolant is 60°C

Fig. 5.15 Oscillograms of pressure in the main chamber and body noise

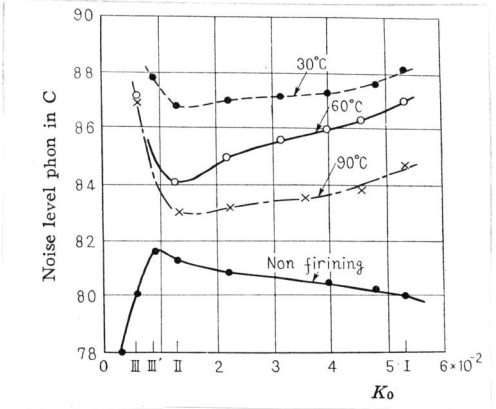


Fig. 5.16 Median noise level at varying throttle ratio $K_o$

Table 5.2 unit: phon in C-scale

| Throttle condition | Cooling water temperature at exit | Fired Median | Fired Mode | Fired 90%-range | Non-Fired Median | Non-Fired Mode | Non-Fired 90%-range | Increase above non-fired level* | Reduction from no throttled level* |
|---|---|---|---|---|---|---|---|---|---|
| I | | 88.1 | 88.0 | 1.6 | 80.0 | 79.9 | 0.9 | 8.1 | |
| II | | 86.8 | 87.2 | 1.5 | 80.5 | 80.6 | 0.5 | 6.3 | 1.3 |
| III | 30°C | misfiring | | | 79.1 | 79.1 | 0.6 | - | - |
| III' | | 87.8 | 87.8 | 2.4 | 81.6 | 81.5 | 1.1 | 6.2 | 0.3 |
| I | | 87.0 | 87.4 | 1.6 | 80.8 | 80.9 | 0.9 | 6.2 | |
| II | 60°C | 84.1 | 84.2 | 1.1 | 80.8 | 80.8 | 0.9 | 3.3 | 2.9 |
| III | | 87.2 | 87.1 | 1.8 | 80.2 | 80.2 | 0.8 | 7.0 | -0.2 |
| I | | 84.7 | 84.6 | 1.1 | 80.9 | 81.0 | 0.5 | 3.8 | |
| II | 90°C | 83.1 | 83.2 | 0.8 | 80.9 | 81.0 | 0.5 | 2.2 | 1.6 |
| III | | 87.1 | 87.2 | 1.2 | 80.6 | 80.8 | 0.9 | 6.5 | -2.4 |

* for median

(4) Median and mode of the fired level virtually coincide with each other. The 90%-range stands between 0.8 and 1.5 phons in the case of optimum throttling.

In Fig. 5.15 typical records of cylinder pressure and body noise are illustrated in the case of 60°C of cooling water at exit. The optimum throttle (II) gives smoother cylinder pressure change and quieter running than with the open inlet condition (I), or with the excessive throttle (III).

Fig. 5.16 shows the effect of continuously varied throttle ratio, $K_o$, on the median noise level for the three different temperatures of cooting water, together with the noise level under non-fired condition. In order to describe any degree of throttling including the case where the effect of the inlet valve cannot be neglected, an equivalent throttle area $f_{eq}$ has been introduced in such a way that the resistances due to both the suction value and the throttle installed may be replaced by this fictitious orifice. Denoting the actual throttle area as f and the average valve passing area, obtained by dividing the total time-area of the inlet valve by the duration of its opening, as $f_v$, one can equate the flow rate through the equivalent orifice with those through the two resistances, and accordingly obtain

$$\mu f \sqrt{2g \frac{\Delta p}{\gamma_o}} = \mu_v f_v \sqrt{2g \frac{\Delta p_v}{\gamma_v}} = \mu f_{eq} \sqrt{2g \frac{\Delta p_{eq}}{\gamma_o}} ,$$

where, $\mu_v$: flow coefficient of suction valve, $\gamma_o$ and $\gamma_v$: specific gravities of atmospheric air and of air between the resistances, respectively, $\Delta p$ and $\Delta p_v$: pressure differences caused between spaces divided by the installed throttle and by the suction valve, respectively; $\Delta P_{eq}$ is the total pressure drop or the difference in both sides of the equivalent orifice; i.e.

$$\Delta p_{eq} = \Delta p + \Delta p_v .$$

Elimination of pressure differences from these equations leads to the following formula;

$$(\mu f_{eq})^{-2} = (\mu f)^{-2} + (\mu_v f_v)^{-2} \cdot \gamma_v / \gamma_o \qquad (5.7)$$

From the practical point of view, the modification of $K_o$ is significant only for a large value of throttle area, f, so that it would miss nothing to introduce the relations as $\gamma_v/\gamma_o = 1$ and $\mu = \mu_v$, in the course of the threatment. Thus the final formula for the modification is as follows:

$$f_{eq}^{-2} = f^{-2} + f_v^{-2} \qquad (5.8)$$

Modified $K_o$ will be obtained by applying $f_{eq}$ to Eq. (5.5) in place of f. Numerical values for calculating thus modified $K_o$ are derived from the specifications and the running conditions of the testing engine as follows:

$F=7.1 \times 10^{-2} m^2$, $S=0.115$ m, $f_v=4.94 \times 10^{-4} m^2$,

n=600 rpm, $T_o=300^{\circ}K$, $\mu=0.60$.

At non-throttled condition, where $f=10.18 \times 10^{-4} m^2$, one may find out that $f_{eq}=4.44 \times 10^{-4}$ and $K_o=5.28 \times 10^{-2}$.

Fig. 5.16 shows that, for every cooling water temperature, minimum noise can be heard at $K_o=1.3 \times 10^{-2}$ as is already presented as an optimum throttle ratio for noise. Although this ratio is somewhat smaller than the theoretical ratio expected as attainable maximum temperature-increase in suction air, the discrepancy between them seems still allowable as an error of flow coefficient of the throttle, $\mu$, estimated in the calculation of the ratio. Excessive throttling will give an increase in the noise level and finally produce a tendency to misfiring. The testing engine cannot be operated with smaller ratio than $K_o=0.84 \times 10^{-2}$ at $30^{\circ}C$

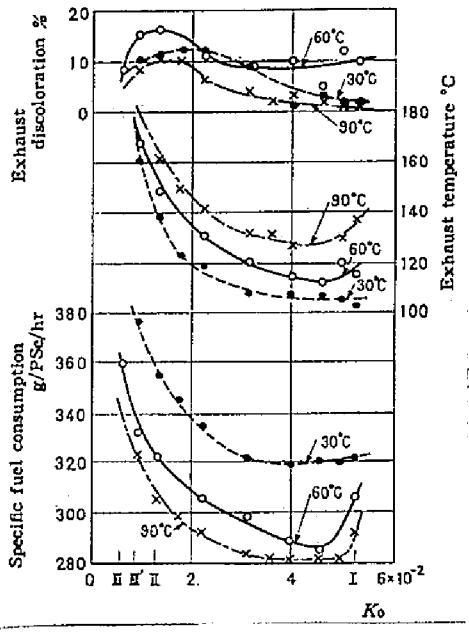


Fig. 5.17 Changes in engine performance due to throttling

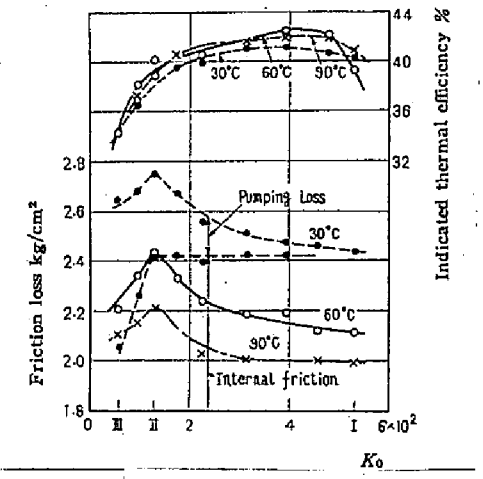


Fig. 5.18 Friction loss and indicated thermal efficiency

of the cooling water exit temperature. In the other cases, $K_o$= $0.51x10^{-2}$ at 60°C or $0.44x10^{-2}$ at 90°C respectively. There is a slight decrease in those ratios of giving misfiring with increasing water temperature of the exit. Below such critical ratios, a normal combustion does not take place, with accompanying a marked white exhaust.

All experiments mentioned above were made with a constant eingne speed of 600 rpm. Apart from this, measurement was made at various speeds with the optimum throttling at $K_o=1.3x10^{-2}$. The results are presented as broken lines in Fig.5.12. The noise is reduced as compared with the case without a throttle, amounting to 3.5 phon rise above the motoring level at most, which is clearly smaller than 6.0 phon in the case without a throttle. And, the peak of the curve at 600 rpm with the non-throttled condition has been successfully eliminated with the optimum throttling.

Changes in engine performance Fig. 5.17 is a summary of performance tests, showing measured specific fuel consumption, exhaust temperature and discoloration, in relation to the throttle ratio $K_o$ under the ordinary test condition of 600 rpm and 2.0 kg/cm$^2$ of Bmep. A little throttled range of the ratio from fully opened inlet, at $K_o=4\sim5x10^{-2}$, gives minimum values at the specific fuel consumption and at the exhaust temperature, at every exit-temperature of cooling water. Below this ratio, the changing throttle ratio causes a gradual increase toward but a rapid one near the extreme, in the fuel consumption as well as in the exhaust temperature. At the optimum inlet condition for the combustion noise (II), the increase in the specific consumption from the non-throttle is 14 g/PSe/hr corresponding to 4.2% rise.

In order to have a better insight into the change of the engine performance thus mentioned, the pumping loss and the total friction loss were measured with the testing engine; the former obtained through the calculation from the indicator diagrams, and the latter through the direct weighing by the electric dynamometer. These results are summarized in Fig. 5.18, from which one may know that smaller $K_o$ requires, in general, larger pumping loss, while the internal friction, that is, the rest of the total friction subtracted by the pumping loss, remains virtually constant down to the limit of $K_o=1.3x10^{-2}$. Below this limit, the internal friction and the total loss decrease quickly with the reduction of throttle ratio, in spite of the growth of the pumping loss, probably due to the drop of compression pressure. On the basis of the measured loss, the

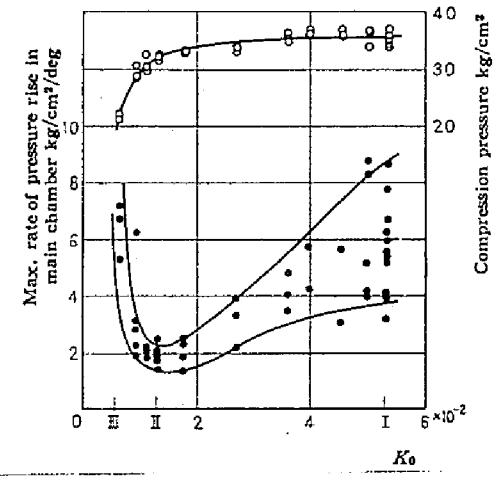


Fig. 5.19 Maximum rate of pressure rise and compression pressure in relation to $K_o$, at constant coolant temperature of 60°C

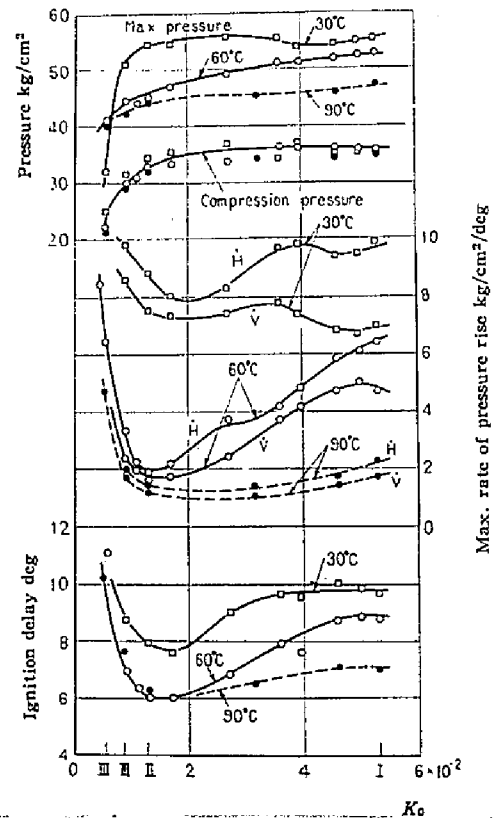


Ḣ denotes maximum rate of pressure rise in the main chamber and Ẇ that in the pre-chamber. Other values are of main chamber.

Fig. 5.20 Characteristics of combustion at varying throttle ratio $K_o$

indicated thermal efficiency has been calculated for 2.0 $kg/cm^2$ of Bmep and presented in relation to $K_o$ in the upper half of Fig. 5.18. It can be seen from this that the optimum throttle causes no great difference in the indicated thermal efficiency from that of no throttle, and that, for every cooling water temperature, the maximum efficiency can be found at a throttle ratio in the range between these inlet conditions. These seem due to a slight change in the combustion phase under those running conditions; namely, immutable compression pressure as well as so plentiful air for combustion as excess-air factor being above 2.5. On the other hand, excessive throttles bring about rapid falling down of the compression pressure and thus caused low excess-air factor, resulting in an imperfect combustion exhausting white smoke.

3) Consideration from indicator diagrams

The effect of the inlet throttling was evaluated by inquiring into indicator diagrams taken with various throttle ratios, in order to approach it from the standpoint of combustion.

The measured compression pressure and the maximum rate of pressure rise in the main combustion chamber are shown in Fig. 5.19, where each of the plots corresponds to an instantaneous combustion cycle sampled among successive ones. It can be seen from the figure that there are considerable cycle-to-cycle variations in the combustion in spite of a fixed running condition, which was difficult to catch by the use of the noise level meter. The maximum rate of pressure rise with the non-throttled inlet varies largely from 3 to 9 $kg/cm^2/deg$, while the optimum throttle cuts down the rates within narrower and lower range between 1.5 and 2.2 $kg/cm^2/deg$. For these, further analysis of indicator diagrams would be made by representing their variables in averaged values; ignition delays, maximum rates of pressure rise in the two chambers, compression pressures, and peak pressures are shown in relation to $K_o$ in Fig. 5.20.

First of all, the compression pressure is not influenced by the exit temperature of cooling water, and it decreases rapidly when the throttle ratio is reduced below $K_o=1x10^{-2}$. One can find out the minimum value in each of ignition delays at $K_o=1.3x10^{-2}$ and recognize that the shape of the curves is similar to those of sound level shown in Fig. 5.16.

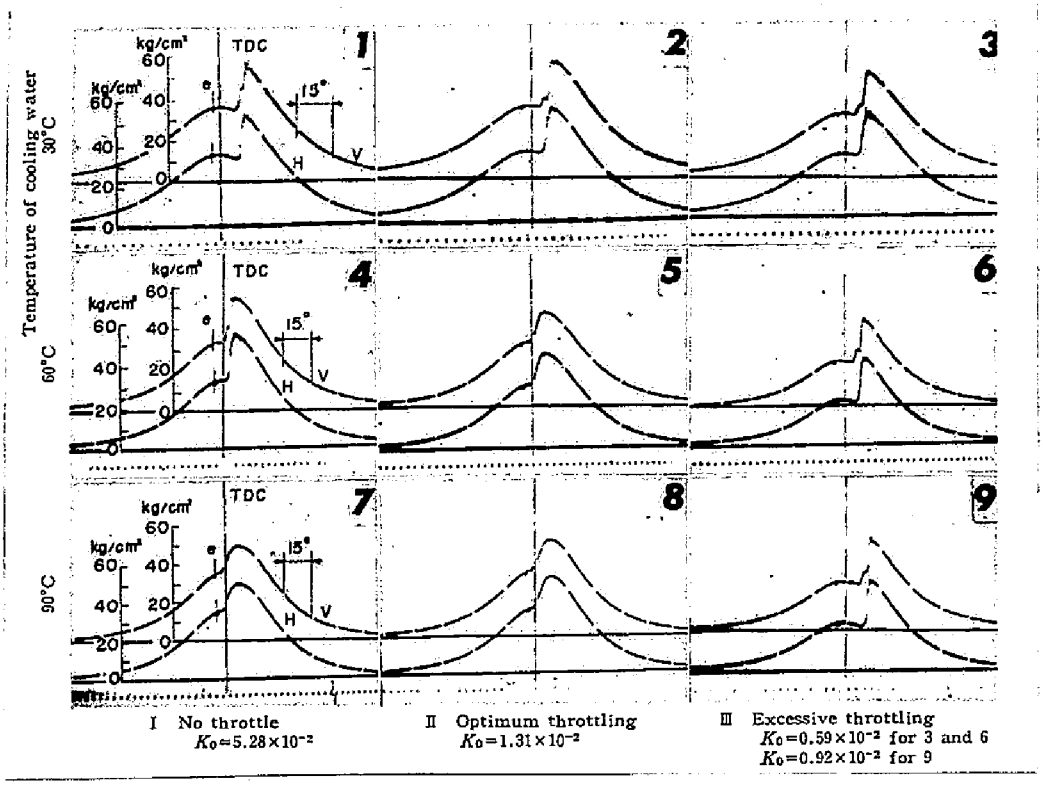


V: pressure in the pre-chamber, H: pressure in the main chamber, e: injection beginning, time mark: $10^{-3}$ sec

Fig. 5.21 Comparative indicator diagrams with typical inlet conditions and different cooling water temperatures

At the throttle ratio favourable for the noise reduction, the ignition delay is shortened by 2.2°, 2.8° and 0.9° in crank angle, for temperatures of the cooling water exit of 30°C, 60°C and 90°C respectively.

As regards the maximum rate of pressure rise, we may consider that a smooth running may be possible if the rate in the main combustion chamber is made below 2 kg/cm$^2$/deg. Applying this supposition to the cases considered, we may conclude that, at 60°C of the exit water temperature, knocking is absent with the optimum throttle ratio, because the rate is nearly 2 kg/cm$^2$/deg, while the open inlet causes furious knocking showing 5 to 6 kg/cm$^2$/deg. At 90°C of the exit temperature, the rate in the case of the open inlet is 2.2 kg/cm$^2$/deg, which almost corresponds to knocking-free running, and some slight additional advantage will be obtained with the optimum throttling. In the meanwhile, at 30°C of the exit water temperature, the reduction of the rate is from 10 kg/cm$^2$/deg at no throttle to 8 kg/cm$^2$/deg under the optimum condition but is short of knock suppression, for 8 kg/cm$^2$/deg is still in the severe knocking range.

Fig. 5.21 shows typical indicator diagrams illustrative of these conditions. Generally speaking, the phenomenon of idling knock is originated by a spontaneous combustion of combustible mixture in the main combustion chamber, that is, of unburned fuel come from the auxiliary chamber; hence, the intensity of the idling knock is predominantly governed by the amount of fuel entering into the main chamber[17]. Indicator Cards 1 and 2 illustrate this stage with strong knock occuring; namely, the initial ignition in the pre-chamber, a subsequent ignition in the main combustion chamber, and a very steep pressure rise in the main chamber which begins belatedly but soon exceeds the pressure in the pre-chamber. In the initial stages of the steep pressure increase, the rate in the main chamber is higher than that in the pre-chamber after some pressure rise has been developed. An abrupt rise begins in the pre-chamber due to an explosive combustion of the fuel left in the pre-chamber, and a sharply edged peak of pressure occurs after it. Thus longer ignition delay causes a bigger portion of unburned fuel to escape into the main chamber, giving a larger rate of the pressure rise.

Recognition of these facts will serve to clarify the effect of throttling in each case;

(1) In the case of 30°C of cooling water exit, ignition is delayed

by the low temperature wall of the combustion chamber and possibly starts when a few moments have elapsed after TDC, as is seen from the comparison of Card 1 with Card 2.

(2) In the case of 60°C of cooling water exit, a throttled suction causes a desirable shortening of the delay which affords simulteneous ignition in the pre- and the main combustion-chambers, eliminating the idling knock successfully, as is observed from Card 5.

(3) In the case of 90°C of cooling water exit, the ignition delay is substantially short even in the case of no throttle, so the effect of throttling appears minimum, as is seen from the comparison of Card 8 with Card 7.

(4) Eventually, excessive throttlings, as shown in Cards 3, 6 and 9, always give longer ignition delays, because of the reduced compression temperature and pressure, so that the pressure rise due to combustion starts much later than TDC, which leads to an exceedingly steep rise.

In the course of the experiment, the injection timing was so adjusted that the best engine performance might be obtained with 60°C of cooling water exit. If the timing is chosen to have minimum delay at each water temperature, some further advantage will be expected by the use of the inlet throttling.

## 5.4 Conclusion

From the research work on the idling knock and its elimination in pre-chamber type diesel engines, the following results were drawn out:

Concerning the idling knock and injection mode:

(1) That the idling knock occurs within a limited region of the engine speed relates the variation of the injection rate-time relation with the engine speed. At a lower speed the pressure wave initiated at the fuel pump is so weak that the nozzle can spray fuel by the second or later wave, thus resulting in a relatively high rate of discharge in the initial stages of injection, which invites an idling knock. At an engine speed at which the amplitude of the pressure wave becomes just sufficient to inject fuel with the first wave, the nozzle does not open wider yet at first, so that a small amount of fuel is injected prior to the substantial part, just like the pilot injection, thus bringing about a knock-free combustion. At a very high speed the first wave is so

powerful that the initial rate of injection becomes high again, regaining an audible knock.

Concerning elimination of idling knock by inlet throttling:

(2) An adequate throttling at inlet port can prevent the engine from the idling knock of a rather strong intensity. As the example, the maximum rate of pressure rise in the main chamber was reduced from 6.5kg/cm$^2$/deg down to 2.0 kg/cm$^2$/deg, at 60°C of exit of cooling water, which corresponded to a reduction of 3 phon in the noise level.

(3) The reduction of idling knock by the inlet throttling, however, is limited when the intensity of the knock is too high, since shortening of the ignition delay does not serve to prevent the combustibles from escaping into the main combustion chamber.

(4) Concerning the engine performance, minimum specific fuel comsumption is obtained at a throttle ratio, under a light load, and further throttling will cause an increase in the specific consumption. At the optimum throttling for knocking, the engine requires an increased consumption of fuel by about 4 % compared with no throttle condition. But the indicated thermal efficiency does not increase at the optimum throttling.

# CHAPTER 6

## An Analysis of the Rapid Pressure Rise in Diesel Engine

### 6.1 Purpose of the Study

The final problem that the author will refer to is the origin of rapid combustion occurring in the cylinder of a diesel engine. As has already been seen frequently, the rate of pressure rise is influenced by the rate of fuel injection, ignition delay, air swirl and so forth. It has been accepted that the rapidness of pressure rise has a close connection with quantity of the combustible mixture that concerns itself with the early stages of inflammation, namely the autoignition. Such a quantity of combustible mixture, however, cannot be measured directly and there is almost no theory by which we can predict the relationship between the ignition delay and the rate of pressure rise, excluding an empirical one presented by Austen and Lyn[33]. The strongest obstacle to theorize them is the fact that the physical processes, such as atomization, distribution, mixing and vaporization of the injected fuel, are intricately interwoven with the chemical processes involving the complex phenomena such as preflame reaction.

In order to reveal the essential nature of the rapid combustion, it will be of value to study each of the stated processes. At the same time, it seems equally important to find out the relation between the injection rate and the rate of heat release. In this chapter, without paying any detailed attention to the above-stated processes, an approach to the latter direction is planned by introducing a model of the combustion system, the essential of which lies in the concept that the ignition of every fuel element injected at different time grows shorter according to the changing state parameters of the cylinder charge. The analysis led to the conclusion that the qualitative nature of rapid combustion could be described somewhat successfully by introducing such a model.

### 6.2 Ignition Delay and Its Time Variation

1) Increase in heat-release rate ensured from the time-variation of the ignition delay

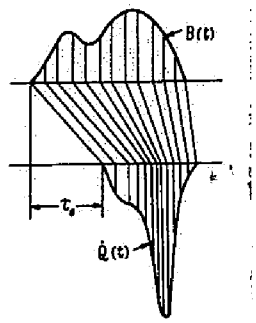


Fig.6.1 Relation between injection rate B(t) and heat release rate $\dot{Q}(t)$

Assume that fuel droplets distributed in a spray form over the space of the combustion chamber behave thermally independently of one another. If the combustion chamber were an infinite space, then the rate of heat release would be equal to the injection rate since the ignition delay of all droplets would be the same. This is very distant from the actual condition. When the volume of the combustion chamber is finite as is in the actual case, the ignition delay of successive fuel elements becomes shorter as the pressure and the temperature rise in the cylinder after the combustion starts, even if each fuel element is thermally insulated from another. The degree of the shortening of the delay will be to such extent that, in the stages of controlled combustion, fuel can burn immediately after it comes into the combustion chamber; namely, it burns almost without delay. In short, the fuel introduced ealier has a longer delay whereas the one introduced later has a shorter one. It is anticipated that fuel burns crowdedly sometime in the middle of the combustion stages when the ignition delay changes rapidly with time, leading to a higher rate of heat release than the injection rate. In Fig. 6.1 is shown schematically the relationship between the course of the injection rate $B(t)$ and the development of heat-release rate $\dot{Q}(t)$ in which t denotes time. Each of the strips drawn in the figure indicates the same fuel element. Since the less the duration assigned to burning of a fuel element the higher becomes the rate of heat release, the density of the strips is proportional to the ratio of $\dot{Q}(t)$ to the corresponding rate of injection. In particular, when these strips coalesce in a point, the combustion would occur sometime all at once, thus resulting in an infinitely high rate of heat release. If such a process constitutes the origin of rapid combustion, we shall be able to obtain some fundamental knowledges on the diesel knock. In order to analyze the combustion process from this point of view, we ought to describe the influence of time-variation of the ignition delay on the heat-release rate and thereafter how the variation of the delay develops under the changing pressure and temperature.

For the sake of convenience we now introduce time variable z for scaling the injection time, by which we are able to distinguish it from the time variable t for measuring the heat release-rate $\dot{Q}(t)$. Let us take the commencement of the injection to be the origin of both time variables and assume the ignition delay of the fuel element introduced

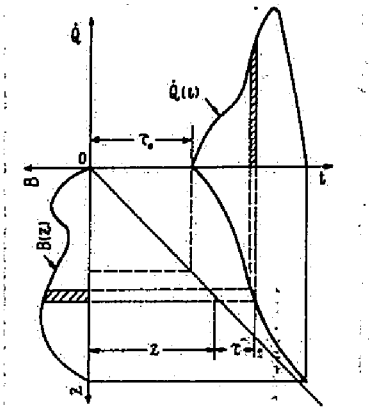


Fig.6.2 Comprehensive diagram of changing ignition delay

in the beginning to be a given magnitude $\tau_0$. If we write the ignition delay of fuel element introduced at an arbitrary time as $\tau$, the following relation has to hold for the fuel element under consideration.

$$z = t - \tau \tag{6.1}$$

Fig. 6.2 shows a comprehensive diagram of the changing ignition delay mechanism. As can be recognized from the figure, a fuel element introduced at z during an infinitesimal period $\Delta z$, which amounts to $B(z)\Delta z$, releases heat at a rate $\dot{Q}(t)$ during an infinitesimal period $\Delta t$. It will be reasonably assumed that the heat introduced $B(z)\Delta z$ is equal to the heat released $\dot{Q}(t)\Delta t$. This may be described as follows:

$$\dot{Q}(t) = \frac{B(z)}{\frac{dt}{dz}} = \frac{B(z)}{1 + \frac{d\tau(z)}{dz}} \tag{6.2}$$

The initial ignition delay $\tau_0$ depends on the pressure and temperature of the quiescent gas before the combustion; for example, it obeys the Wolfer's formula in the following[34].

$$\tau_0 = C p_0^{-n} e^{a/T_0} \tag{6.3}$$

where $p_0$ denotes the initial pressure, $T_0$ the initial temperature, and c, n and $a$ constants. Wolfer gave c=0.44, n=1.19 and $a$ =4650°K when $p_0$ was expressed in ata. After the combustion starts, the ignition delay grows shorter with the rises in both pressure and temperature in the combustion chamber. The ignition delay of successive fuel element cannot be determined by any empirical formula since the pressure and temperature change from time to time during the delay period of a considering fuel element.

2) Ignition delay under changing pressure and temperature

Although many research works have been conducted experimentally to determine the ignition delay in the bomb or in the engine, these ignition delay data have been gained under the condition in which the process is assumed to be in a fixed state. Therefore, it is necessary for the present purpose to estimate the ignition delay of a changing environment during the induction period. There is almost no established rule of predicting it from the delay data gained at a fixed state, ex-

cept one presented by Livengood and Wu[35]. Their method will be summarized briefly in the following: Let us put p(t) and T(t) as the changing pressure and temperature respectively. The ignition delay at a fixed environment is assumed to be given as a function of instantaneous values of p and T. We denote this delay as $\sigma=\sigma(p,T)$. The reaction velocity during the delay period is not constant when p and T are changing. We assume that there is always a fixed relationship between the concentration of active center of reaction x and the relative time $t/\sigma$. Thus we can write the equation of reaction as follows:

$$\frac{d}{dt}\left(\frac{x}{x_c}\right) = \phi\left(\frac{t}{\sigma}\right) \tag{6.4}$$

where $\phi$ denotes the function of reaction rate and $x_c$ the critical concentration (constant). When $x/x_c=1$, fuel ignites. Integrating this equation, we get

$$\frac{x}{x_c} = \int_0^{\tau} \phi\left(\frac{t}{\sigma}\right) dt = 1 \tag{6.5}$$

where $\tau$ is the unknown ignition delay. If we assume that for a fixed state process the reaction rate does not change with time (zero-th order reaction), the following relation has to hold:

$$\phi(t/\sigma) = 1/\sigma \tag{6.6}$$

Therefore Eq. (6.5) can be written as the following form.

$$\int_0^{\tau} \frac{dt}{\sigma} = 1 \tag{6.7}$$

This equation may be solved with the aid of ignition delay data and a knowledge of the state-time history of the process. By using this equation, Livengood and Wu tried to predict the condition of autoignition in a gasoline engine from the delay data gained by Rapid Compression Machine and the state history of gas measured by the velocity of sound technique. The predicted conditions of autoignition showed a fairly good agreement with the experimental ones. Eq. (6.7) seems applicable as well for predicting the ignition delay in a diesel engine which is now considered. As the ignition delay data, we use Wolfer's formula, that is,

$$\sigma(p, T) = cp^{-n}e^{a/T} \tag{6.8}$$

Since $\sigma$ is a function depending on state parameters and does not indicate the ignition delay itself under the changing environment, $\sigma$ may be designated as the ignition delay function. Now our problem is reduced to solving $\tau$ out of Eq. (6.7) by the aid of Eq. (6.8).

3) Ignition delay of fuel injected at a given time

For the convenience sake, we adopt the following notation:

$$f(h) = \int_0^h \frac{dt}{\sigma(t)} \tag{6.9}$$

where h denotes a variable. If p and T are uniform over the total gas inside the combustion chamber, then the function f(h) of the considered fuel element depends only on the time progress of p and T. Although a fuel element injected at different time has a different value of f(h), f(h) is the integral of a common function of $1/\sigma$. From the fact that the difference in f(h) is merely the range of the integration, we can determine the ignition delay $\tau$ of the fuel injected at a given time z.

In the case of $z < \tau_0$: Let t'=t-z be the time elapsed after injection of the considering fuel element. When t' is between zero and $\tau_0$-z, no fuel has ignited yet in the combustion chamber, and when t'= $\tau_0$-z, fuel injected starts to burn. Separating the left side of Eq. (6.7) into two parts at t'=$\tau_0$-z, we obtain

$$1 = \int_0^{\tau_0 - z} \frac{dt}{\sigma(t)} + \int_{\tau_0 - z}^{t'} \frac{dt}{\sigma(t)} \tag{6.10}$$

$\sigma$(t) in the first integral being equal to $\tau_0$ and the second integral being able to alter the range of integration, Eq. (16.10) is reduced to

$$1 = \frac{\tau_0 - z}{\tau_0} + f(t' - \tau_0 + z) \tag{6.11}$$

As the ignition delay $\tau(z)$ is such t' as to fulfil this equation, we can reach the final expression

$$\tau(z) = f^{-1}(z/\tau_0) + \tau_0 - z \quad [z < \tau_0] \tag{6.12}$$

where $f^{-1}$ denotes the inverse function of f(h).

In the case of $z \geq \tau_0$: The considered injection time is later than the earliest inflammation by $z-\tau_0$. If we trace back to the start of

burning in measuring time in Eq. (6.7), we have

$$1 = \int_{\tau_0 - z}^{t'} \frac{dt}{\sigma(t)} - \int_{\tau_0 - z}^{0} \frac{dt}{\sigma(t)} \tag{6.13}$$

or

$$1 = f(t' - \tau_0 + z) - f(z - \tau_0) \tag{6.14}$$

Putting $\tau(z)$ on t' in this equation and solving it, ignition delay finally becomes

$$\tau(z) = f^{-1}\{f(z - \tau_0) + 1\} + \tau_0 - z \quad [z \geq \tau_0] \tag{6.15}$$

4) Relationships between z(t), f(h) and $\sigma$(h)

As the time variable z is related with the time variable t by Eq. (6.1), we get the following relationship for $z < \tau_0$.

$$t = f^{-1}(z/\tau_0) + \tau_0 \tag{6.16}$$

or

$$z = \tau_0 f(t - \tau_0) \tag{6.17}$$

The latter expression implies that the z versus t curve is quite similar to $\tau_0 f(h)$ for $z < \tau_0$. The gradient of the z versus t curve is, from Eqs. (6.9) and (6.16),

$$\frac{dt}{dz} = \frac{\sigma(t)}{\tau_0} \tag{6.18}$$

In the case of $z \geq \tau_0$, we get a similar relationship from Eq. (6.15), that is,

$$t = f^{-1}\{f(z - \tau_0) + 1\} + \tau_0 \tag{6.19}$$

Transforming Eq. (6.19) by using the next function

$$F(h) \equiv \tau_0 (h - \tau_0) \tag{6.20}$$

then we get

$$F(t) = F(z) + \tau_0 \tag{6.21}$$

Through a second transformation

$$G_T(h) = F(h) + \tau_0 \tag{6.22}$$

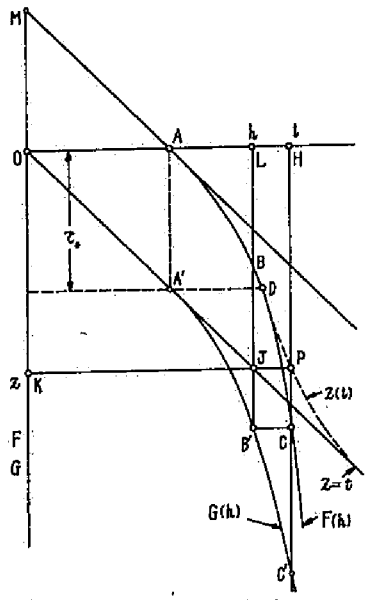


Fig.6.3 Geometrical relationship between z(t), f(h) and G(h)

we obtain a simple expression as follows:

$$F(t) = G(z) \tag{6.23}$$

We can now find out the following geometrical relations when the coordinate (F,h) is superimposed on the coordinate (z,t), as shown in Fig. 6.3. Drawing a curve ABC as F(h), it is clear from Eqs. (6.17) and (6.20) that for $z<\tau_0$ the z versus t curve coincides with F(h) while, for $z \geq \tau_0$, i.e. in the region below point D, the curve z(t) departs from F(h). Since G(h) is a parallel displacement of F(h) by $\tau_0$, we may draw G(h) as the curve A'B'C'. A fuel element that burns at time t, as represented by line OH, has been injected at time z which is represented as line OK=OL. Therefore, G(z) can be represented by line B'L. At the same time, G(z) is equal to F(t) from Eq. (6.23), namely, equal to CH. In other words, through the four apices of a rectangle JB'CP pass the following four curves; z=t, G(h), F(h) and z(t) respectively. Thus z(t) becomes uniquely determinable.

Next, we derive the differential quotient of z(t) for $z \geq \tau_0$. Differentiating Eq. (23), we have the following relation.

$$\left(\frac{dt}{dz}\right)_P = \frac{(dG/dh)_{h=z}}{(dF/dh)_{h=t}} = \frac{(dG/dh)_{B'}}{(dF/dh)_C} \tag{6.24}$$

This relation indicates that the gradient of the curve z(t) at point P is given by the ratio of the slope at B' to that at C. Using Eqs. (6.20), (6.22) and (6.9), we obtain

$$\frac{dt}{dz} = \frac{d\{f(z)\}}{d\{f(t)\}} = \frac{\sigma(t)}{\sigma(z)} \tag{6.25}$$

This final expression can be easily extended to the case of $z<\tau_0$: Since the state parameters are invariable during the initial delay period, $\sigma(z)$ is clearly equal to $\tau_0$ for $t<\tau_0$, therefore Eq. (6.25) is reduced to Eq. (6.18). This matter is quite equivalent to drawing a straight line OA' as the continuation of G(h) in the range $h<\tau_0$. Finally, Eq. (6.25) will serve to calculate the relation between the injection rate B(z) and heat-release rate $\dot{Q}(t)$. Putting Eq. (6.25) into Eq. (6.2), we have

$$\dot{Q}(t) = B(z)\,\frac{\sigma(z)}{\sigma(t)} \tag{6.26}$$

It is noted that the ignition delay is inplicit in Eqs. (6.25) and (6.26).

## 6.3 Predicted Heat-Release Rate

### 1) Combustion knock without considering fuel vaporization

Governing equations Changing ignition delay and its effect on the heat-release rate were described in the last section. In order to estimate the time developments of heat-release, pressure and temperature we make the following assumptions in the calculation:

(1) Each of fuel elements does not release any heat during the delay period and as soon as the fuel element ignites, it is converted into final products releasing the total energy of fuel.

(2) Fuel droplets are fine and uniformly distributed over the combustion chamber. The pressure and temperature are macroscopically unfirom, but there is no microscopic interaction between fuel particles.

(3) Both the total weight of gas and the volume of the combustion chamber do not change throughout the combustion and the gas obeys the ideal air law.

(4) Vaporization time of a fuel droplet is negligibly short.

Denoting gas weight and volume of the chamber as G and V respectively, we have the following relations:

$$\dot{Q} = c_v G \dot{T} \qquad \text{(First law of thermodynamics)} \qquad (6.27)$$

$$pV = GRT \qquad \text{(Ideal gas law)} \qquad (6.28)$$

where $c_v$ denotes specific heat at constant volume (=0.171 kcal/kg$^\circ$K), and R gas constant (=29.3 m/$^\circ$K). Unknown variables are $\dot{Q}$, p, T, $\sigma$ and z. For these five unknowns, Eqs. (6.8), (6.25), (6.26), (6.27) and (6.28) are given as the simultaneous differential equations. Among variables, B, $\dot{Q}$ and G are intensive quantities so that we can consider them as the quantities per unit weight of gas. Therefore G is unity in the present case. Because of nonlinearity of the governing equations, all solutions were obtained by numerical method.

Influence of ignition delay At first, the calculations were made for the following conditions; initial pressure $p_o$=40 kg/cm$^2$ and injection rate B=0.2 kcal/g of air/msec (of course B=0 when $z<0$). In order to evaluate the effect of the initial ignition delay, the

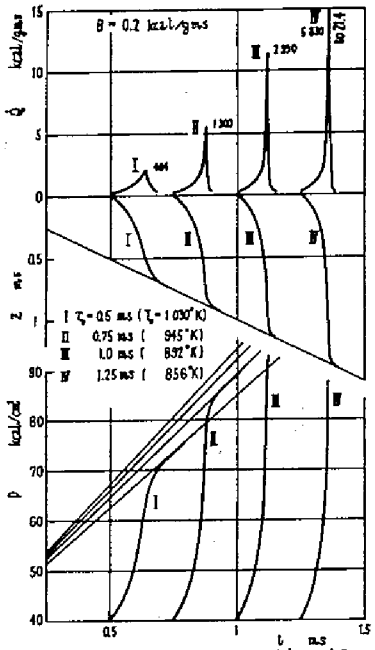


Fig.6.4 Influence of initial ignition delay under a step-functional injection rate (Numerical values written in the each peak position of $\dot{Q}$ indicate the maximum rate of pressure rise in $kg/cm^2/ms$.)

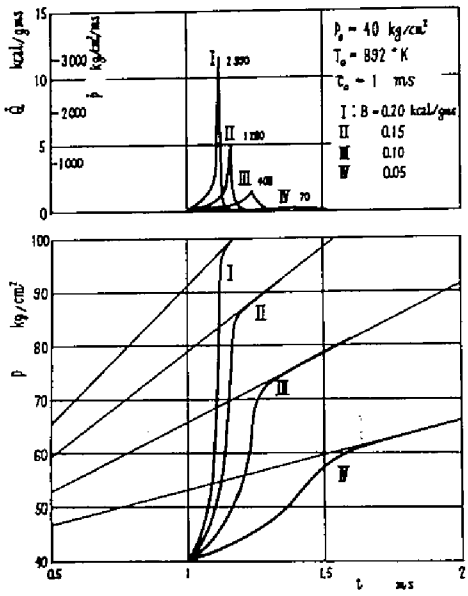


Fig.6.5 Influence of injection rate

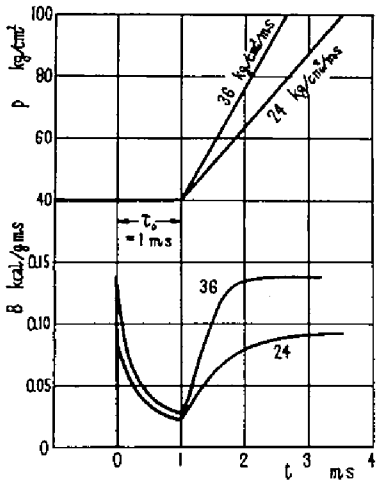


Fig.6.6 Effect of pilot injection

following four cases were taken; $\tau_0$=0.5, 0.75, 1 and 1.25 msec, in which the initial gas temperature $T_0$ was properly selected so as to fit the stated conditions. The solutions are inclusively drawn in Fig. 6.4.

As seen from the figure, z(t) starts with a gradient of unity (dz/dt=1) and accelerates toward the maximum gradient at $z=\tau_0$ where $\dot{Q}$ reaches its maximum. Thereafter the curve z(t) quickly approaches the asymptotic line z=t and $\dot{Q}(t)$ does B(t). Since the pressure rise is proportional to $\int \dot{Q}(t)dt$, the pressure-time curve is S-shaped at first and asymptotically approaches a certain line. It can be seen that both the maximum rate of heat-release and the maximum rate of pressure rise increase rapidly with the initial ignition delay. This is in accordance with the trend in practical engines.

Influence of injection rate Under the initial conditions of $p_0$= 40 kg/cm$^2$ and $\tau_0$=1 msec ($T_0$=892°K), the influence of injection rate B on the heat-release rate was investigated. The results of numerical calculation are presented in Fig. 6.5. As can be seen from this, the injection rate has a large influence on the maximum rate of heat release and its dependence can be roughly expressed by the following form in the range where the calculations were made:

$$\dot{Q}_{max} \backsim B^{2.7} \tag{6.29}$$

This result seems to be supported by the current understanding that reduction in the injection rate is effective for reducing the combustion knock. In the later stages of combustion when the maximum heat-release rate is over, the ignition delay of the fuel element tends to zero so that a larger injection rate is allowable in such stages. Consequently, such an injection rate diagram may be ideal that the rate is low during the delay period but is high after the delay period is finished.

Effect of pilot injection Next, the injection rate versus time relation was estimated for a given pressure development. From the viewpoint of knock suppression, the maximum rate of pressure rise is recommended to be less than 4 kg/cm$^2$/deg in crank angle in the practical engine. Therefore we can assume the ideal pressure development to be a ramp function at a fixed rate of $\dot{p}$=36 kg/cm$^2$/msec at an engine speed of 1500 rpm. In Fig. 6.6 are shown the calculated injection rate time relations, together with the given pressure developments of $\dot{p}$=36 kg/cm$^2$ /msec and 24 kg/cm$^2$/msec. It can be seen from the figure that a quite

low rate of pressure rise can be realized by adopting the pilot injection characteristics; namely, considerably high injection rate at first which is followed by a gradual decrease until the ignition and a rapid growth to a constant injection rate. If the injection rate is not high enough in the earliest stage, then the pressure rise will be less sharp at its very beginning since the initial high injection rate concerns with the curvature of the pressure rise.

2) Combustion knock with fuel vaporization considered

Relation between injection rate and velocity of vaporization

Because all of the physical properties of spray, such as distribution and vaporization of fuel, were neglected in the foregoing treatment, the numerical values of heat-release rate obtained from the foregoing calculations gave impractically large ones. For example, let us consider an engine operating at a speed n=1500 rpm, excess air ratio $\lambda$= 1.5 and duration of injection $\phi=20^{\circ}$. If the stoichiometric air $L_0$ and real calorific value $H_u$ are 14.5 kg/kg and $10^4$ kcal/kg respectively, then the average injection rate B will be

$$B=\frac{6nH_u}{(1+\lambda L_o)\phi}=0.198 \text{ kcal/g of air/msec} \qquad (6.30)$$

The injection rate 0.2 kcal/g of air/msec, the value of which was presented in the previous figures, was a proper estimate. Further, if the initial ignition delay is 1 msec, that is, $9^{\circ}$ in crank angle, which seems to be an entirely reasonable value for a practical engine, then the theoretical maximum rate of pressure rise, from Fig. 6.4, amounts to 2990 kg/cm$^2$/msec or 332 kg/cm$^2$/deg. This is extraordinarily high for the value of usual operating condition, considered from our experience. One of the causes of its overestimate seems to be the fact that the vaporizing velocity of the fuel injected was assumed to be infinite in the calculations.

Hitherto, several investigations were carried out about the vaporization process of finely atomized fuel droplets. Among them, the simplest theory will be sufficient for evaluating the effect of velocity of fuel vaporization on combustion knock, because no quantitative argument is necessary for our present purpose. Hence, assuming an iso-thermal quasi-stationary prooess of vaporization of an aggregate of the same-sized fuel particles and neglecting the heat-up time, we

determine the relation between injection rate and velocity of vaporization. Thus the droplet diameter d at time z is

$$d^2 = d_o^2 - Kz \tag{6.31}$$

where $d_o$ is the initial diameter and K the coefficient of velocity of vaporization. K is constant in the iso-thermal quasi-stationary process. Change in weight of a particle w per unit time is

$$-\frac{dw}{dz} = -\frac{d}{dz}\left\{\frac{\pi}{6}\gamma_b d^3\right\} = \frac{\pi}{4}\gamma_b K\sqrt{d_o^2 - Kz} \tag{6.32}$$

where $\gamma_b$ denotes the specific weight of the fuel in liquid phase. As the initial weight of a particle is equal to $(\pi/6)\gamma_b d_o^3$, vaporization velocity $\psi(z)$, when fuel of unit weight is instantaneously introduced, is

$$\psi(z) = \begin{cases} \frac{3}{2z_o}\sqrt{1-\frac{z}{z_o}} & [0 \leqq z/z_o < 1] \\ 0 & [1 \leqq z/z_o] \end{cases} \tag{6.33}$$

where $z_o$ is vaporization time: $z_o = d_o^2/K$ (6.34)

When the injection rate B(z) is given, the rate of vaporization C(z) can be obtained by superposition using $\psi(z)$ as the weighting function, namely,

$$C(z) = \int_0^z B(\theta)\psi(z-\theta)d\theta \tag{6.35}$$

If B(z) is a step function, C(z) is

$$C(z) = \begin{cases} B\left\{1-\left(1-\frac{z}{z_o}\right)^{3/2}\right\} & [0 \leqq z/z_o < 1] \\ B & [1 \leqq z/z_o] \end{cases} \tag{6.36}$$

The coefficient of vaporization is estimated on the basis of Sitkei's description[36]. Owing to quasis-tationary process, the heat transferred from the surrounding air to the surface of droplet, q, is equal to the heat carried away by mass transfer. Thus we have

$$q/\pi d^2 = \alpha(T - T_L) = \beta(p_L - p_K)l \tag{6.37}$$

where $\alpha$ and $\beta$ denote transfer coefficients of heat and matter respectively, T and $T_L$ temperatures in the surrounding and at the surface of the droplet, $p_K$ and $p_L$ partial pressures of fuel vapor in the surrounding and at the surface respectively, and $l$ latent heat plus superheat.

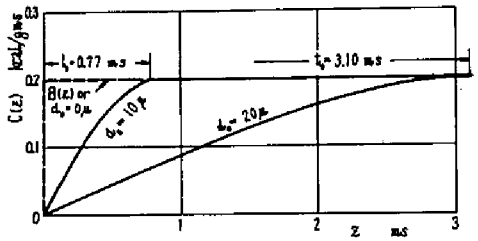


Fig.6.7 Vaporization velocity of a step-functional injection rate

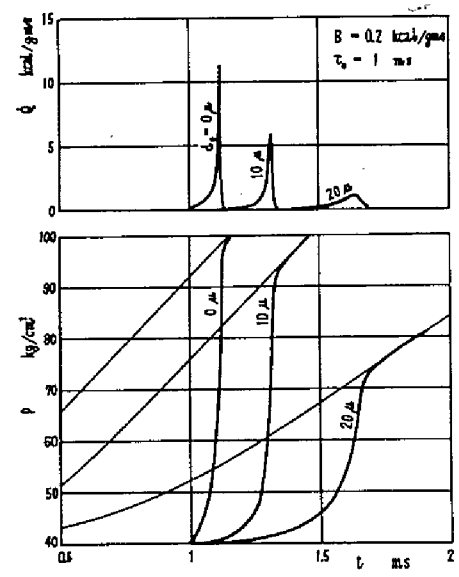


Fig.6.8 Influence of particle size

Assuming that the droplet diameter is so small that the fuel vapor is transferred outward by molecular diffusion, namely, the Nusselt number is two, we get the following relationship.

$$\alpha d/\lambda = \beta d/D_p = 2 \tag{6.38}$$

where $\lambda$ denotes the thermal conductivity and $D_p$ the diffusion coefficient. If we neglect any interaction between droplets, $p_K$ is naught in Eq. (6.37), thus leading to

$$\lambda(T - T_L) = D_p l p_L \tag{6.39}$$

$p_L$ and $D_p$ are given by the following formulae:

$$D_p = D_{po} \frac{T}{T_n} \frac{p_n}{p} \tag{6.40}$$

$$p_L = c_L e^{-b/T_L} \tag{6.41}$$

where p denotes the total pressure, $p_n$ and $T_n$ reference pressure and temperature (1 kg/cm$^2$ and 273°K respectively), and $c_L$, b and $D_{po}$ constants. Solving simultaneously Eqs. (6.39) through (6.41), we obtain $P_L$, $T_L$ and $D_p$. The velocity of vaporization of a droplet is

$$-\frac{dw}{dz} = \pi d^2 \beta p_L \tag{6.42}$$

so that K and $z_0$ become, by comparing Eq. (6.42) with Eq. (6.32),

$$K = \frac{8 D_p p_L}{\gamma_b} \tag{6.43}$$

and

$$z_0 = \frac{d_0^2 \gamma_b}{8 D_p p_L} \tag{6.44}$$

Results of calculation Given $p_0$=40kg/cm$^2$ and $T_0$=892°K (see Fig. 6.5), K and $z_0$ were calculated by using Sitkei's data[4] ($D_{po}$=0.121x 10$^{-4}$ m/hr, $c_L$=6.0x10$^7$ kg/m$^2$, b=4.15x10$^3$ °K). We get $T_L$=602°K and K= 1.30x10$^2$ $\mu^2$/msec at $l$=280 kcal/kg, so that for two kinds of initial droplet diameters $d_0$=10$\mu$ and 20$\mu$ the vaporization time $z_0$ is 0.77 msec and 3.10 msec respectively. Fig.6.7 shows the vaporization rate versus time relation C(z) of these droplets at B=0.2 kcal/g of air/ msec. Using the vaporization rates thus obtained, the heat-release rate $\dot{Q}(t)$ as well as the pressure development was computed. The results are summarized in Fig. 6.8, in which vaporization rates are assumed not to be influenced by combustion throughout the process. It

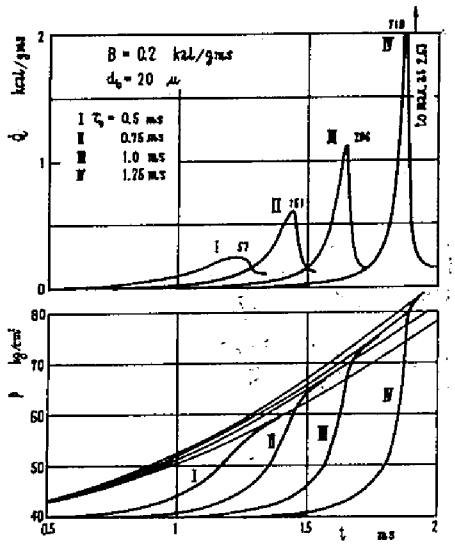


Fig.6.9 Influence of ignition delay under consideration of fuel vaporization (notice the scale of $\dot{Q}$)

can be seen that the heat-release rate and the rate of pressure rise are remarkably lower than those when the influence of the vaporization is neglected ($d_0=0\mu$ in the figure). The maximum rate of heat release at $20\mu$ of initial diameter is only about one tenth that at $0\mu$. By the way, another finding is that the larger the initial diameter the later comes the moment of maximum rate of heat release.

Assuming the droplet diameter to be $20\mu$ and neglecting the temperature dependence on the vaporization velocity, the heat-release rate was calculated for various ignition delays under the same condition of Fig.6. 4. Fig. 6.9 shows the results. As seen from the figure, $\dot{Q}_{max}$ rapidly decreases as the initial ignition delay $\tau_0$ is reduced. The maximum rates of pressure rise become nearer to the practical value as compared with the case of Fig. 6.4; if we compute them in terms of crank angle basis at an engine-speed of 1500 rpm, they are 80, 33, 17 and 6.3 kg/$cm^2$/deg for $\tau_0$=1.25, 1.0, 0.75 and 0.5 msec respectively.

In the above-stated theory, the vaporizing velocity of fuel was calculated on the assumption of molecular diffusion process. This assumption is correct only when the droplets are very fine or quiescent. However, there are large particles and a large relative-velocity between air and a droplet owing to injection, turbulent diffusion and air swirl. It can be considered that the calculation based on the molecular diffusion gives the lower limit of the theoretical rate of heat release whereas the calculation of the infinite vaporizing velocity describes its higher limit.

3) Consideration on the theory

Although the qualitative nature of the relation between injection rate $B(z)$ and heat-release rate $\dot{Q}(t)$ was fairly well established, there are several kinds of assumptions put in this theory which hinder its application to the practical case. In order to improve the theory we must consider the following matters in the first place.

(1) Ignition delay: Strictly speaking, Wolfer's formula here adopted is valid for a relatively long ignition delay. In the present calculation an extrapolation was made to too short delay. Therefore a more proper selection of the expression for the ignition delay will be required when quantitative results are expected. According to the present knowledge, the ignition delay consists of two parts, namely, the physical

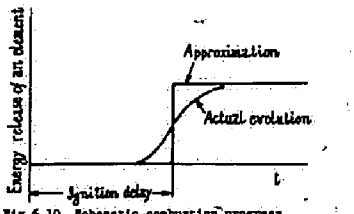


Fig.6.10. Schematic combustion progress of an element of fuel

delay and the chemical delay. Since the latter is very short at a high temperature range, the physical delay occupies an important part of the total induction period. In such a condition, the approximation of the zero-th order reaction is not correct and a more adequate treatment becomes necessary. However, it does not seem difficult to make up for the defect of our theory by applying the many detailed theories and their results concerning the physical delay[37].

(2) Heat evolution of an element of fuel: In the theory it was assumed that each of the fuel elements did not produce any appreciable energy release during the delay period whereupon it was suddenly converted into final products of reaction. Fig. 6.10 shows schematically the discontinuous evolution of heat of an element as drawn in the solid line. This discontinuous process is the first approximation which was already adopted by Crocco and Cheng in the analysis of combustion instability of a rocket motor[38]. The actually encountered heat evolution, however, will follow an imperfect step-function like the broken line drawn in the same figure, which originates from several effects; namely, gradual oxidation during the delay period, decrease in the concentration of reactants, their poor mixing and so forth. The precise descriptions of them would require detailed knowledges of all the intermediate processes. This is impossible at present. In order to estimate the effect of deviation from the pure discontinuity, let us consider the reaction time defined as the half-value width of the rate diagram of heat-release evolution. Since the reaction time may be considered to be the same order of the rapidness of autoignition of homogeneous mixture in a gasoline engine, we can expect that the magnitude of the reaction time will be small enough to neglect in the calculation of pressure-and temperature-developments when the velocities of injection and vaporization are relatively low.

(3) Influence of flame propagation: The considered combustion system has a positive feed-back loop through the changing delay time sensitive to the previous courses of temperature and pressure. Owing to this, a rapid burning can occur even if microscopic structure of dispersed fuel particles is essentially adiabatic without occurrence of any flame propagation. On the other hand, many experimental observations made by high-speed photography of the diesel combustion chamber show that an ignitable mixture burns very rapidly once ignition occurs from one or several nuclei, the flame spreading over the spray jet and covering the entire combustion space within a very short

duration, just like the flame propagation. Austen and Lyn, who inquired into the combustion process of a direct-injection engine, stated that the process occurring in early stages of combustion lies in the border region of simultaneous autoignition and flame propagation[33]. Since the flame propagation can get ahead of successive autoignition when the latter process is slow, it seems probable that simultaneously with successive autoignition the flame propagates both apparently and substantially. But, the speed of propagation itself cannot be so fast as considered from the normal flame speed in a gasoline engine. Alcock and Scott saw no correlation between the diesel knock and the flame speed and found that the spreading velocity of apparent flame front was far less than the velocity of detonation or shock wave[29]. These matters probably support the fact that the flame propagation alone cannot produce an explosive nature of combustion in a diesel engine.

## 6.4 Conclusion

From the above mentioned analysis, we reach the following conclusion: The nature of the combustion knock in a diesel engine can be well described by introducing the concept that the ignition delay of the injected fuel element varies from time to time according to the changes in temperature and pressure of the charge. In this process, the rate of heat release is multiplied by the shortening velocity of the ignition delay thus resulting in an explosive nature of combustion. By using this theory, we can evaluate the effects of various factors on the rate of pressure rise in the cylinder.

## CONCLUSION

The combustion noise of a diesel engine has formed a vast study of research work covering the problems in structure of the engine, fuel injection system, combustion system and physical-chemical mechanism of combustion. It is true to say that there are still several gaps in our fundamental knowledge of the combustion noise some of which were thrown into relief by the recent investigations.

In this thesis, some essential nature of the combustion noise of a diesel engine and characteristics of the combustion knock were better understood than before, from several experimental works made by accurate measurement of pressure change in the combustion chamber as well as from several theoretical attempts by introducing various kinds of combustion models. The results would be expected to contribute to some more progress of the high speed diesel engines.

The first acknowledgement is made to Dr. Fujio Nagao, Professor of Kyoto University, who has given a kind and invaluable guidance to the author throughout this work and has been a source of encouragement. Thanks are also due to the students of Kyoto University for their assistances in the experimental work and in the numerical calculations. This work was partially supported by Research Grant for Scientific Experiments by Ministry of Education from 1960 to 1961.

Cited References


(1) H. R. Ricardo: The High-Speed Internal Combustion Engine, (1953), Blakie & Son.

(2) A. J. Davies: Proc. Instn. Mech. Engrs. (A. D.), (1951-52), p.214.

(3) J. S. Meurer: SAE Trans., Vol.64 (1956), p.250.

(4) M. Alperstein, W. B. Swim, and P. H. Schweitzer, SAE Trans., Vol.66 (1958), 574.

(5) G. Grosshans et al: 5th World Petroleum Congress, (1959).

(6) R. Kloss: MTZ, Jg.19, Ht.9 (1958), S.302.

(7) F. Hertl: Energie, Jg.13, Ht.8 (1961), S.337.

(8) J. S. Meurer: SAE Trans., Vol.70 (1962), p.712.

(9) T. Priede: Proc. Instn. Mech. Engrs. (A.D), (1960-61), p.63.

(10) F. Nagao, H. Kakimoto and M. Hirukawa: Trans. Japan Soc. Mech. Engrs., Vol.25, No.160 (1959), p.1325.

(11) T. Ito: Onkyo-Kogaku-Genron (Fudamentals of Acoustic Engineering), Vol.2, (1957), Corona-sha.

(12) M. Maekawa: Trans. Japan Soc. Mech. Engrs., Vol.2, No.6 (1936), p.106.

(13) J. A. Robinson, M. D. Behren, R. G. Mosher, and J. M. Chandler: SAE Trans., Vol.66 (1958), p.549.

(14) H. Steinbrenner, E.-L. Alpert, und H. J. Florus: MTZ, Jg.23, Ht. 2 (1962), S.39.

(15) F. Nagao, Y. Shimamoto, and Y. Ueno: Trans. Japan Soc. Mech. Engrs., Vol.28, No.189 (1962), p.620.

(16) R. C. Binder and A. S. Hall: Jour. Appl. Mech., Vol.14, No.3 (1947), p.183.

(17) F. Nagao, H. Kakimoto, and T. Hiraoka: Trans. Japan Soc. Mech. Engrs., Vol.24, No.144 (1958), p.599.

(18) A. K. Oppenheim: Jour. Appl. Mech., Vol.20, No.1 (1953), p.175.

(19) P. H. Schweitzer: Trans. ASME, Vol.74, No.4 (1952), p.517.

(20) F. Nagao, Y. Shimamoto, et al: Preprint of the 37th annual Meeting of Kansai Branch, Japan Soc. Mech. Engrs., Part 2 (1962-3), p.17.

(21) H. R. Dinkelacker, Experimentelle Verfolgung zweidimensionaler instationärer Gasströmung auf Grund der Gas-Flachwasser-Analogie, (1959), Leemann.

(22) F. Nagao und H. Kakimoto: MTZ, Jg.20, Nr.6 (1959), S.183; Nr.8 (1959), S.303.

(23) A. Pischinger und F. Pischinger: MTZ, Jg.20, Nr.1 (1959), S.5.
(24) T. Ito: Onkyo-Kogaku-Genron, Vol.1 (1958), Corona-sha.
(25) G. Sitkei: Periodica Polytechnica, Vol.5, No.1 (1957), p.48.
(26) F. Nagao, T. Kobayakawa, et al: Trans. Japan Soc. Mech. Engrs., Vol.23, No.132 (1957), p.579.
(27) J. Alcock and R. Watts, CIMAC-A7 (1959), p.246.
(28) F. Nagao, H. Kakimoto, S. Ohta and M. Konishi: Trans. Japan Soc. Mech. Engrs., Vol.27, No.177 (1961), p.762.
(29) J. F. Alcock and W. M. Scott: Proc. Instn. Mech. Engrs. (A. D.), No.5 (1962-63), p.179.
(30) T. Kushiyama: Mitsubishi Heavy Industries Tech. Rev., Vol.3, No.3 (1966), p.226.
(31) C. Shacke u. H. Straubel: Kraftfahrzeugtechnik, Bd.6, Nr.9 (1956), S.324.
(32) W. Browne: SAE Trans., Vol.48 (1941), p.148.
(33) A.E. W. Austen and W. T. Lyn: Proc. Instn. Mech. Engrs., (A. D.), No.1 (1960-61), p.47.
(34) H. H. Wolfer: VDI Forsch.-h. 392 (1938).
(35) J. C. Livengood and P. C. Wu: 5th Symposium on Combustion, (1955), p.347, Reinhold.
(36) G. Sitkei: Kraftstoffaufbereitung und Verbrennung bei Dieselmotoren, (1964), Springer.
(37) M. M. ElWakil et al.: SAE Trans., Vol.64 (1956), p.712.
(38) L. Crocco and S. Cheng: Theory of Combustion Instability in Liquid Propellant Rocket Motors, (1958), Butterworths.